Thin-Walled Structures for Energy Absorption

Yang Li

St Anne’s College

A thesis submitted for the degree of Doctor of Philosophy in the Department of Engineering Science, University of Oxford.

Trinity Term, 2016

To my parents.

Abstract

This thesis considered three types of new and improved high-performance energy absorbing devices for either compression or bending applications. These improvements were achieved by only altering their initial geometries for desired failure modes. Three types of proposed energy absorbing structures are as follows.

First, origami initiators were added to tubes with concave cross-sections. This new type of geometries, named as *origami concave tubes*, successfully triggered a reliable progressive buckling failure, which is uncommon for tubes with concave cross-sections. Origami concave tubes achieved ultra-high energy absorption and relatively low peak force. A comprehensive numerical, experimental, and theoretical analysis was conducted on the square, traditional concave, and origami concave tubes, which showed origami concave tubes achieved 3.3 times of specific energy absorption of square tubes. Additional to the huge improvement, it was illustrated that origami concave tubes can approach the theoretical limit of energy absorption through progressive buckling failure.

Second, thin-walled tubes with corrugated cross-section instead of traditional circular tubes were proposed for inversion. Comparing to circular tubes, the introduction of corrugation not only increased specific buckling force and reduced imperfection-sensitivity of tubes, but also decreased load needed for inversion process. In consequence, thin corrugated tubes could be inverted significantly more reliably, and even allowed practical frictional contact and geometric imperfection, which was not achieved or claimed before for tube inversion. A comprehensive numerical, experimental, and theoretical analysis was carried out on thin circular and corrugated tubes inversion, and validated the effectiveness of the new design. Thin corrugated tube inversion also reaches the theoretical limit of energy absorption.

Third, a series of novel bending devices of beams, panels, arches, and shells using origami technique were developed. These bending devices can provide more constant bending resistance and overall higher energy absorption than conventional open-section beams. Numerical simulations and experiments were used to validate these designs, which showed that properly designed origami bending devices can achieve 23.0%-40.0% increase of energy absorption and 12.7%-20.7% lower load uniformity than those of a conventional beam.

Keywords: energy absorbing structures, origami.

Acknowledgements

This thesis would not be possible without the ongoing support from my family, friends, and colleagues.

Firstly, I would like to thank my supervisor Professor Zhong You, who introduced me to these interesting topics and unique ways of thinking. He also provided me with abundant freedom as well as sufficient research fund during my study, from which I enjoyed my research and built up my confidence and independence. I would also like to thank Dr. Joe Gattas, Prof. Yan Chen, and Dr. Jiayao Ma for their technical supports and suggestions. For the patient help and teach of materials and experiments, I would like to thank technicians in Engineering Department, especially Graham Haynes, Cleveland Williams, Maurice Keeble-Smith, Igor Dyson, Bob Scott, and Clive Baker.

I appreciate deeply the companion from my dear friends in Engineering Department and St Anne's College, who made my life rich and colourful. I would also like to thank my Christian brothers and sisters from church, who brought me joyful experience and fellowship.

Finally, I want to thank my exceedingly tolerant girlfriend Huaping Sun, and my parents Guohua Li and Xuejun Yang for their selfless care and support.

Contents

Figures

Tables

Notation

A	Ratio between the amplitude of corrugation and R_{in}
a, b, c, d, h_b	Geometric parameters
b	Radius of bending
c	Width of the tube
D	Tube diameter
D_{in}	Inner diameter of tube
E	Young's modulus
E_1, E_2, E_3	Three sources of energy dissipation
E_{total}	Total energy dissipation
F', F	Reaction force
h, h_1, h_2	Folding length
L	Length
L	Total length of tube
l_1, l_2	Length of straight and inclined parts of the tube
M	mass
m_0	Parameter obtained from experiment
m_1, m_2	Exponents
M_p	Plastic bending moment
m_p	Power exponent of stress-strain curve
N	Number of pairs of corrugation
n_s	Strain hardening exponent
N_y	Yielding force
P_m, P_{m1}, P_{m2}	Mean crush force
R	Radius of tube
r_1, r_2	Radius of each corrugation
Rc	Radius when corrugated tube fully loses its corrugation
r_{die}	Radius of die
R_{in}, R_{mid}, R_{out}	Inner, middle, and outer diameter of tube
t	wall thickness
w	width

α	Pattern angle
ε	Strain
ε_u	Ultimate strain of material
θ	The central angle corresponding to each corrugation
θ_1, θ_2	Corresponding central angle of r_1 and r_2
μ	Friction coefficient
μ'	Equivalent friction coefficient
v	Poisson's ratio
ρ	Density of material
σ	Stress
σ_0	Equivalent plastic flow stress
σ_{cl}	Critical buckling stress
σ_{inv}	Inverting stress
σ_u	Ultimate stress of material
σ_y	Yield stress of material
Υ	Knockdown factor

Chapter 1 Introduction

1.1 Energy Absorbing Structures

Accidents involving impact to a transport vehicle take the lives of more than a million people every year and incapacitate many millions more (WHO, 2015). Energy absorbing components are used as a common way to mitigate damage in such accidents. An energy absorption device or structure is a structural component integrated into the main structure of a vehicle, which is designed to consume kinematic energy in an impact. Primarily there are three mechanisms to achieve energy absorption: plastic deformation (Wierzbicki, 1983), shear and fracture failure (Thornton, 1979), and frictional dissipation (such as frictional buffer stops) of structures. Amongst the energy absorption structures, the thin-walled structures, which utilise the plastic deformation mechanism, are most frequently used. They are made from ductile metals such as steel and aluminium, are inexpensive to manufacture and can be easily integrated with other structures of a vehicle. Forms of these structures include tubes which absorb energy when axially crushed, as well as beams/arches and panels/shells that absorb energy when being bent. Some of the structures are shown in Figure 1.1.

When designing an energy absorption structure, engineers always aim to achieve a high and consistent energy absorption capability per unit mass amongst various other objectives. Enormous efforts have made to achieve this target. For instance, Figure 1.2(a) shows a pair of tubular structures known as the crashcans. They are typically mounted between the bumper beam and main structure of a car. When the car is subjected to a frontal impact, the crashcans, which are under axial compression, undergo large plastic deformation so as to absorb energy.

The crashcans shown are square sectional tubes with a dented texture. The textures are purposely made to provide a consistent energy absorbing performance. Figure 1.2(b) shows an improved version of the crashcan design known as the origami crashcan (Ma, 2011). It consists of a set of diamond-shaped corners. Their presence increases the overall energy absorption capacity by over 50% in comparison with the crashcan designs given in Figure 1.2(a). Figure 1.2(c) and (d) show two bumper beams and their cross-sections. These beams, installed at the front of a vehicle, are for absorbing energy through bending. They have open-sections, and the beam below performs better especially with thinner material due to its shorter width introduced by the longitudinal dent (Ma, 2011). These examples demonstrate that a good geometrical shape could lead to a substantial increase of energy absorption ability.

Thin-walled structures for energy absorption are also widely used in lifts, aircraft, ship and trains (Johnson and Walton, 1983a, Johnson and Walton, 1983b), crash barriers (Reid and Sicking, 1998, Jin and Keping, 2013, Wei et al., 2013, Faller et al., 2007), protection structures in mines (Podjadtke et al., 2008), safety surroundings of radioactive material shipping casks (Kanae et al., 1986), and collision damage barriers for road bridges (Lei et al., 2012), etc..

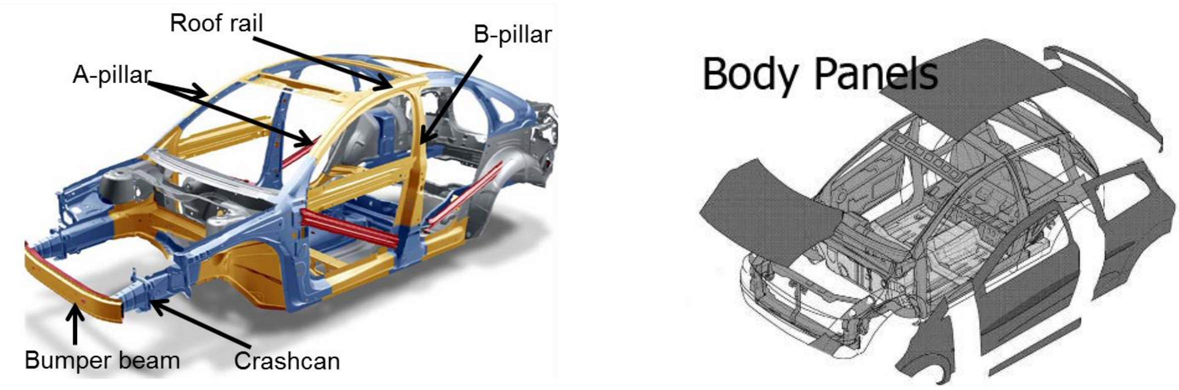

(a) Frames (b) Body panels

Figure 1.1. Energy absorbing components in vehicle.

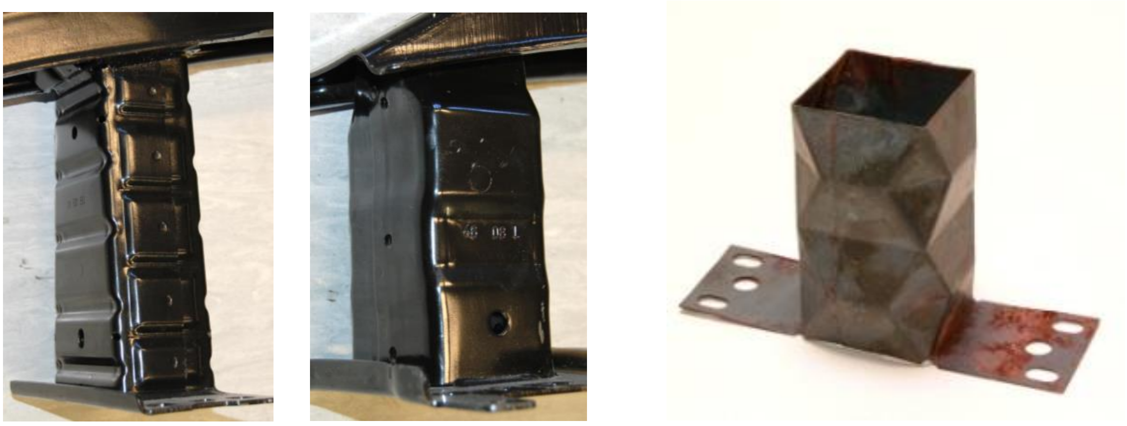

(a) Two crashcans (b) Origami crashcan

(c) One bumper beam and its cross-section

(d) Another bumper beam and its cross-section

Figure 1.2. Common design of energy absorbing components.

1.2 Aims, Scope and Layout

The object of this thesis is to propose new designs of high-performance energy absorbing thin-walled components. It is achieved by introducing new geometries aimed to induce a failure mechanism that is associated with higher overall energy absorption. The origami technique is employed to generate some of these new shapes that can be easily manufactured. The focus of this thesis is only on geometric modification of structures. The materials for these structures are identical to the conventional ductile metallic materials used for current thin-walled energy absorption structures, such as the stainless steel and annealed aluminium. The structures fail due to large plastic deformation.

The thesis structure is as follows. Chapter 2 is a literature review encompassing three areas of compression and bending structures for energy absorption as well as origami engineering. In the first area, particular focus is given to energy absorption using tube buckling. In the second area, energy absorption by inversion of a thin-walled tube is reviewed, whereas the structures subjected to bending is the emphasis in the third area. Finally, origami engineering is introduced as a potential structural solution.

Chapter 3 proposes a new concept of origami concave tubes for energy absorption, which leads to a series of designs of origami concave tubes. Numerical simulation, experiments, theoretical modelling, and parametric study were carried out for two specific designs of origami concave tubes. Comparisons were made with traditional square tube and normal concave tubes, which showed that the new designs could achieve desirable performance with more than 3 times energy absorption of square tube.

Chapter 4 proposes to use thin corrugated tubes for inversion instead of circular tubes. Numerical simulations, experiments, and theoretical modelling were done. Comparisons of inversion of thin corrugated tubes and circular tubes were made both numerically and experimentally. It presented that corrugated tubes could be stably inverted with frictional contact and geometrical imperfection, while circular tubes buckled.

Chapter 5 presents a series of designs of origami bending devices for energy absorption, including beams, panels, arches, and shells. Numerical simulation and experiment were carried out. Comparisons in both numerical simulation and experiment of origami bending devices with a commercial bumper beam were carried out, and it showed that origami bending devices achieved more consistent reaction force and overall higher energy absorption.

Conclusions and future work are given in Chapter 6, which ends the thesis.

Chapter 2 Literature Review

2.1 General Principles of Energy Absorbers

An ideal energy absorption device should meet the following requirements (Lu and Yu, 2003):

- Irreversible energy conversion to avoid a second impact caused by energy release.
- Long stroke to allow large plastic deformation.
- Stable and repeatable deformation mode to ensure predictable performance in an event of impact.
- Restricted and constant reactive force so that no excessive force is transmitted to the main structure that the device is to protect.
- High energy absorption to absorb as much energy as possible, accompanied by light-weight for easy installation.
- Low cost as the device often gets destroyed in an impact and needs replacement.

To evaluate the energy absorption performance of a device, two parameters are extensively used: the specific energy absorption (SEA), defined as the energy absorption per unit mass, and the load uniformity, which is the ratio between the peak and the mean crushing forces. Here the peak force is the highest reaction force during the crushing process and the mean crushing force equals to the total energy absorption divided by the final crushing distance. Lower load uniformity indicates that relatively less peak deceleration is produced in the impact, which better prevents concussion of the passengers.

2.2 Thin-walled Tubes Buckling for Energy Absorption

Thin-walled structures are amongst the most commonly used energy absorption devices due to their good energy absorbing ability, excellent manufacturability and low cost.

In automobiles, thin-walled tubes made of square and rectangular cross-sections, are widely used as crashcans. Similarly, thin-walled square tubes are also used in front of trains for energy absorption (Xie and Zhou, 2014). In helicopters, circular tubes have been used as the landing gears for their good crashworthiness when axially compressed (Airoldi and Janszen, 2005). The tubes are often relatively short to avoid global Euler buckling.

2.2.1 **Thin-walled Circular Tubes**

Extensive research had been done in the past to understand the performance of thin-walled tubes with circular or square sections when subjected to axial compression. For stocky circular tubes, the classical theory (Timoshenko, 1961) predicted the bellow buckling mode, see Figure 2.1(a). In this mode, the material of circular tube bulges out and dents in axisymmetrically. Later, it was found (Allan, 1968) that there were actually two failure modes, depending upon the diameter to wall thickness ratio. Relatively thick tubes (ratio of diameter to thickness smaller than 90) failed by material yielding which led to the bellow mode, and relatively thin tubes (ratio of diameter to thickness larger than 90) failed elastically in the diamond mode (Guillow et al., 2001), Figure 2.1(b). In the diamond mode, the cross-section of circular tube deforms into series of polygonal shapes. The mean crush force of below mode can be expressed as (Singace et al., 1995)

$$P_m = \sigma_0 (5.57 t^{\frac{3}{2}} D^{\frac{1}{2}} + 1.41 t^2) , \qquad (1)$$

where σ_0 is the effective plastic flow stress of the material, t is the wall thickness, and D is the diameter of the tube. Theoretical modelling of the diamond mode is more complex, which can be expressed as

$$P_m = \frac{\sigma_y}{2\sqrt{3}}\left[\frac{2\pi^2}{m_0}\tan\left(\frac{\pi}{2m_0}\right)D\cdot t - \frac{m_0\cdot\pi}{3}t^2\right], \qquad (2)$$

where σ_y is the yielding stress of the material, and m_0 can only be determined by experiments.

The circular tubes have been used as energy absorption devices (Abramowicz and Jones, 1986) because of their high SEA and low cost. However, they have unfavourably high load uniformity. To overcome this problem, lateral compression (Reddy and Reid, 1980) or indentation (Lu, 1993) on circular tubes had been attempted which could reduce the load uniformity, but it was accompanied by lower SEA. A number of other approaches were also reported in which additional components were utilised to cause thin-walled tubes to be inverted (Miscow F and Al-Qureshi, 1997) or split (Reddy and Reid, 1986). Tube inversion can produce high SEA accompanied by low load uniformity. Splitting gives low load uniformity. However, special dies are needed to activate the specific deformation modes in both inverting and splitting.

2.2.2 **Thin-walled Tubes with Square Sections**

Like circular tubes, stocky square tubes also exhibit various failure modes depending on the width to thickness ratio. Very thin tubes usually fail in the non-compact mode (Reid et al., 1986), Figure 2.1(c). Tube fails in this mode is not folded down compactly, and is undesirable from the perspective of energy absorption, because Euler buckling could jump in, and this would considerably reduce the energy absorption capability. Tubes with moderate thickness normally fail in the symmetric mode, Figure 2.1(d). In this mode, square tube folds down layer by layer and forms a compact structure. The mean crushing force of symmetric mode can be expressed as (Wierzbicki and Abramowicz, 1983)

$$P_m = 9.56\sigma_0 t^{\frac{5}{3}} c^{\frac{1}{3}}, \tag{3}$$

where c is the width of the tube. Since the effective crushing length is about 70% of the total length of the tube (Abramowicz, 1983), P_m for a square tube can be rewritten as

$$P_m = 13.66\sigma_0 t^{\frac{5}{3}} c^{\frac{1}{3}}. \tag{4}$$

Effective crushing length is the actual crushable displacement that the tube has, which is smaller than the tube length itself due to the existence of the uncrushable remaining. For some width to thickness ratios, asymmetric modes could also occur (Abramowicz and Jones, 1984). The load uniformity of square tubes is also very high.

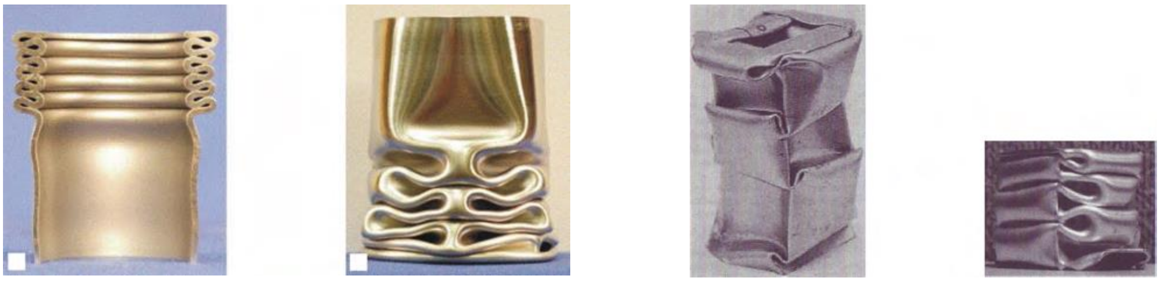

(a) (b) (c) (d)

Figure 2.1. Circular and square tubes under axial compression (Bardi and Kyriakides, 2006). (a) the bellow mode (Guillow et al., 2001); (b) the diamond mode (Bardi and Kyriakides, 2006); (c) the non-compact mode (Reid et al., 1986); and (d) the symmetric mode (Reid et al., 1986).

2.2.3 Circular and Square Tubes with Geometric Discontinuity

A simple but effective method of reducing load uniformity is to introduce some sort of geometric imperfections to the tube, also known as the geometric discontinuity. Buckling initiator was manufactured at the top of the square tube to reduce the initial buckling force, and to preserve the energy absorption in (Zhang et al., 2009). The laterally corrugated circular tube was proposed in (Chen and Ozaki, 2009), leading to lower load uniformity, but slightly lower SEA than that of a regular circular tube. Placing appropriate spacing of lateral grooves on circular and square tubes (Hosseinipour and Daneshi, 2003), which provides local structural imperfection and can lead to designed failure modes, could reduce the load uniformity and slightly increase SEA. A similar way (Adachi et al., 2008) to increase SEA of circular tubes but with more significant improvement was to add lateral ribs with an appropriate spacing in a circular tube to trigger the bellow mode (axisymmetric failure). However, there was no improvement to the load uniformity.

2.2.4 **Thin-walled Tubes with Concave Sections**

A significant amount of research has been done on the energy absorption of the axial crushing of thin-walled tubes with concave cross-sections (such as Figure 2.4(b) and (c)). Tubes with different convex and concave cross-sections have been studied (Fan et al., 2013, Tang et al., 2012, Liu et al., 2015, Reddy et al., 2015), which showed that concave tubes have great potential for high energy absorption. However, concave tubes have unstable features which suggest that material always bulges out laterally when compressed as shown in Figure 2.2, instead of buckling progressively. Progressive buckling of tubes gives periodic folding of material as shown in Figure 2.1(a), (c), and (d), which correspondingly brings periodical reaction response. A simple solution for this unstable problem with experimental validation has not been provided yet.

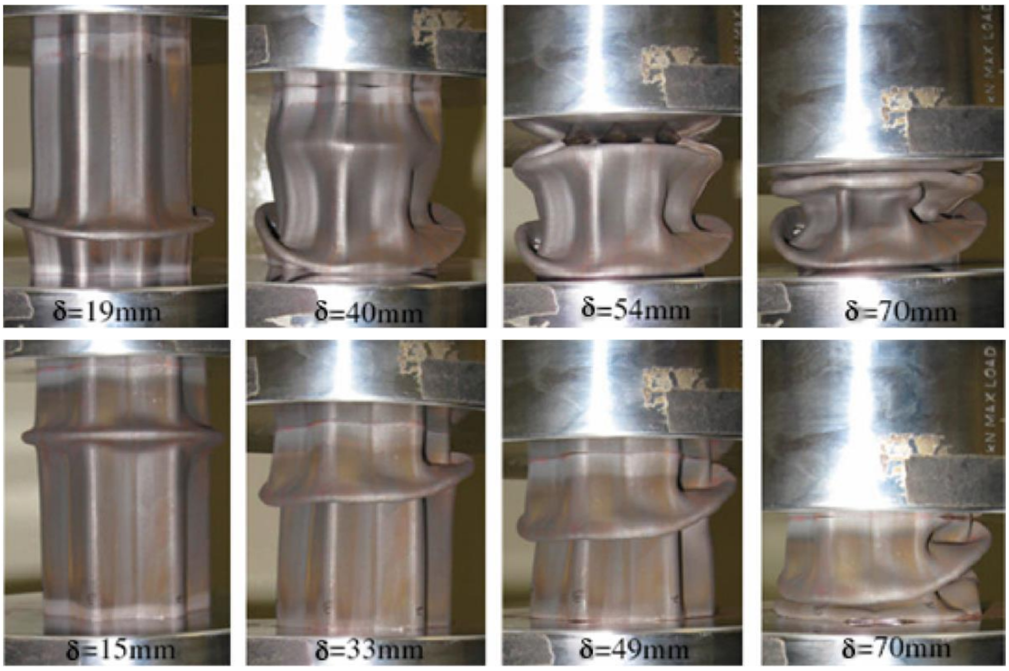

Figure 2.2. Experimental crushing of thin-walled tubes with concave cross-sections.

Buckling force of short thin-walled tubes has also been well studied. Generally, cross-section with shorter width gives higher specific buckling force. For instance, a six-sided polygonal tube has a higher buckling force than a square tube, but smaller than a circular tube with the same circumference. Tubes with concave cross-sectional shapes (such as corrugated shape) have largest buckling load (Ma, 2011, Ning and Pellegrino, 2013). A higher buckling force indicates its capability to support failure mode with higher energy absorption.

It was pointed out that the corners of a square tube absorb two-thirds of energy during the crushing process (Wierzbicki and Abramowicz, 1983, Ma and You, 2013b). In consequence, energy absorption can be enhanced by increasing the number of corners of the tube, as shown in Figure 2.3. When the number of corners is increased to a limit, corners become too shallow to be distinguishable mechanically, which eventually leads to a circular shape and approximately 50% higher energy absorption compared to the square tube (Ma, 2011; Lu, 2003). These indistinguishable corners are ineffective mechanically. Another way of increasing effective corners is by introducing concave shapes to the cross section, shown in Figure 2.4.

This method seems to be more promising since it has no limit of the number of corners. However, even though with their high buckling load and potentially high energy absorbing failure mode, concave shaped tubes cannot usually buckle progressively to achieve high energy absorption. Instead, sides of tubes often bulge out (Figure 2.2) which gives them similar energy absorption to the circular tube and very high peak load (Fan et al., 2013).

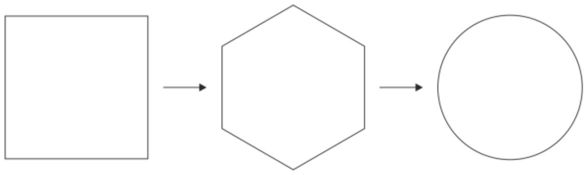

Figure 2.3. Shape changes from square to polygon and to circle.

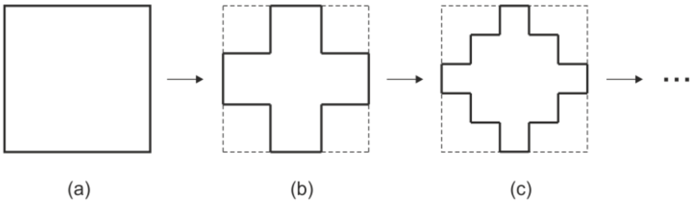

Figure 2.4. Shape changes from square to concave shapes.

2.2.5 Other Thin-walled Tubes

Thin-walled tubes with different sectional profiles were extensively examined for their energy absorption capability. A circular tube has higher SEA than that of a square tube of identical surface area and thickness, but the former is associated with a high initial buckling force which is not easy to be reduced without compromising the energy absorption efficiency, and tubes with concave cross-section suffer from unstable failure mode. Polygonal tubes, normally having hexagonal or octagonal cross sections, (Abramowicz and Wierzbicki, 1989) are therefore often regarded as a trade-off between square and circular tubes. Frusta (or tapered tube) has a low initial buckling force and stable force vs displacement response, and high energy absorption capability when subjected to oblique loads compared with that of straight tubes, but still less efficient under axial load (Reid and Reddy, 1986, Mamalis et al., 1996). Tubes with a cellular cross section, in general, have better energy absorption ability than that of single-cell tubes such as circular or square tubes discussed earlier. Because SEA increases with the decrease of the ratio of width and thickness, the introduce of cellularity decrease the width leads to better energy absorption (Chen and Wierzbicki, 2001). A typical example is the honeycomb structure (Wu and Jiang, 1997) which is widely used as core structure of sandwich panels. However, the cellular tubes still have a high initial buckling force and more expensive.

Tubes with undevelopable surface, i.e. they cannot be made from a flat sheet without stretching the sheet, bring new collapse modes which increase energy absorption. Appropriately designed longitudinal grooves on square tubes, Figure 2.5, could either reduce peak force by a quarter or increase SEA by over three quarters (Zhang and Huh, 2009). However, it cannot achieve both merits with considerable improvements at the same time. Pyramid pattern was introduced to the surface of the square tube, resulting in an increase of SEA by more than 50%, accompanied by a slight reduction of initial buckling force (Zhang et al., 2007) according to numerical simulation, Figure 2.6. However subsequent experiment showed that triggering of this failure mode was rather inconsistent (Ma, 2011).

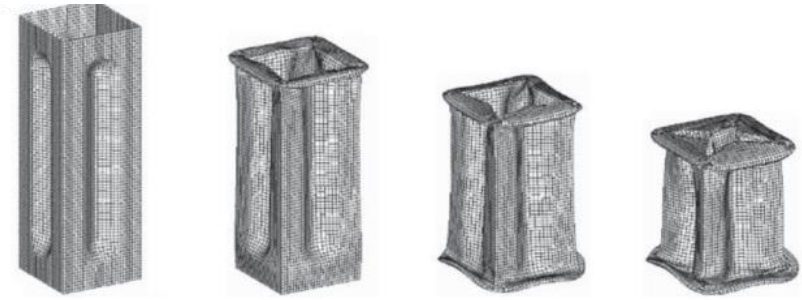

Figure 2.5. Deformation sequance of a square tube with longitudinal grooves under axial compression.

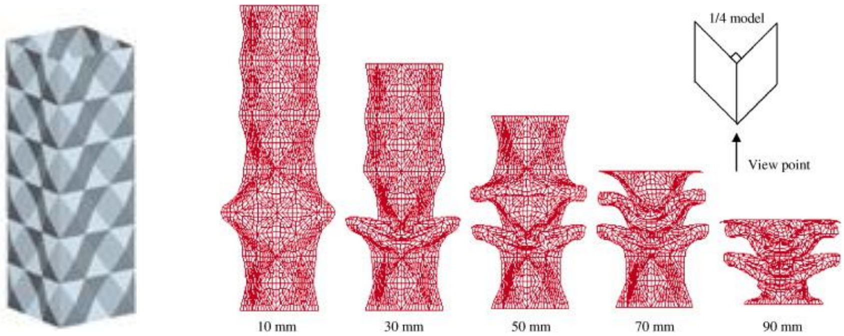

Figure 2.6. Deformation simulation of a square tube with pyramid pattern under axial compression.

2.3 Circular Tube Inversion

Tube external inversion using a die is a process that a tube, which is subjected to compression, rolls up and undergoes inside-out inversion with the help of die, as shown in Figure 2.7. This process can be used for energy dissipation, which has very high and stable reaction force.

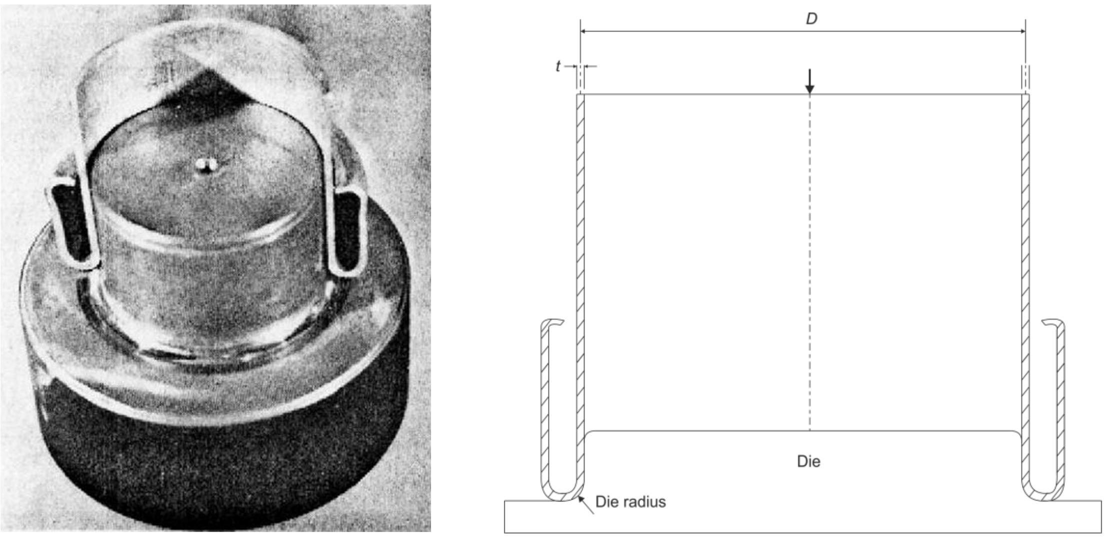

(a) Experiment (Al-Hassani, 1972)

(b) Schemetic diagram

Figure 2.7. Illustration of Tube Inversion.

Extensive experimental and theoretical studies were performed on external tube inversion process using a die (Reid, 1993, Rosa et al., 2004, Sekhon et al., 2003, El-Domiaty, 1997). Successful tube inversion has a strict requirement for various conditions. Four controlling factors were summarized by Rosa (Rosa et al., 2004), which are D/t, r_{die}/R, μ, and strain hardening exponent, where D is the diameter of the tube, t is its wall thickness, r_{die} is the die radius shown in Figure 2.7(b), R is tube's cross-section radius, and μ is friction coefficient. Failing to satisfy appropriate values of those factors will result in either fracturing or buckling of the tube other than inverting. The solution for fracturing is straight forward, which requires smaller die radius (less circumferential stretch) and larger elongation of material. Elongation is equivalent to ultimate strain. However, eliminating the occurrence of buckling requires a careful assignment of all four factors, which essentially makes sure that the buckling load of the tube is higher than the load required for a successful inverting process, so that inverting can occur prior to buckling. Some successful tube inversion examples are shown in Table 2.1.

Table 2.1: Examples of successful tube inversion.

Authors	D/t	r_{die}/R	Friction coefficient μ
Rosa (Rosa et al., 2004)	18	0.21-0.42	0.02
Reid (Reid, 1993)	31.25	0.16-0.24	Lubricated
Sekhon (Sekhon et al., 2003)	33.07	0.16-0.27	Graphite Lubricated
	37.46	0.12-0.21	Graphite Lubricated
	29.12	0.12-0.29	Graphite Lubricated
Gupta (P. K. Gupta, 2013)	33.07	0.16-0.27	Graphite Lubricated
	29.12	0.20-0.29	Graphite Lubricated
	37.46	0.21-0.29	Graphite Lubricated

Definition of thin wall tube is $D/t > 20$ (Reid, 1993). From Table 2.1, D/t of tubes range from 18 to 37.46, which are all quite thick tubes. All successfully inverted tubes used lubrication, which decreased the load needed for inversion to a lower value than its buckling load. Failure of lubrication can increase μ from 0.02 to 0.4 (Rosa et al., 2004), and local buckling will easily take place (Rosa et al., 2004, Sekhon et al., 2003).

Concluded by (El-Domiaty, 1997), larger D/t allows smaller r_{die}/R, which is also reflected in Table 2.1. Tube inversion with smaller r_{die}/R is less likely to fracture (Sekhon et al., 2003). This gives one reason for favouring tubes with larger D/t.

Theoretical models of buckling and inverting forces of circular tubes were proposed respectively. Buckling stress σ_{cl} of linear-elastic thin tubes with perfect geometry can be calculated as (Brush and Almroth, 1975)

$$\sigma_{cl} = \frac{2E}{\sqrt{3(1-v^2)}} \cdot \frac{t}{R} \tag{5}$$

where E, v, R, and t are the Young's modulus, Poisson's ratio, radius of tube, and shell thickness, respectively. Inverting stress can be written as (Lu and Yu, 2003b)

$$\sigma_{inv} = 2 \cdot \sigma_y \cdot \sqrt{\frac{t}{R}} \tag{6}$$

where σ_y is the material yield stress. It can be concluded from Equation (5) and (6) that σ_{inv} decreases faster than σ_{cl} when t/R ($< 1/4$) decreases.

Comparison between buckling and inverting load with different D/t ratio done by (El-Domiaty, 1997) also agreed with this conclusion. It showed, when D/t increases, σ_{inv} decreases faster than σ_{cl}. This means that tubes with larger D/t (smaller t/R) should be easier to be inverted. However, perhaps due to the experimental inconvenience, no study has been found about tube inversion with $D/t > 50$, which is also common D/t range for thin-walled tubes in practice.

However, further consideration differs that conclusion. Thinner circular tubes are more sensitive to imperfection (Jones, 2006), and this largely reduces the actual buckling force of the tube, which will again make the tube more likely to buckle. A simple way of evaluating actual buckling force of thin tubes is by applying a knockdown factor (Jones, 2006), and its expression is

$$\gamma = 1 - 0.901(1 - e^{-\frac{1}{16}\sqrt{\frac{R}{t}}}) . \tag{7}$$

The plot of Equation (7) and experimental knockdown factors are shown in Figure 2.8. One solution for increasing knocked down buckling force is to introduce corrugation to its cross-section (Ning and Pellegrino, 2013), which not only reduces the imperfection-sensitivity, but also increases the buckling load per weight of the tube.

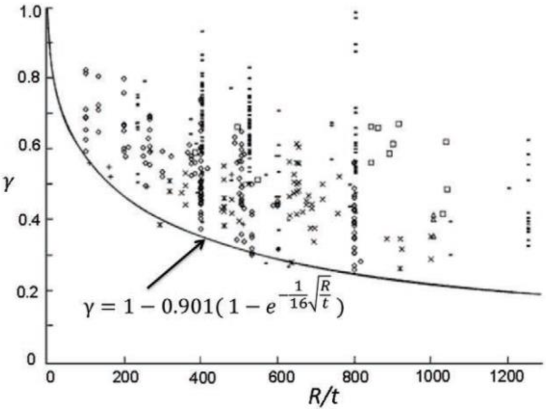

Figure 2.8. Experimental knockdown factors of cylindrical shells under axial compression and the empirical curve for the knockdown factor (Jones, 2006).

2.4 Bending Devices for Energy Absorption

The frame of vehicles, which is primarily consisted of thin-walled open-section beams and arches, is used to protect passengers during crash accidents, shown in Figure 2.9(a). It is designed to absorb kinetic energy through large plastic deformation when subjected to impact loadings. Though existing open-section beams and arches often experience large plastic deformation in a collision and are widely used, these designs have their limitations.

Compared with thin-walled tubes under axial compression, common thin-walled beams have a relatively low SEA. The low energy absorption efficiency is caused by the lateral bending collapse mode of thin-walled beams which usually features a limited number of localised plastic hinges during the crushing process, and therefore only a small amount of material in the neighbourhood of the hinges undergoes large plastic deformation (Lu and Yu, 2003). Box-sectional and open-sectional beams were used as bumper beam (Jonsson and Juntti, 2005). It undergoes the plastic deformation described above, followed by local flattening at those plastic hinges. Steel and aluminium alloy are commonly used materials because of high machinability and low cost.

Attempts were made to alter the lateral bending collapse mode of conventional beams by introducing tension components to trigger membrane deformation in curved beams (Carpenter, 1990, Schwartz and Ramoo, 1999). While having higher energy absorption, this type of beam is also heavier and does not integrate well with the main structure of a vehicle.

The beam or arch sections tend to be flattened in large deformation, and result in localized deformation with reduced bending resistance, and this phenomena is called as Brazier’s effect (Calladine, 1989), shown in Figure 2.9(b). This effect leads to high initial reaction but low overall energy absorption. In contrary to the performance of existent beams and arches, ideal energy absorbers require high specific energy absorption (SEA) which is defined as the energy absorption per unit mass, and low load uniformity (LU) which is defined as peak load divided by mean crush load (Lu and Yu, 2003).

(a) (b)

Figure 2.9. (a) Frame of vehicles and (b) thin-walled beam bending.

Bending behaviour of thin-walled beams has been extensively investigated using numerical, experimental and theoretical analysis. Failure behaviour of beams under impact is comprehensively summarized by Lu and Yu (Lu and Yu, 2003). Wierzbicki and Abramowicz (Wierzbicki and Jones, 1989) developed analytical models which give a reasonably accurate prediction of their energy absorption capability. Additional to extensive analysis, improvement of energy absorption of closed-section thin-walled beam was carried out through geometric modification using origami technique and showed good results (Ma and You, 2013a). However, relatively little has been done to improve the performance of open-section beams and arches.

2.5 Origami Engineering

It has been mentioned that origami technique, which involves borrowing geometries from origami folding, is effective in bringing new initial configurations and failure modes into thin-walled structures for higher energy absorption (Ma and You, 2013a). Origami is originally a traditional art form of paper folding that leads to the creation of intricate and fascinating. In recent decades it has been of increasing interest to mathematicians and engineers. Mathematicians are more interested in the geometrical aspects of origami objects, which are assumed to have zero thickness, such as rigid and flat foldability. Origami with rigid foldability is a small subset that permits continuous motion between folded states along the pre-determined folding creases without the need for twisting or stretching of the facets. Origami folding which satisfies flat foldability means that it can be folded down into one plane. Engineers, on the other hand, are finding that traditional geometry and folding used for artistic paper models can be readily parameterised and applied to the development of new mechanisms, structures and all sorts of devices. Since most of the sheet materials used in engineering applications are relatively thin and rigid, which are much easier to be bent than stretched, particular attention has been drawn on to rigid origami. Rigid foldability allows the origami structures to be readily manufactured from modern sheet materials such as plastic, metal, or carbon-fibre sheets, producing structures that are sufficiently strong and durable to be of use in large-scale applications. This type of patterns is also ready to produce foldable mechanisms for applications like deployable structures.

Artists have created many origami patterns. Some of the patterns, the repetitive patterns known as tessellation patterns in particular, can be used to fold novel plates and tubes. A number of methods and patterns were explored (Nojima, 2002), which can give closed cylindrical tube shapes. These tubes could neatly collapse by rotating one end of the tube against the other, making them suitable for applications as space masts. The origami pattern most frequently used in engineering structures is Miura pattern, which is a four-creases rigid and flat foldable folding, shown in Figure 2.10. Applications of origami mainly lay in two fields, which are respectively mechanisms and structures.

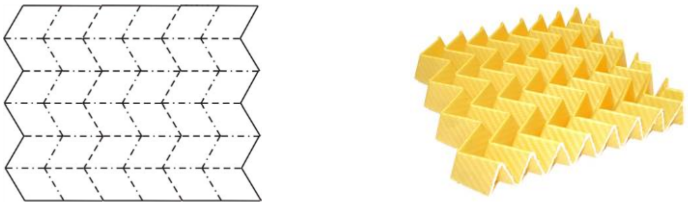
(a) (b)

Figure 2.10. (a) Folding pattern of Miura pattern and (b) its folded form.

2.5.1 **Origami for Mechanisms**

The most direct engineering application of rigid origami is to produce mechanisms or foldable structures. Origami with no thickness is essentially a series of spherical linkages, and can naturally form shell structures when deployed. Extensive analysis and modelling have been done for this motion of origami mechanisms with assumption of zero material thickness (Belcastro and Hull, 2002, Wu and You, 2010). Controlling quantitative constraints were summarized for typical origami patterns with one degree of freedom for the convenience of future design (Gattas et al., 2013). These origami mechanisms can be used for space applications such as solar panel or telescope (Lang, 2001), which can be compact during delivery and spacious when deployed. On a smaller scale, Kuribayashi and You (Kuribayashi et al., 2006) developed a novel folding aortic stent graft by introducing a helical folding pattern into a membrane tube, resulting in a structure that has an overall negative Poisson’s ratio, allowing uniform expansion and contraction of the stent, shown in Figure 2.11. Also, robots (Felton et al., 2014), and tents or shelters (Lee and Gattas, 2016) can be made using origami mechanisms. Recently, construction of origami of thick panels based on the analogy to Bennet (4 bars) and Bricard (6 bars) linkages was proposed, which revolutionarily gives a general way of designing thick origami panels (Chen et al., 2015).

Figure 2.11. A novel origami folding aortic stent graft.

Different features of origami mechanisms were explored and utilized. Bifurcation, which enables mechanisms to switch the motion path at certain positions, was used for achieving reconfigurable cross-sections for one pre-designed deployable origami tube (Filipov et al., 2016). Combining several folded structures repetitively can often create a type of deployable structures, which can be easily opened in certain ways while resistant to other movements (Evgueni T. Filipov, 2015, Schenk, 2011). All these lead to various developments in deployable structures.

2.5.2 **Origami for Structures**

Another engineering application of origami is to create structures with a desirable or even reprogrammable mode of deformation and reaction response. Traditional structures are mostly designed for load bearing applications, which normally have similar reaction response to Figure 2.12 with high buckling force and uncontrollable post-buckling reaction response. Altering initial geometry of thin-walled structures can give them designed buckling modes with desired reaction responses. One application is for energy absorbers, which essentially desires maximum area beneath reaction curve and low buckling force. Recently, origami technique has been applied to change the surface geometry of thin-walled structures with the aim to increase the overall energy absorption (Ma and You, 2013b, Gattas and You, 2014, Gattas and You, 2015, Ma and You, 2013a). They found that by pre-folding thin-walled surfaces a desirable failure mode could be triggered.

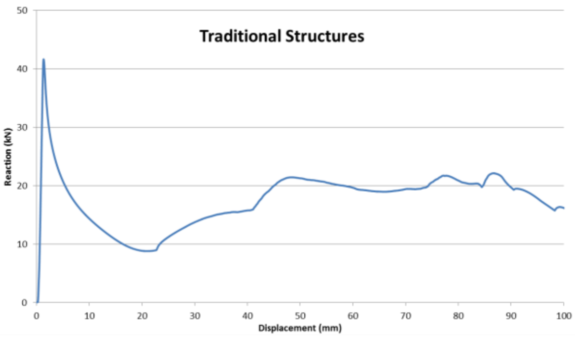

Figure 2.12. Reaction response of traditional structures.

The energy absorption capability of tubes generated using Miura and its associated patterns were examined and found that, by appropriately placing the basic folding units, good load uniformity could be achieved and reactive force could be maintained at more or less constant level during the crash process (Wu, 2010). Ma (Ma, 2011) developed an origami tube in which an origami pattern has been used to pre-fold the surface of a square tube. The origami pattern for one of the units is given in Figure 2.13(a). The pre-folded shape enables a more particular failure mode, known as the diamond mode, being trigged when subjected to axial compression. In fact, the formation of the mode is due to the fact that the tube follows the pre-folded shape when it is crashed down, as shown in Figure 2.13(b) simulation. In comparison with the conventional square of the identical surface area and thickness, this origami tube has over 50% higher SEA and excellent load uniformity. Ma showed that the origami shape acts as an inducer to trick the tube deforming into a pre-determined shape which is associated with high energy absorption. This example proves that origami can be used as a structural design tool to alter failure modes. Ma also extended the concept to closed-sectional beams and created an origami beam using the same unit from his origami tube. The slightly curved beam, intended for bumper beams of transport vehicles, outperformed the beam with a square section by 20% in terms of SEA. In the origami beam, the plastic deformation was no longer localised. In fact, the entire beam experienced various level of plastic deformation.

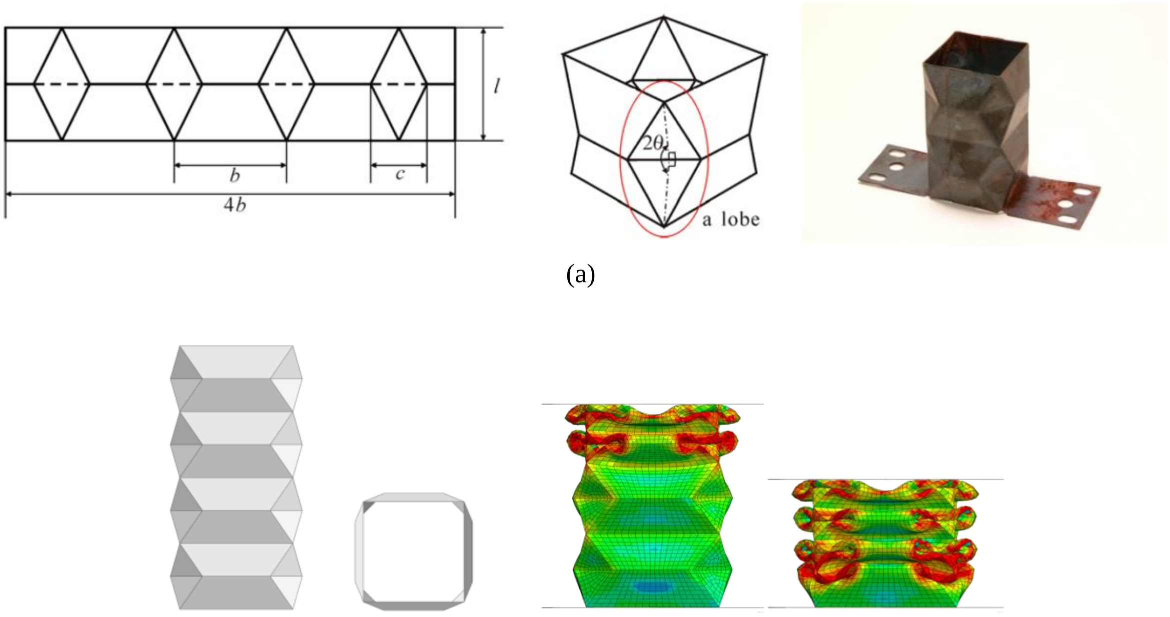

(a)

(b)

Figure 2.13. The origami crash tube. (a) Origami pattern of the origami tube; and (b) the simulation results of the crashing process.

More recently, Miura patterns have been used to produce core structures of sandwich panel, which are easy to make, have good shape flexibility in comparison with the honeycomb core, and are open channel allowing ventilation. Figure 2.14 shows an example of core structure for sandwich panels (Gattas, 2013). This same pattern with different orientation has also been used for the core of sandwich beams for blast-resistance (Schenk et al., 2014a). However, no effort has been noticed for solving structural depth reduction problem which is explained in Section 2.4, shown in Figure 2.9(b).

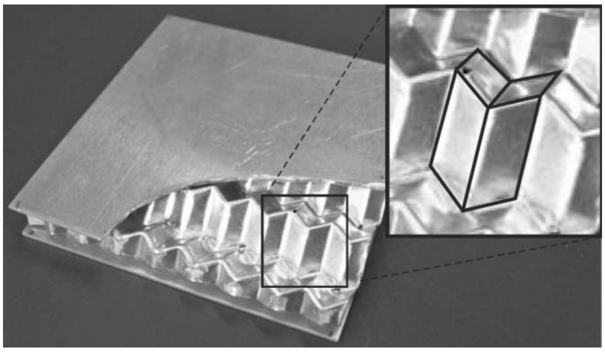

Figure 2.14. Miura pattern for the core-structure of sandwich panel.

Other applications of origami structures were also studied. Another application is for nonlinear spring for vibration isolation, which requires reduced slope of stiffness in the middle of compression (Ishida et al., 2014). Special deformation modes are preferred in certain applications and can be achieved by origami, such as negative Poisson’s ratio (Lv et al., 2014, Yasuda and Yang, 2015, Kuribayashi et al., 2006a). Bi-stability (Silverberg et al., 2015, Gattas, 2013) and re-programmability (Silverberg et al., 2014) of origami structures were reported, which shall lead to wider applications in the future. Origami structures give engineers more design parameters and better control of their performance in large deformation.

2.6 Finite Element Analysis and Abaqus

In order to assess the performance of energy absorbing structures, proper method of analysis should be applied. Finite element analysis (FEA) is the most used numerical method of solving highly non-linear structural problems, such as thin-walled structures that undergo large deformation. Abaqus (Abaqus, 2013) is one of most popular commercial FEA softwares, which has been proven to be accurate for the simulation of crushing energy absorbing structures (Gattas, 2013), and it is employed in this thesis. The explicit solver provided by Abaqus is used in this research, which provides good accuracy and convergence for highly non-linear quasi-static problems (Ma, 2011). In this solver, the explicit dynamic integration method (also known as the forward Euler or central difference algorithm) is used and the load is assumed to be time-dependent, in which dynamic equilibrium of the system is formulated and solved in each time step, and then equations are iterated through time. It is important to ensure insignificant inertia effect in a quasi-static study and practical processing time by setting reasonable time period for the analysis. Abaqus offers different types of element, in which shell element is the most appropriate choice for thin-walled structures. S4R and S3R elements, which respectively refer to quadrilateral and triangular elements with reduced integration, are most commonly used in problems involving large strain. Since S4R is robust while S3R may suffer shear-lock problem, S4R element is dominantly used in this research while S3R element is only employed when usage of only S4R element is not possible for the geometry. Abaqus/Explicit offers two methods for modelling contact: general contact and contact pairs. General contact is used in this research, since it automatically involves interaction of all bodies and surfaces in the model. In contact pairs, individual surface pairs need to be specified manually. Penalty method provided in general contact is used for contact constraint.

2.7 Summary

Mainly three challenges for further enhancement of energy absorption of structures have been presented in this chapter. Tubes with concave cross-section have multiple effective angles and high buckling force which imply their potential for high energy absorption. However, they usually fail in a non-progressive manner, and this makes them unsuitable for energy absorbers. Inversion of circular tubes consume an enormous amount of energy, but this process is very unreliable due to the tendency of buckling. Inversion can occur only under various conditions, such as good lubrication, which makes it less practical. Thin-walled beams often suffer flattening of their structural depth in large deformation, and this causes significant reduction of bending stiffness. This makes them less ideal for absorbing energy.

Solving these problems is potential to dramatically improve the performance of these energy absorbing structures.

Chapter 3 Origami Concave Tubes

This chapter presents the designs of various tubes with concave cross-sections which have a stable progressive buckling mode when they are subjected to axial compression. Origami technique, which borrows developable geometry from origami folding, has been employed to generate such designs. In this chapter, the geometry of origami concave tubes is specified first. Experiments of different tubes followed with corresponding numerical simulations are presented afterward. Finally, theoretical modelling, parametric study, and different loadings of origami concave tubes are researched.

3.1 Geometry of Concave Tube and Modification

Two concave tubes are shown in Figure 3.1(a), (b), (d), and (e) respectively. One of the ends of each tube is slightly bent to create an origami initiator, which can be seen in Figure 3.1(c) and (f) respectively. Origami initiator is designed to initiate progressive buckling. They are manufactured from a single sheet metal using the origami patterns given in Figure 3.2, which consist of a set of mountain (solid line) and valley creases (dash line). These are rigid origami patterns, i.e., continuous folding can be carried out by folding along the creases without stretching the sheet. Stretching of material can bring difficulty in the manufacturing process. Concave tubes can be obtained once edges AB meets A’B’ and BC meets B’C’. Such tubes have the same surface areas as those of the corresponding square tubes, but it is expected that the increase of corners could lead to a failure mode with higher energy absorption capability. The geometry of origami concave tubes is determined by five independent parameters. α, the pattern angle, l_1, the length of the straight part of the tube, l_2, the length of the inclined part, w, the width of edge, and t, the wall thickness of the sheet, which are all noted in Figure 3.2.

Tubes with the shape shown in Figure 3.1(b) are named as *O*1 *concave tubes* (O1 stands for order 1), and correspondingly tubes in Figure 3.1(c) are named as *O*1 *origami concave tubes*. *Order* here is to imply the number of corrugations in the cross-section. Similarly, tubes shown in Figure 3.1(e) and (f) are named as *O*2 *concave tubes* and *O*2 *origami concave tubes* respectively.

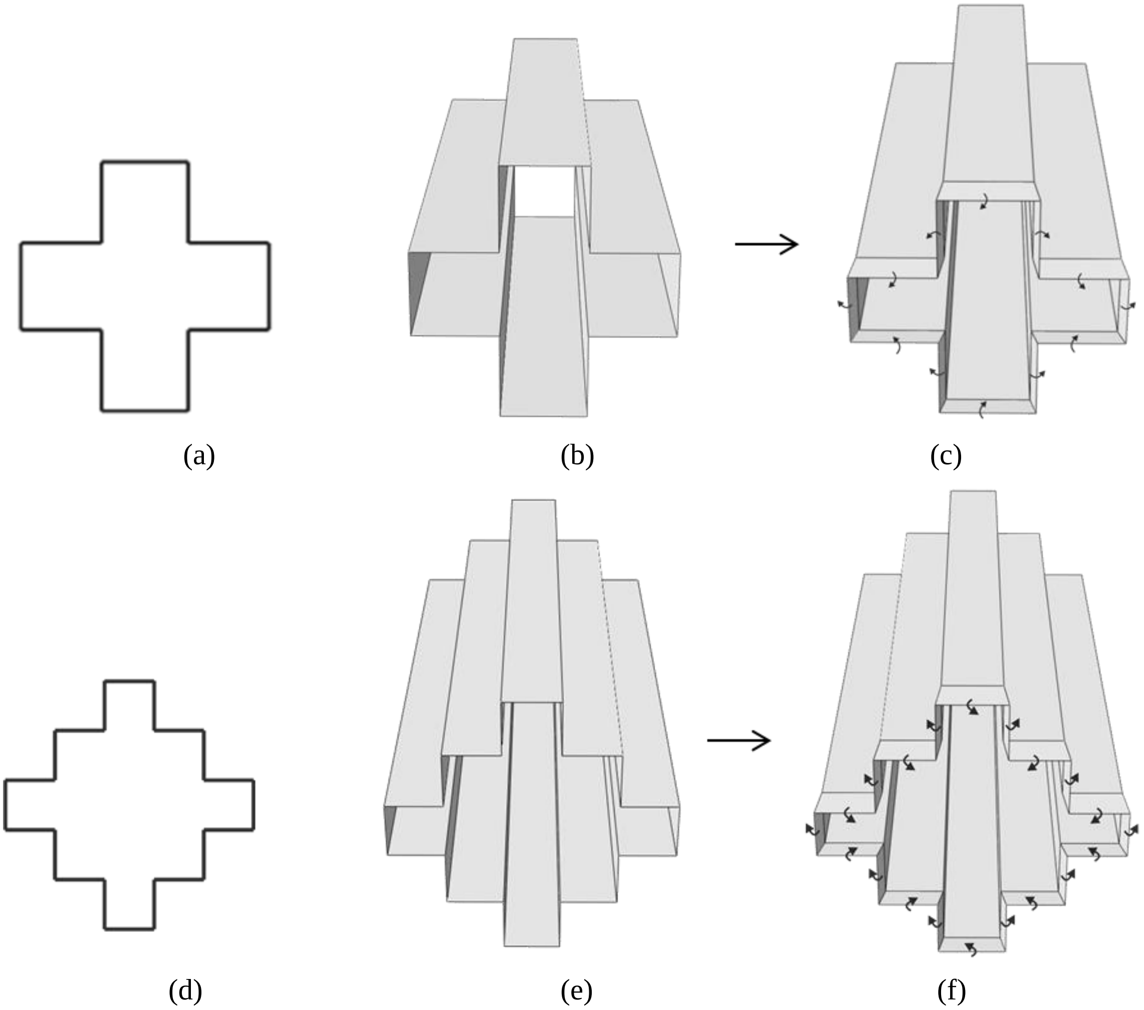
(a) (b) (c)

(d) (e) (f)

Figure 3.1. Method of generating origami concave tubes: (a) cross-section of one concave shape; (b) tube made out of cross-section in (a); (c) origami initiator added into tube in (b); (d) cross-section of another concave shape; (e) tube made out of cross-section in (d); and (f) origami initiator added into tube in (e).

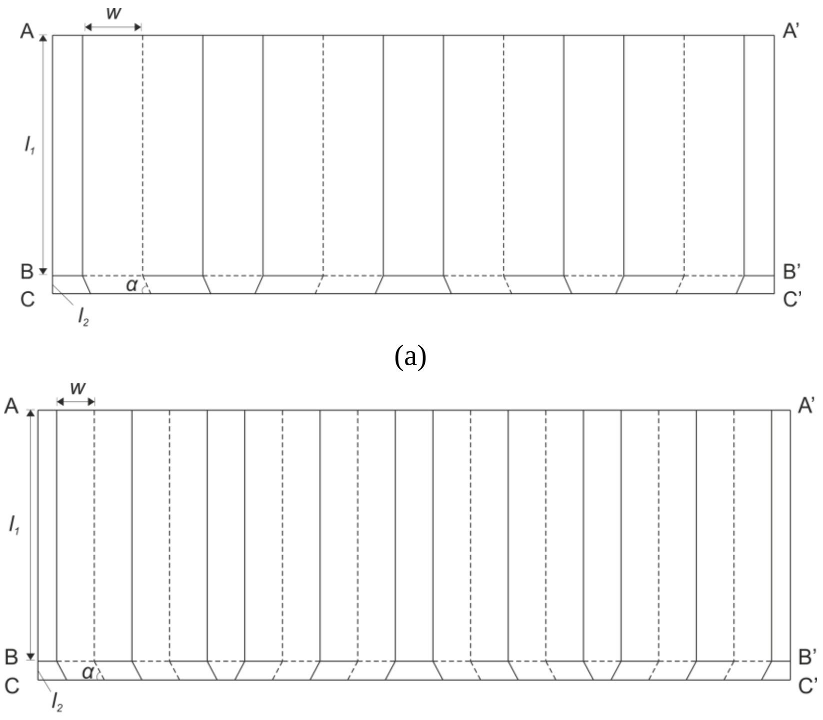

(a)

(b)

Figure 3.2. Folding patterns of (a) the first and (b) second origami concave tubes.

3.2 Experimental and Numerical Studies

3.2.1 Manufacturing and Experiment Setup

5 types of tubes were manufactured, which were the square tube, O1 concave tube, O1 origami concave tube, O2 concave tube, and O2 origami concave tube.

Dimensions of the cross-section of tubes are shown in Figure 3.3. Total tube length was set as 150 mm. Each tube was spot welded from four smaller pieces with 15 mm overlap to each other, which left the tube with four 15 mm thicker parts that are marked black in Figure 3.3. All tubes were welded to two rigid plates by four tabs at each end, and positions of those tabs were at overlapped and thicker part of tubes, shown in Figure 3.4. Parameters for the prototypes are given in Table 3.1. The material used was 304 stainless steel sheet. The dog-bone samples were cut off from the sheet and tested (in Figure 3.5(a)). The averaged stress-strain curve is shown in Figure 3.5(b). It has density ρ = 8030 kg/m^3, young's modulus E = 193 GPa, yield stress σ_y = 241.3 N/mm^2, ultimate stress σ_u = 679.6 N/mm^2, ultimate strain ε_u = 55.8%, and strain hardening formula $\sigma = 1400\varepsilon^{0.43}$ (Callister, 2005).

The tube prototypes were made through a series of bending and spot-welding processes. For example, for O2 origami concave tube, four pieces of stainless steel were cut, and bent into a "w" shape, shown in Figure 3.6(a) and (b). Then four w-shaped pieces were spot welded together which gave a concave tube shown in Figure 3.6(c) and (d). After that, one end of the concave tube was bent manually by a spanner, which formed the origami initiator seen in Figure 3.6(e) and (f). Finally, the tube was welded to two steel plates with four 15 mm tabs at spot welded positions each end, shown in Figure 3.6(g). The other tubes were made similarly except no origami initiators were made when they were not present in designs. The material used has good ductility, and residual stress from manufacturing process was very small comparing to the stress experienced during the crushing process. Practical imperfection was generated in these tubes from manufacturing and welding process.

Three different testing methods were used because the buckling load of some specimens exceeded the limit of the load cell installed in the Instron machine available. Method 1 was to compress the tube by an Instron 5982 with speed of 10 mm/min, shown in Figure 3.7(a); Method 2 was to pre-buckle the tube by a hydraulic machine (Figure 3.7(b)) to the point of plastic deformation, and then further compress it by the Instron machine with speed of 10 mm/min; and method 3 was to soften the specimen by annealing (heated to 1100°C and quenched in oil for austenitic steel), and then to compress it by Instron machine with speed of 10 mm/min. Annealed 304 stainless steel was tested with dog-bone samples and its stress-strain curve is given in Figure 3.8. In total, 13 specimens were prepared: 1 square tube, 3 O1 concave tubes, 3 O1 origami concave tubes, 3 O2 concave tubes, and 3 O2 origami concave tubes, all of which are shown in Figure 3.9. Short codes of those specimens and corresponding testing methods are listed in Table 3.2.

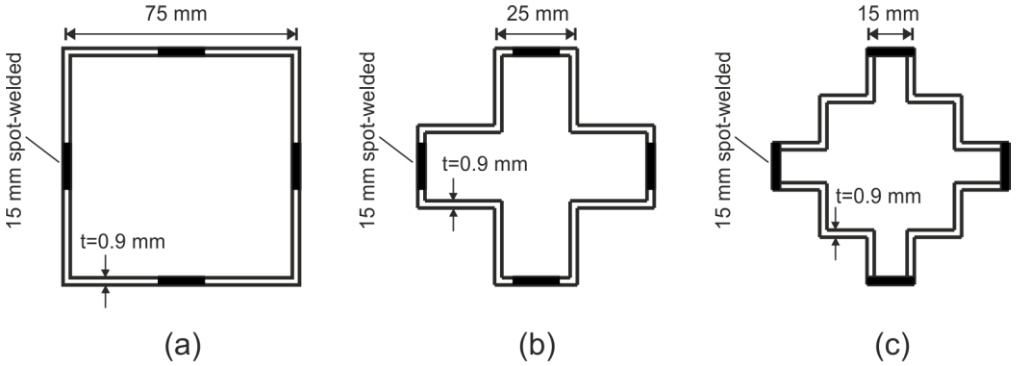

Figure 3.3. Dimensions of cross-section of tubes for experiment.

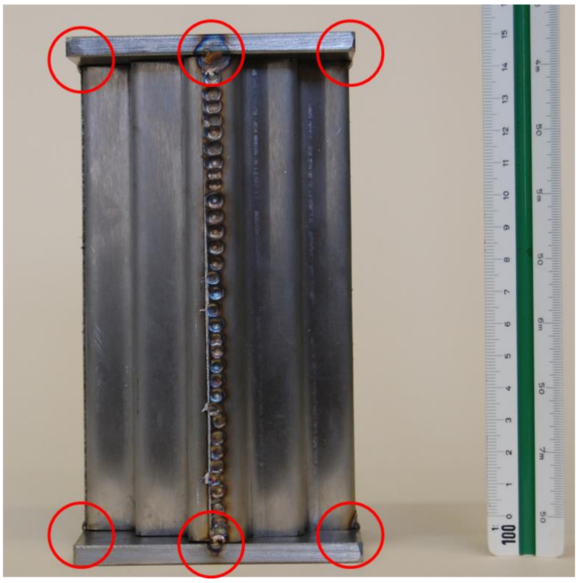

Figure 3.4. Tube welded to end plates.

Table 3.1: Parameters of origami concave tubes

Type	α (°)	l_1 (mm)	l_2 (mm)	w (mm)	t (mm)
O1 origami concave tube	80.66	142.5	7.6	25	0.9
O2 origami concave tube	80.66	142.5	7.6	15	0.9

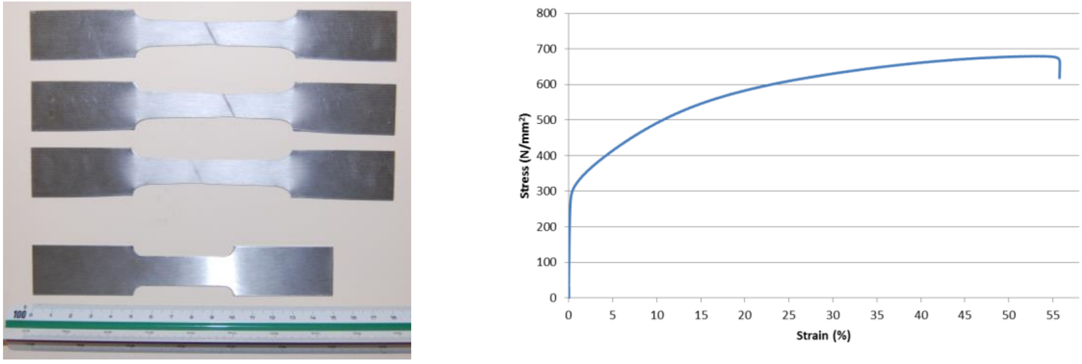

(a) (b)

Figure 3.5. Dog-bone specimen of 304 stainless steel and its stress-strain curve.

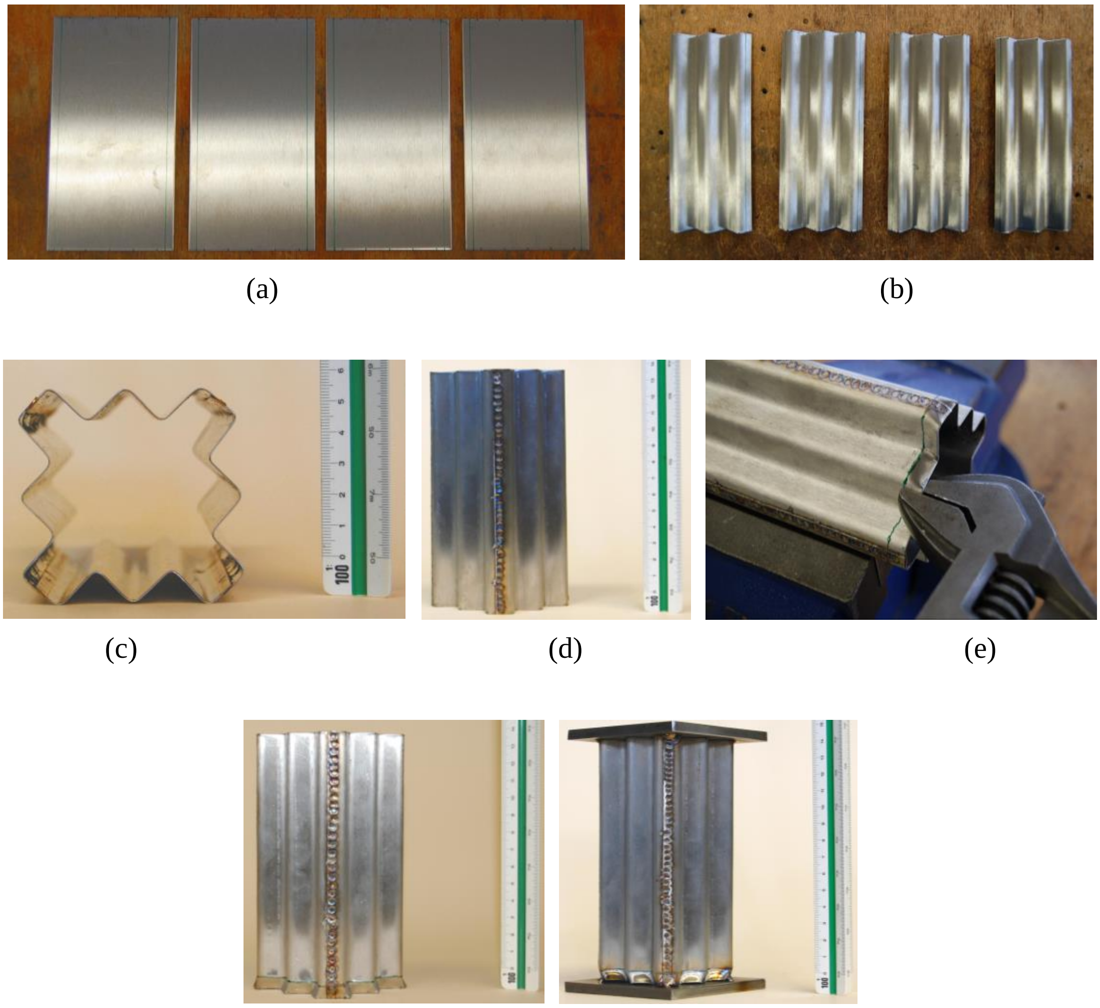

(a) (b)

(c) (d) (e)

(f) (g)

Figure 3.6. Manufacturing process of O2 origami concave tube: (a) cut four pieces of material; (b) bend them in to w-shape; (c) and (d) spot-weld four w-shape pieces together and form the tube; (e) bend one end of the tube to form the origami initiator by a spanner; (f) a O2 origami concave tube was made; (g) weld the tube into two steel plates.

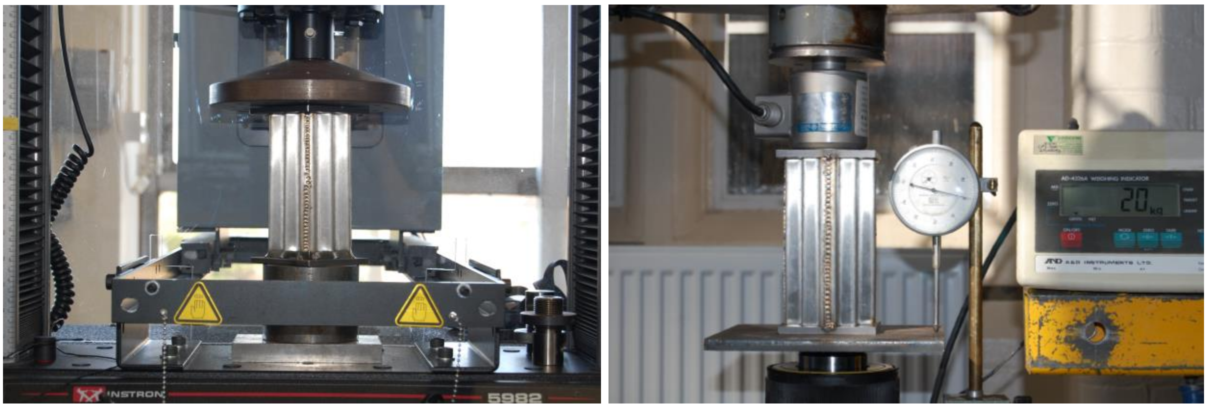

(a) (b)

Figure 3.7. Experiment settings: (a) Instron machine, and (b) hydraulic machine.

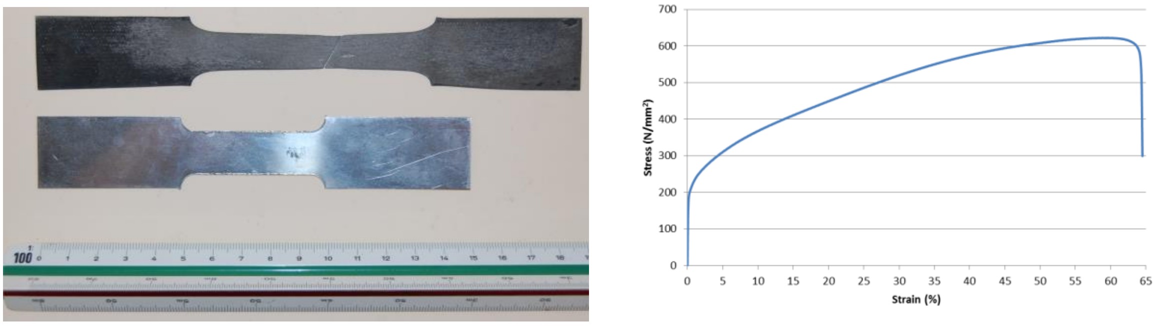

(a) (b)

Figure 3.8. (a) Tested dog bone specimen and (b) its stress strain curve of annealed 304 stainless steel.

(a) Square tube (b) O1 concave tube (c) O1 origami concave tube (d) O2 concave tube (e) O2 origami concave tube

Figure 3.9. Five types of tube for experiment: (a) square tube, (b) O1 concave tube, (c) O1 origami concave tube, (d) O2 concave tube, and (e) O2 origami concave tube.

Table 3.2: Name and testing method of each specimen.

Specimen	Short Code	Testing Method	Material
Square tube	S1	1	304 stainless
O1 concave tube 1	O1C1	2	304 stainless
O1 concave tube 2	O1C2	1	304 stainless
O1 concave tube 3	O1C3	1	304 stainless
O1 origami concave tube 1	O1OC1	1	304 stainless
O1 origami concave tube 2	O1OC2	1	304 stainless
O1 origami concave tube 3	O1OC3	1	304 stainless
O2 concave tube 1	O2C1	2	304 stainless
O2 concave tube 2	O2C2	2	304 stainless
O2 concave tube 3	O2C3	3	Annealed 304 stainless
O2 origami concave tube 1	O2OC1	1	304 stainless
O2 origami concave tube 2	O2OC2	1	304 stainless
O2 origami concave tube 3	O2OC3	1	304 stainless

3.2.2 Numerical Simulation Setup

Abaqus/Explicit (Abaqus, 2013) was used for the numerical simulation. Number and type of elements used in tubes are listed in Table 3.3. Shell elements were employed due to the thickness of the material is significantly smaller than the width, and S4R element (four-node shell element with reduced integration) was used due to its robustness. Tubes were tie constraint to two rigid plates at ends by four 15 mm length tabs, illustrated in Figure 3.10, which corresponded to the experimental setup. Each rigid plate used 1 R3D4 element. Imperfection amplitude of tubes was set as 0.1 mm for more realistic performance, and this amplitude was validated with experimental buckling forces in Section 3.3. First buckling mode was obtained from linear buckling analysis, shown in Figure 3.11(b), and it was superposed into perfect shape (Figure 3.11(a)) to form the imperfect shape (Figure 3.11(c)) (Ning, 2013). The superposition adds transversal displacement from the deformed shape to the perfect shape with adjusted amplitude. The intention of adding imperfection is to get the realistic buckling force in simulation, and the mode of imperfection doesn’t matter in this case. Rigid plate at the bottom was fixed, and the top one was controlled by a displacement which moved down to a total of 120 mm in 0.1 second, generating an axial compression on the tubes. No rotation of plates was allowed. Material was defined according to the result of dog-bone tests, and overlapping and hardening effect of welding region were not considered. Explicit Dynamics in Abaqus was used with consideration of geometric nonlinearity. General contact was applied, which considered self-contact. Friction was applied by using penalty with 0.25 friction coefficient. Convergence tests with respect to mesh density and analysis time were conducted prior to the analysis. These simulations can be regarded as quasi-static process since the kinematic energy was well below 5% of internal energy (Abaqus, 2013).

Table 3.3: Elements used for each numerical model.

Tube	Square	O1 concave	O1 origami concave	O2 concave	O2 origami concave
Elements	31248 S4R	45000 S4R	45602 S4R	71440 S4R	45300 S4R

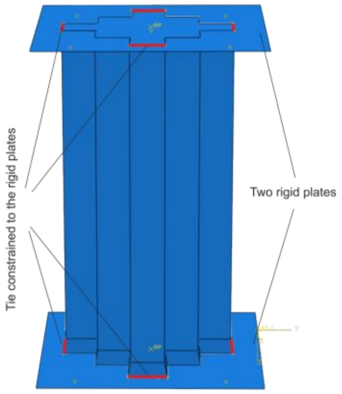

Figure 3.10. Setup of numerical simulation.

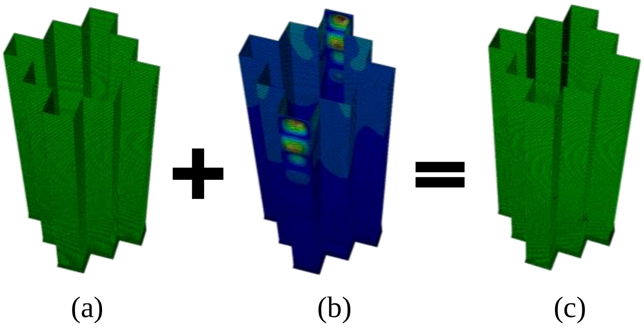
(a) (b) (c)

Figure 3.11. (a) Perfect shape, (b) critical buckling mode with 5 mm amplitude, and (c) imperfect shape with 0.1 mm amplitude obtained by superposing critical buckling mode onto the perfect shape.

3.3 Numerical and Experimental Results

Crushing of Square Tube

Experiments of 13 tubes and numerical simulation of 5 types of tubes were carried out. Deformation and reaction curves were collected and used for analysis and comparison. The reaction force was measured by recording the resistance that the top rigid plate experienced during crushing process, which equals to the external load applied to the structure. The square tube was used as a benchmark. Figure 3.12(a) and (b) show typical experimental and numerical failure mechanisms of square tube and indicates good consistency, in which the tube buckled and folded down into roughly three layers. Reaction-displacement plot of experiment and simulation is given in Figure 3.12(c). Initial peak force was generated and then dropped down after buckling. Several undulations of reaction force were observed corresponded to several periodic folds of the tube. In the end, reaction force rises when the tube was fully collapsed. Slight difference of experiment and simulation can be noticed in post-buckling reaction force.

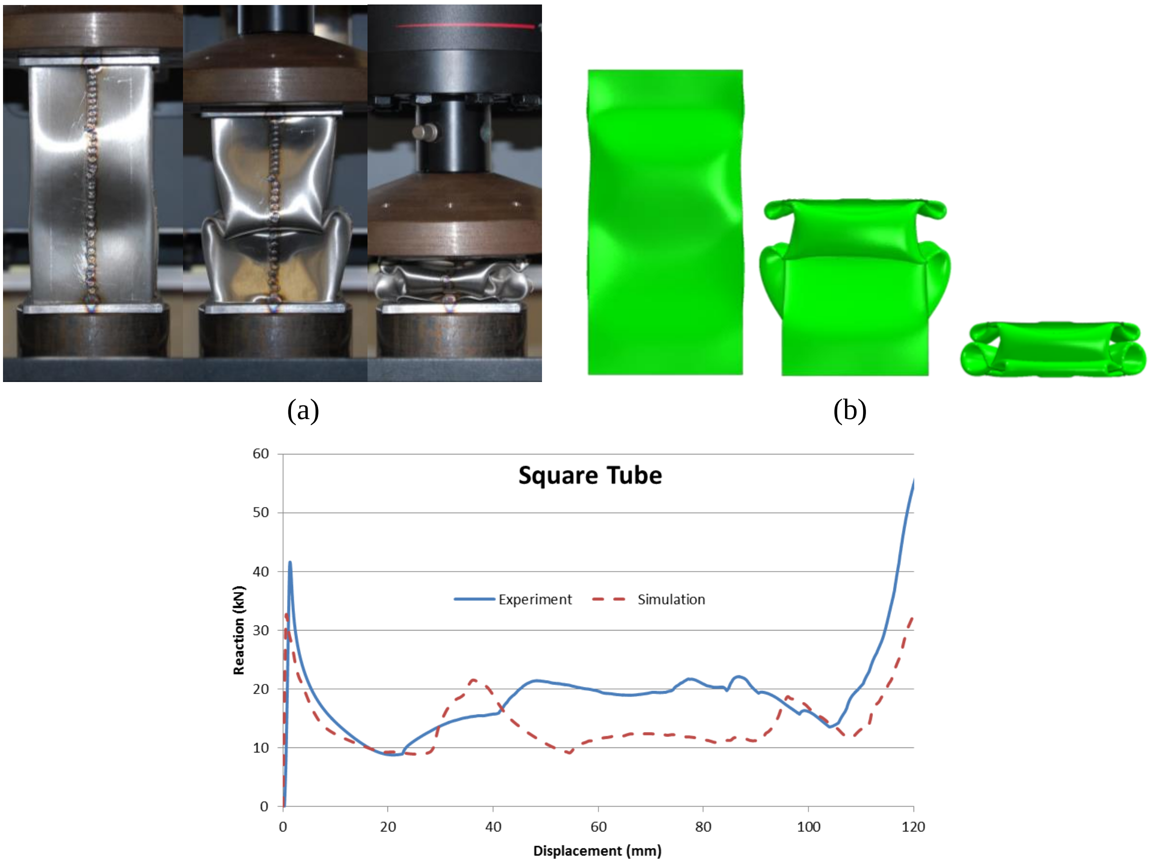

(a)

(b)

(c)

Figure 3.12. Crushing of square tube with displacements of 2.4 mm, 60 mm, and 120 mm in (a) experiment and (b) simulation, and (c) its reaction-displacement plot.

Crushing of O1 Concave Tubes

The experimental crushing of O1C1 and O1C2 are presented in Figure 3.13(a) and (b), and both of them swayed sideways and failed due to global instability, which was different from the progressive buckling mode demonstrated by square tube. The third sample of the same group, O1C3, managed to buckle progressively, shown in Figure 3.13(c). It matched the result of the numerical simulation of O1 concave tube (Figure 3.13(d)), and both demonstrated progressive buckling mode without capturing its instability problem. Lack of lateral constraint for the ends of tubes allowed the exposure of instability problem in the crushing of O1C1 and O1C2.

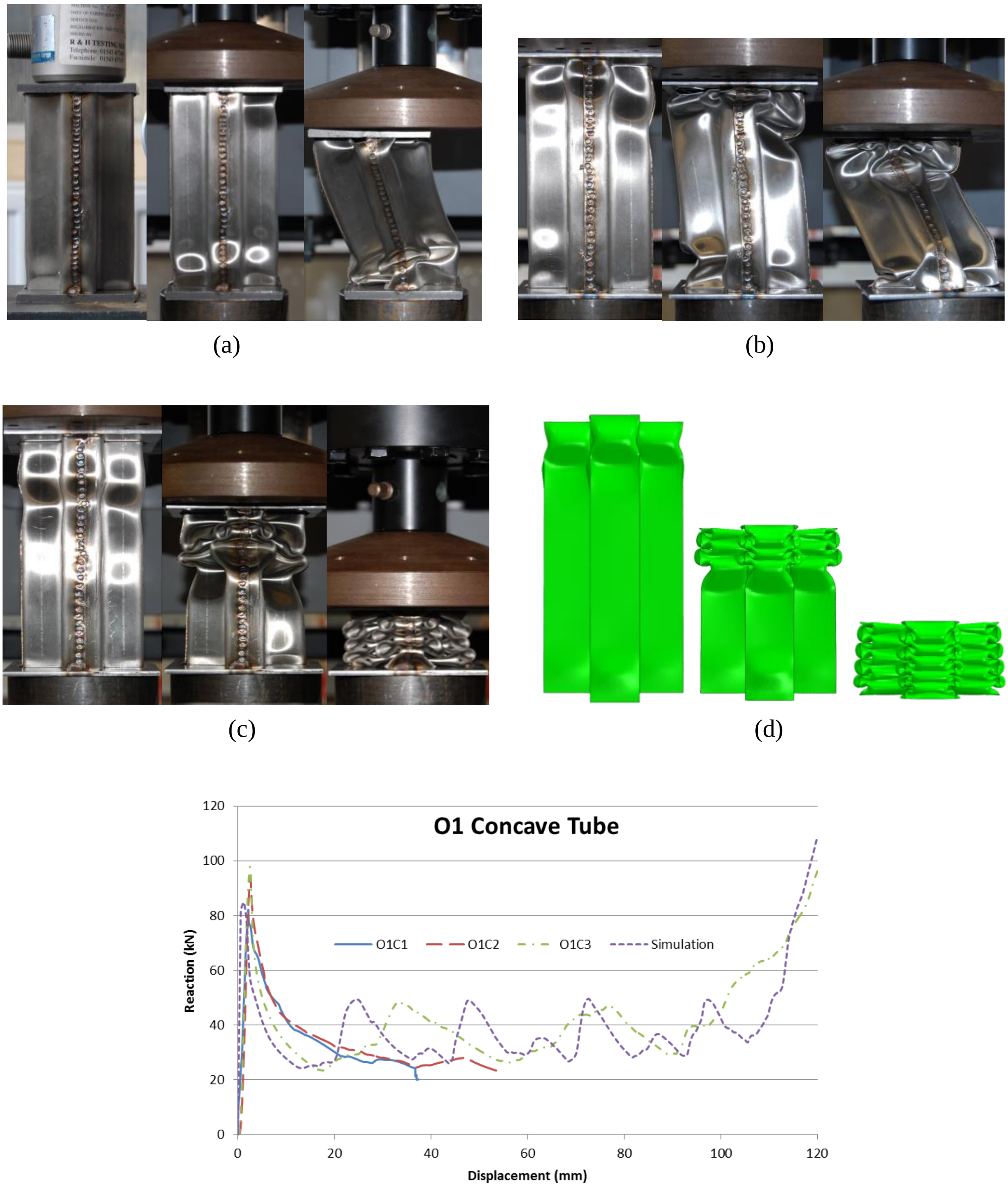

(a)

(b)

(c)

(d)

(e)

Figure 3.13. Experimental crushing of (a) O1C1 by hydraulic and Instron machine in sequence with displacements of 3 mm, 6.3mm, and 39.3 mm, (b) O1C2 by Instron machine with displacements of 3.3 mm 19.8 mm 52.8 mm, and (c) O1C3 and (d) numerical analysis of crushing O1 concave tube with displacements of 4.8 mm 60 mm 110.4 mm, and (e) corresponding reaction-displacement plot.

Reaction-displacement plot of three experiments (O1C1, O1C2, and O1C3) and simulation of O1 concave tube is presented in Figure 3.13(e). In this plot, the difference of reaction responses between different failure modes was obvious. O1C1 and O1C2 showed an identical response, while reaction force of O1C3 and numerical simulation were comparable to each other but significantly different from O1C1 and O1C2. Slight difference in initial slopes of reaction curves can be observed, which was due to small gap and compliance within the structure and the loading system.

Crushing of O1 Origami Concave Tubes

Compression of O1OC1 and numerical simulation of crushing O1 origami concave tube demonstrated comparable progressive buckling modes, shown in Figure 3.14(a) and (b). Crushing of O1OC2 and O1OC3 gave identical failure mechanism with O1OC1. Reaction-displacement plot of crushing O1OC1, O1OC2, and O1OC3, and numerical simulation of O1 origami concave tube is shown in Figure 3.14(c). Reaction curves of three experiments were the same. The undulations of curves were due to successive contact and formation of each layer of folds. Curves of experiments showed small shift and slightly lower initial slope compared to that of the simulation. This shift was probably because the overlapped and spot-welded parts in experimental samples were thicker and harder than the rest, and tubes folded by fewer layers in experiments than in simulation.

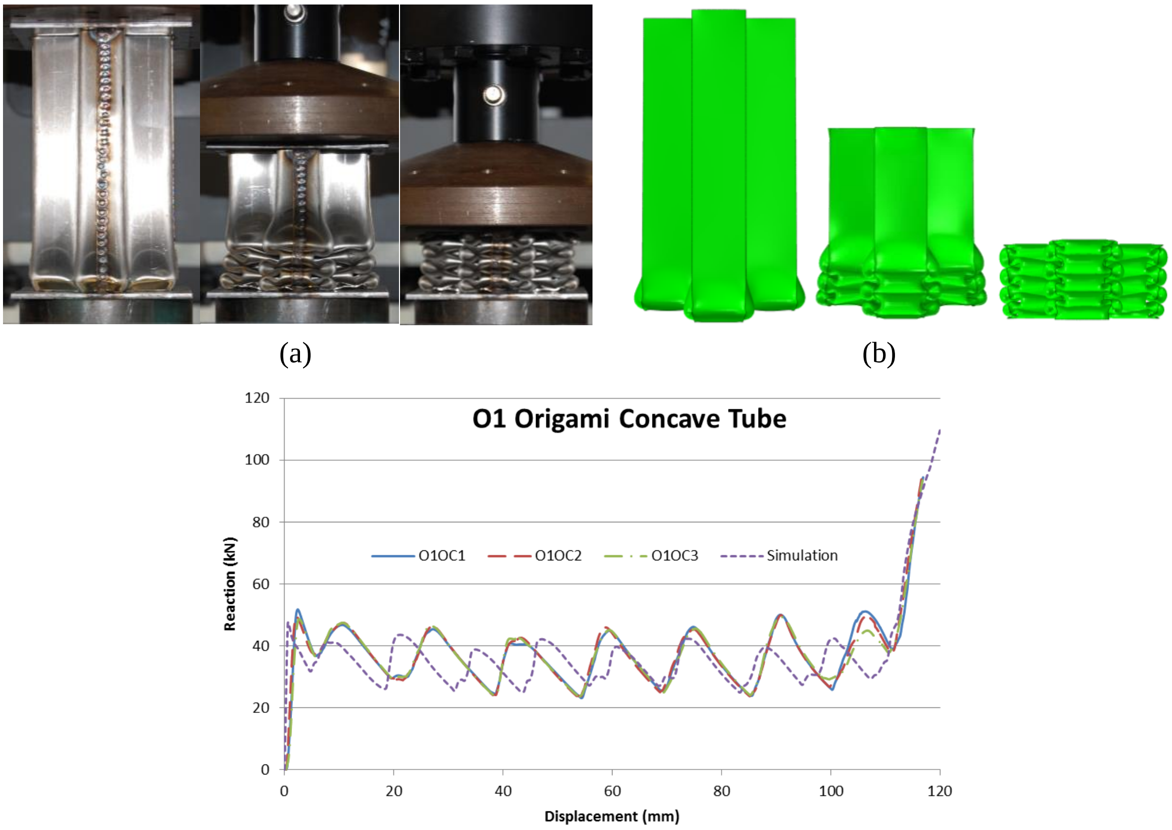

(a) (b)

(c)

Figure 3.14. (a) Experimental crushing of O1OC1 (O1OC2 and O1OC3 gave identical failure mechanism) with displacements of 6 mm, 60 mm, and 114 mm, (b) corresponding numerical simulation, and (c) their reaction-displacement plot.

Crushing of O2 Concave Tubes

Figure 3.15(a) and (b) present the failure mode of O2C1 and O2C2, and Figure 3.15(c) shows failure mechanism of O2 concave tube in numerical simulation. All of these deformations gave unstable failure modes. O2C1 and O2C2 swayed sideways when compressed and were identical to each other, while tube in numerical simulation bulged out in the middle. Reaction-displacement curves are provided in Figure 3.15(d), which shows that all three curves were comparable before deflected by 20 mm. When tubes were further compressed, reaction force in simulation surpassed that in experiments. This was due to the different deformation mode in simulation, which could provide additional resistance when the middle part of the tube got fully expanded circumferentially. The last deformation status shown in Figure 3.15(c) had the displacement of 20.5 mm, and this is corresponding to the point in Figure 3.15(d) where reaction force of experiments and simulation started to differ.

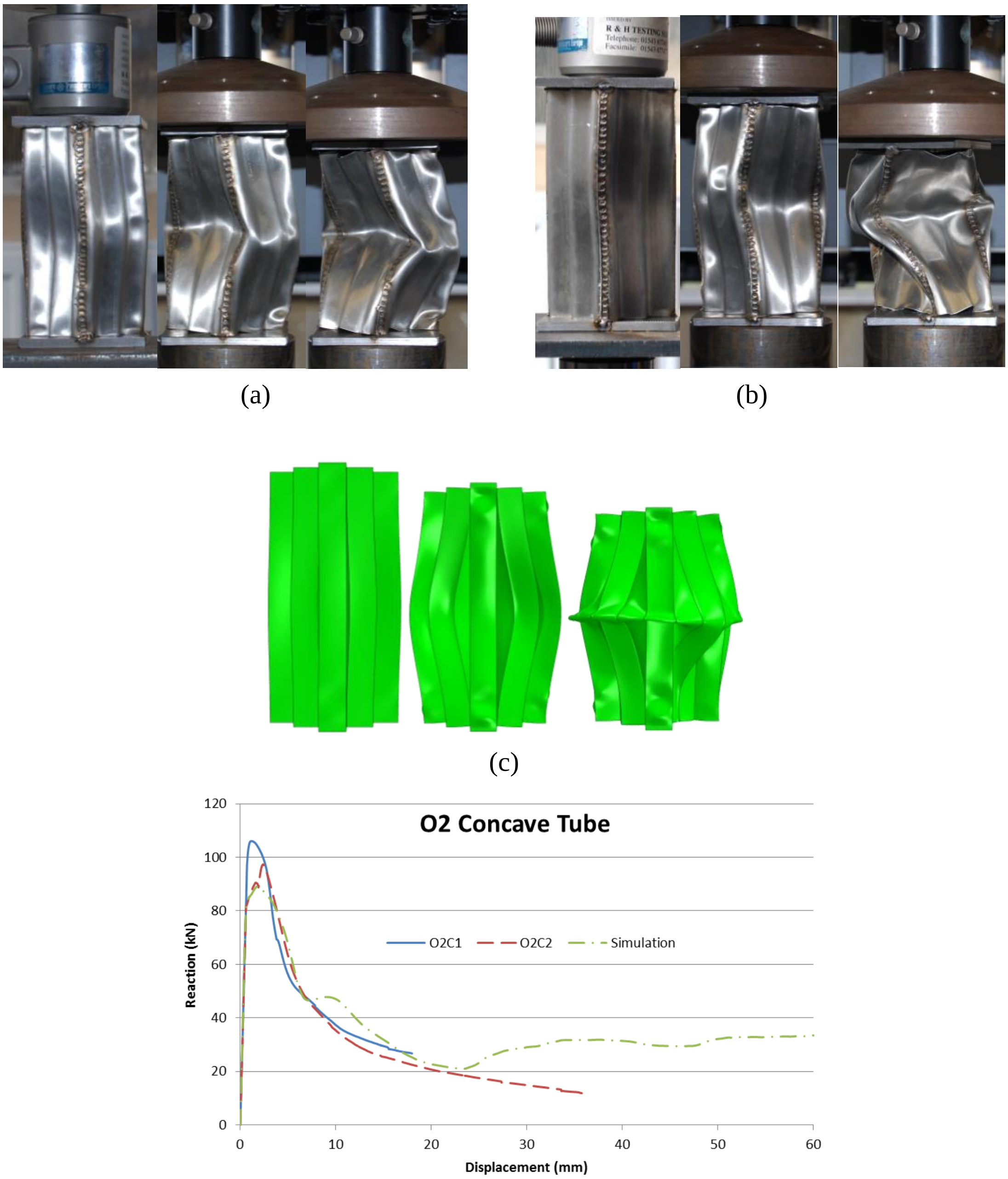

(a)

(b)

(c)

(d)

Figure 3.15. (a) Crushing of O2C1 by hydraulic and Instron machine in sequence with displacements of 4 mm, 10.4 mm, and 20.5 mm; (b) crushing of O2C2 by the same method with displacements of 3 mm, 10.4 mm, and 39.3 mm; (c) its numerical simulation with displacement of 2.4 mm 10.4 mm 20.5 mm; and (d) their reaction-displacement plot.

The failure mode of O2C3 is shown in Figure 3.16(a), and its corresponding numerical simulation is shown in Figure 3.16(b). Material property used in the simulation was the annealed 304 stainless steel. Both deformations gave unstable buckling and swaying-sideways failure mode. Reaction curves are shown in Figure 3.16(c), and O2C3 in the experiment had clearly higher buckling force than the result in numerical simulation. This could be caused by additional connection created between tube and plates in the annealing process (heated up to 1100°C), which could provide stronger boundary constraint and lead to higher buckling force. All O2 concave tubes' tests and simulations showed non-progressive buckling failure.

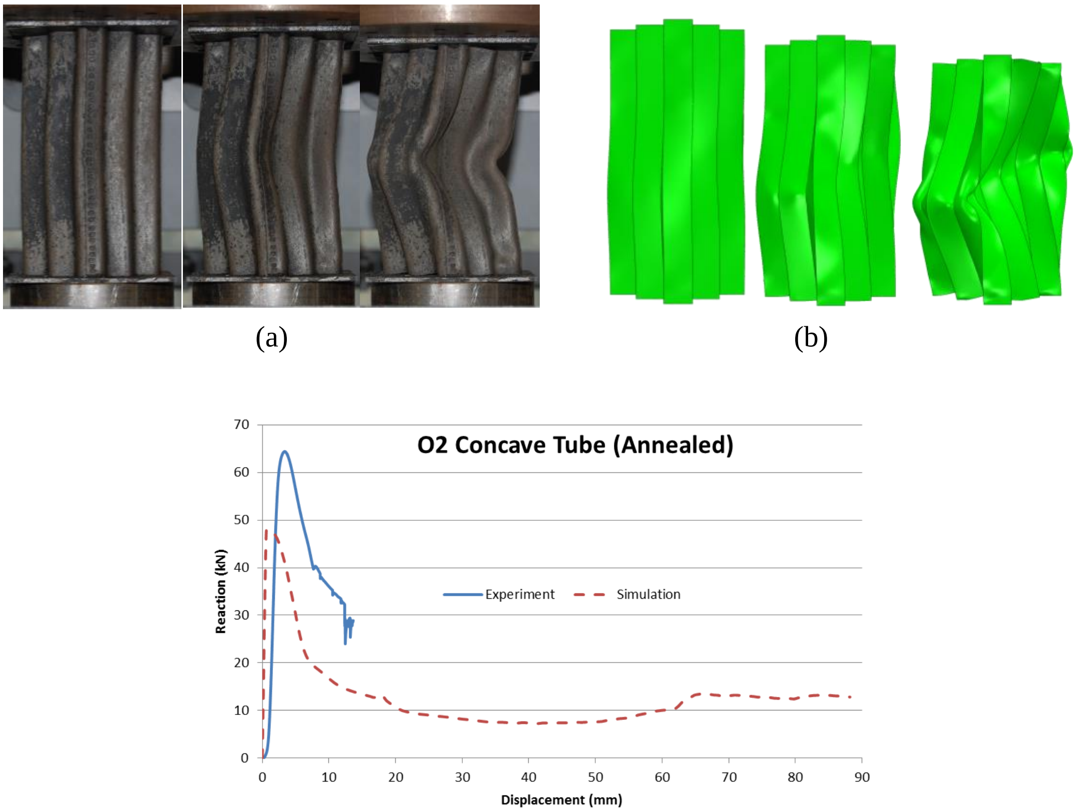

(a) (b)

(c)

Figure 3.16. (a) Crushing of O1C3 by Instron machine with displacements of 2.4 mm, 4.8 mm, and 14.4 mm, (b) its numerical analysis of crushing O2 concave tube (using annealed 304 stainless steel), and (c) their reaction-displacement curves.

Crushing of O2 Origami Concave Tubes

O2OC1, O2OC2, and O2OC3 were compressed in the Instron machine and gave identical progressive failure mode. Deformation of O2OC1 is presented in Figure 3.17(a). Numerical simulation of crushing O2 origami concave tube is given in Figure 3.17(b), and it is comparable to the experimental deformation. Reaction-displacement curves are shown in Figure 3.17(c). Similar to the crushing of O1 origami concave tubes, reaction curves of three experiments were the same, while they showed small shift and slightly lower initial slope compared to that of the simulation (Figure 3.17(c)).

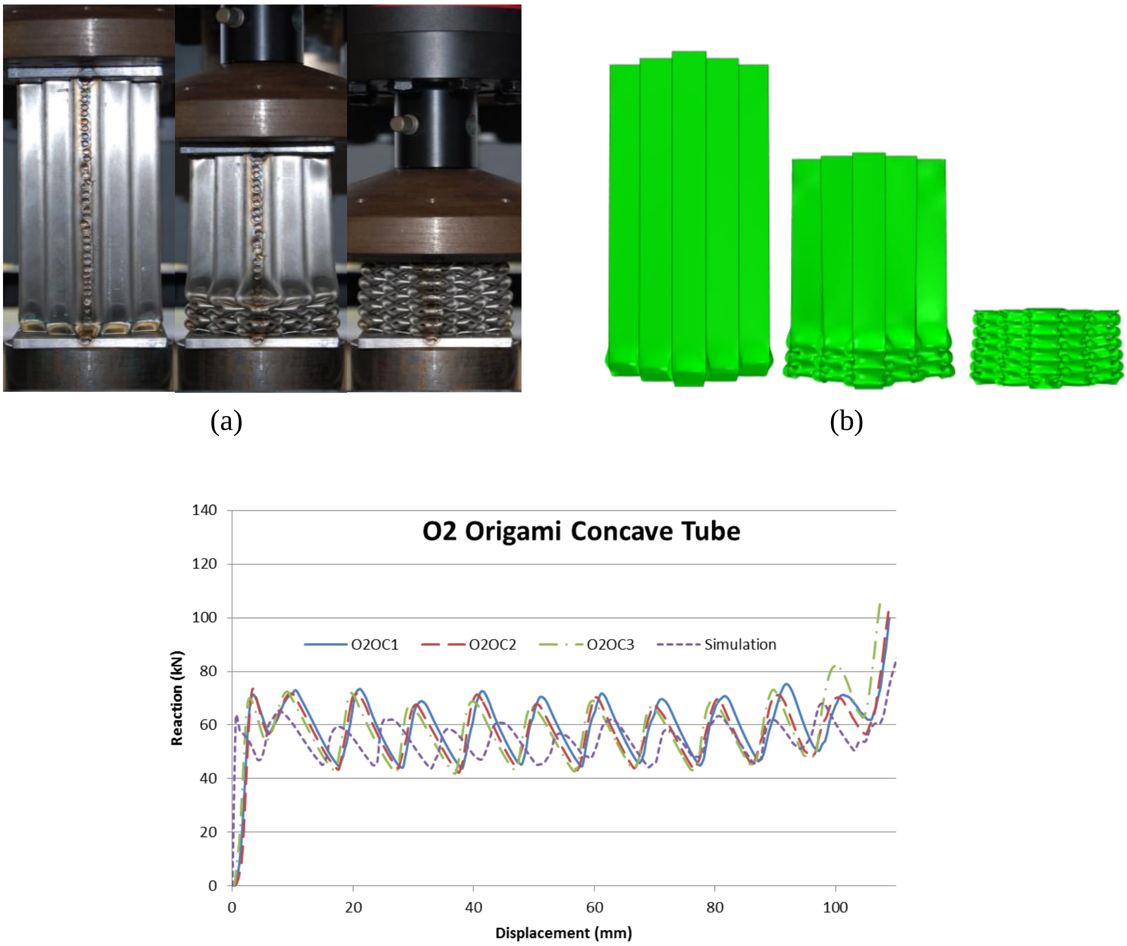

(a)

(b)

(c)

Figure 3.17. (a) Experimental crushing of O2OC1, (O2OC2 and O2OC3 gave identical failure mechanism to O2C1) with displacements of 2.4 mm, 43.2 mm, and 110.4 mm, (b) corresponding numerical analysis of crushing O2 origami concave tube, and (c) their reaction-displacement plot.

All crushed samples are presented in Figure 3.18. Origami concave tubes appeared to have more intriguing folds of material after crushed comparing to square and normal concave tubes. Globally unstable failure was dominating in the deformation of normal concave tubes.

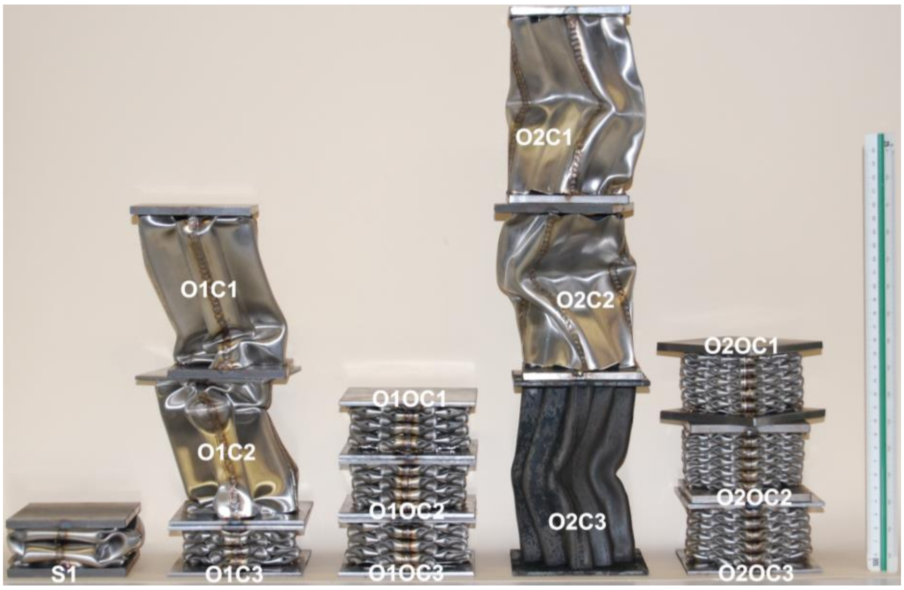

Figure 3.18. Crushed samples.

3.4 Discussion

The performance of square tube was as expected and set as a benchmark. The progressive failure occurred, and the tube folded down layer by layer. However, failure modes of normal concave tubes were rather inconsistent. O1C3 and simulation of O1 concave tube showed progressive buckling and the rest had non-progressive buckling. Comparison of simulation of O1 and O2 concave tubes indicated that concave tubes with longer relative-width (edge-width divided by thickness) are more likely to buckling progressively. However, even though O1 concave tubes (with parameters set in this section) had long relative-width for progressive buckling (as indicated in simulation), it was sensitive to asymmetry and tended to sway sideways when compressed. Further releasing of lateral constraints in simulation might capture this swaying performance in the experiment. For O2 concave tubes (with parameters set in this section), progressive buckling appeared to be impossible.

As a result, O1 and O2 concave tubes turn out to be unsuitable for energy absorbing applications (Lu and Yu, 2003b) for their high buckling force, non-progressive failure mode, and non-repeatable failure behaviour. One thing needs to be emphasised about O1 and O2 concave tubes is their ultra-high buckling forces. Their comparison with the square tube is shown in Table 3.4. The value in “Comparison” is defined as the peak force of concave tubes divided by that of square tube. From the table, buckling forces have been more than doubled by introducing concave cross-section, and this issue is further discussed in Section 3.6.4.

By introducing origami initiators, origami concave tubes can buckle progressively and utilise their multi-corners for high energy absorption. Figure 3.14 and Figure 3.17 show that origami initiator introduced geometric guidance to the structure, which led the tube to deform in a designed and geometrically compatible way. It is crucial to add folding to only one layer at one end of the tube, instead of throughout the tube which has only the zig-zag region and no straight region in the pattern, like what Ma and You (Ma and You, 2013b) did. When the tube gets crushed, origami initiator will deform first. While origami initiator is folding down, it automatically deforms the adjacent layer above it to form another layer of “initiator”. This layer will in turn form another one above it when it gets folded down afterward, and this process is just like how dominoes work. During this whole process, except for the layer which is folding down and its adjacent layer, the upper part of the tube remains straight and rigid. This mechanism brings an order to the crushing process, which allows the tube to deform one layer and pre-fold its adjacent layer at a time, instead of all at once to cause uncertain and unstable behaviour. Origami folding shall not be introduced throughout the tube, otherwise it will behave similarly to Figure 3.15 and Figure 3.16, and show non-progressive buckling modes.

Due to the undesirable performance of normal concave tubes for energy absorption, the focus is on the comparison of square tube and origami concave tubes, which is shown in Table 3.5. Inside the table, "Mean Crush Force Comparison" is defined as mean crush force of origami concave tubes divided by that of square tube. The direct plot of experimental reactions of origami concave and square tubes is shown in Figure 3.19. Origami concave tubes demonstrated that their mean crush forces were several times higher and also load uniformities were significantly lower than those of square tube. Stroke of origami concave tubes was slightly reduced due to the increase of folded layers during crushing process. This problem can be solved by introducing tapered shape and this improvement is presented in Section 6.2.1.

General consistency between experimental and numerical results was observed. Slight discrepancies in terms of deformation and reaction curves were mainly due to small manufacturing imperfection, the sensitive feature of samples, and machine's compliance, which were not technical mistakes and were practically tolerable. This indicates that further studies can rely on numerical analysis.

Table 3.4: Comparison of buckling forces between square tube and conventional concave tubes.

Type	Peak Force (kN)		Comparison	
	Exp.	FEA	Exp.	FEA
Square Tube	41.5	32.4	-	-
O1 concave tube	97.8	84.9	235.7%	262.0%
O2 concave tube	105.8	89.2	254.9%	275.3%

Table 3.5: Comparison of energy absorbing performance between square and origami concave tubes.

Type	Peak Force (kN)		Mean Crush Force (kN)		Stroke		Load Uniformity		Mean Crush Force Comparison	
	Exp. (avg.)	FEA	Exp. (avg.)	FEA	Exp. (avg.)	FEA	Exp. (avg.)	FEA	Exp. (avg.)	FEA
Square Tube	41.5	32.4	18.2	14.1	78.2%	80%	2.28	2.31	-	-
O1 origami tube	48.7	47.3	36.5	34.4	75.2%	74.8%	2.00	1.91	**200.5%**	**244.0%**
O2 origami tube	73.0	65.5	58.4	54.4	71.5%	72.4%	1.25	1.20	**320.9%**	**385.8%**

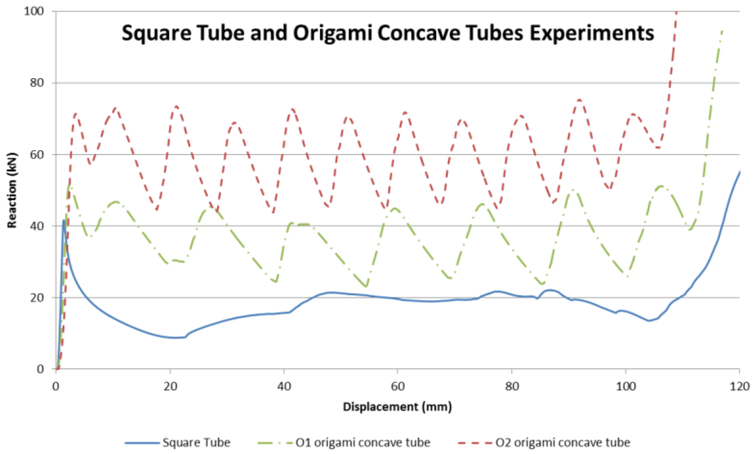

Figure 3.19. Plot of reaction forces of square and origami concave tubes in experiment.

3.5 Theoretical Modelling

In order to enable quick estimation of energy absorption of origami concave tubes to assist future design, theoretical modelling of origami concave tubes is introduced in this section.

Now let us consider the mechanism of a basic failure pattern. The idealised collapse mechanism is shown in Figure 3.20(a). This type of folding can be seen in the crushing of corners of square tube, which is also the folding mechanism for each corner of origami concave tubes. This sketch is one corner and a repetitively folded shape for the origami concave tube shown in Figure 3.20(b). Mean crush force P_m of square tube with symmetric buckling mode based on this element can be written as Equation (3) (Wierzbicki and Abramowicz, 1983), where σ_0 is the plastic flow stress of material, t is the wall thickness, and c is length of (AB + BC) in Figure 3.20(a). Considering that effective crushing length is about 70% of the total length of the tube (Abramowicz, 1983), P_m of a square tube can be rewritten as Equation (4). Its length h (noted in Figure 3.20(a)) for each layer can be expressed as (Wierzbicki and Abramowicz, 1983)

$$h = 0.983\sqrt[3]{tc^2}\ . \tag{8}$$

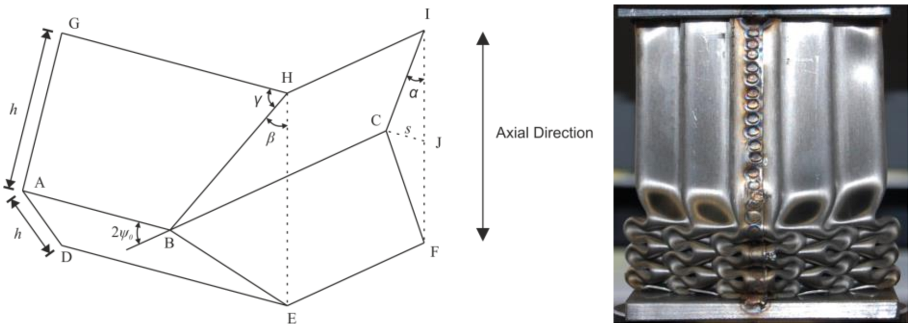

(a) (b)

Figure 3.20. Tube crushing mechanism. (a) Idealised collapse mechanism of one corner, and (b) collapse mode of O2 origami concave tube.

Buckling of origami concave tubes follows the same basic mechanism as square tube except for more repetitions. In consequence, mean crush forces of O1 and O2 origami concave tubes can be calculated by changing *c* in Equation (3) to *c*/3 and *c*/5 respectively, and then multiply 3 and 5 to the resultant equations respectively. The results can be expressed respectively as

$$P_{m1} = 28.42\sigma_0 t^{\frac{5}{3}} c^{\frac{1}{3}} \tag{9}$$

and

$$P_{m2} = 39.94\sigma_0 t^{\frac{5}{3}} c^{\frac{1}{3}}, \tag{10}$$

where *c* equals 3*w* and 5*w* for O1 and O2 origami tubes respectively and also equals to one-fourth of cross-sectional circumference. Their corresponding lengths which are noted as *h* in Figure 3.20(a) for each layer during crushing are

$$h_1 = 0.473\sqrt[3]{tc^2} \tag{11}$$

and

$$h_2 = 0.336\sqrt[3]{tc^2} \ . \tag{12}$$

Equivalent plastic flow stress σ_0 can be calculated by (Ma and You, 2013b)

$$\sigma_0 = \sqrt{\frac{\sigma_y \sigma_u}{1+n_s}} \ , \tag{13}$$

where n_s is the strain hardening exponent which equals to 0.43 for 304 stainless steel. This formula simplifies the plastic strain curve into an averaged constant value σ_0., which avoids the consideration of non-linearity of the material in modelling.

Equation (4), (9) and (10) give an estimation of mean crush force for the square, O1 and O2 origami concave tubes respectively. Putting parameters of tubes which were tested and simulated in Section 3.2 into those models, they give the mean crush forces of the square, O1 origami, and O2 origami tubes as 16.3 kN, 33.9 kN, and 47.7 kN respectively. Equation (8), (11), and (12) give us the number of folds of those tubes which are 4.44, 9.25, and 12.99 for the square, O1 origami, and O2 origami tubes respectively. The numbers produced from equations are not integers, while only integers are possible in practice due to compatibility. In consequence, the estimated numbers of folds shall be rounded to 4, 9, 13 respectively. Comparison of theoretical with experimental and numerical results is shown in Table 3.6, and theoretical values are in good consistency with them. Comparing to numerical results, theoretical value overestimates its mean crush force for the square tube and underestimates it for O2 origami tube. One of the reasons can be the theoretical model assumes 70% stroke for all situations. However, smaller w/t value leads to more folded layers which might cause smaller stroke instead of constantly 70%. Models with a more realistic estimation of effective crushing distance need to be developed in the future. A series of numerical simulations have been run with different wall thicknesses of origami concave tubes, and their comparison with results of Equation (9) and (10) is shown in Figure 3.21. The theoretical model matches the numerical results well when *t* is smaller, while slightly underestimates mean crush force when *t* gets larger.

These simple theoretical models can give a quick and conservative estimation of energy absorbing capacity of origami concave tubes, which shall be very useful for preliminary design. Equation (9) and (10) suggest the mean crushing forces of O1 and O2 origami concave tubes are respectively 2.1 and 2.9 times of that of the square tube (Equation (4)). Simple geometric optimization can be done by dividing Equation (9) or (10) by $t \cdot c$ which is an expression of cross-sectional area. This will give us its ratio (after neglecting constants) as

$$\frac{P_m}{m} = s \cdot \left(\frac{t}{c}\right)^{\frac{2}{3}}, \tag{14}$$

where *m* is the mass of the tube and *s* is a constant. Equation (14) suggests relatively thicker material (higher *t*/*c* ratio) can increase energy absorption per unit weight (higher P_m/m ratio). However, this conclusion might not hold if tubes buckle in different ways, and this issue is further discussed in Section 3.6.

Table 3.6: Comparison of theoretical results to experimental and numerical results.

Type	Mean Crush Force				Number of Folds			
	Exp. (kN)	FEA (kN)	Theoretical (kN)	Theoretical to FEA Difference	Exp.	FEA	Theoretical	Theoretical to FEA Difference
Square Tube	18.2	14.1	16.3	15.6%	3	4	4.44	11.1%
O1 origami tube	36.5	34.4	33.9	-1.5%	7	9	9.25	2.70%
O2 origami tube	58.4	54.4	47.7	-12.3%	10	12	12.99	8.27%

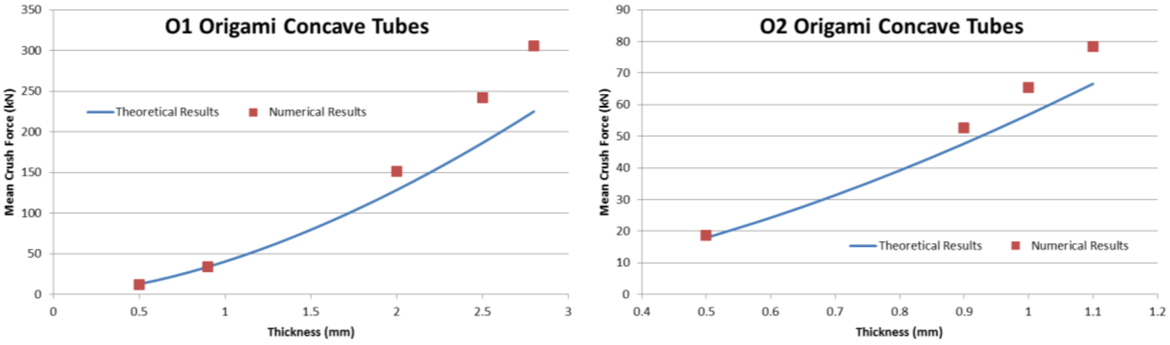

(a) (b)

Figure 3.21. Plots of comparison between theoretical and numerical results of (a) O1 and (b) O2 origami concave tubes.

3.6 Parametric Study

Progressive buckling of origami concave tubes provides good energy absorbing ability. However, non-progressive buckling (such as in Figure 3.15) can occur for origami concave tubes if the parameters are not appropriate. In consequence, it is essential to guarantee progressive failure mode instead of non-progressive. The purpose of parametric study in this section is to find out an appropriate range of those parameters that can guarantee progressive buckling of origami concave tubes. Our study relies on numerical analysis which has the same setting in terms of mesh density, material and so on to Section 3.3.

3.6.1 Effect of *w*/*t* Ratio and Tube Length *l*

The successful crushing of origami concave tubes requires the buckling force of concave tube (without origami initiator) to be sufficiently larger than the reaction force needed for the progressive failure of its origami version. Buckling force of O1 and O2 concave tube shall be proportional to $t^2\left(\frac{w}{t}\right)^{m_1}$ (Timoshenko, 1961), and the reaction force needed for origami concave tubes shall be proportional to $t^2\left(\frac{w}{t}\right)^{m_2}$ as indicated in Section 3.5, where m_1 and m_2 are corresponding exponents. Division of these two expressions indicates that w/t is the key value which affects the failure mechanism. With this understanding, a series of numerical simulations with different w/t ratio of O1 and O2 origami concave tubes were run to find out the working range, and results are shown in Table 3.7 and Table 3.8. Inside the tables, the differential ratio is defined as buckling load of the concave tube divided by the peak reaction force of origami concave tube. Failure modes are categorised as progressive, mixed, and non-progressive. These two tables show that relatively thicker origami tubes can again suffer non-progressive buckling. Geometries of tubes are same with Table 3.1 except for thickness. Settings of numerical simulations are same with Section 3.2 except for fully clamped boundary condition, which matches better with the practical installation. Failure modes of O1 origami concave tubes with w/t ratio of 8.93, 8.33, and 7.81 are shown in Figure 3.22. Failure modes of O2 origami concave tubes with w/t ratio of 13.64, 11.54, and 10.71 are shown in Figure 3.23. From these figures, they show that failure modes changed from progressive to non-progressive when w/t ratio getting smaller. Change of peak forces of tubes and differential ratio to w/t has been plotted in Figure 3.24. It shows that thinner tubes have a larger differential ratio between peak force of concave tube and corresponding origami concave tube, i.e., more likely to achieve progressive buckling modes. Switching points of O1 and O2 origami concave tubes from progressive to non-progressive are $w/t = 8.93$ and 13.65 respectively. For conservation, working zone of w/t has been chosen as $w/t > 10$ for O1 origami tubes, and $w/t > 15$ for O2 origami tubes.

Table 3.7: Parametric study of *w*/*t* ratio of O1 origami concave tube.

w/*t* ratio	Buckling load of concave tube	Peak reaction force of origami concave tube	Differential ratio	Failure mode
25/0.5 = 50	39.9	17.5	2.29	Progressive
25/0.9 = 27.78	90.1	47.3	1.91	Progressive
25/2 = 12.5	260.6	198.3	1.31	Progressive
25/2.5 = 10	348.2	283.9	1.23	Progressive
25/2.8 = 8.93	401.3	357.2	1.12	Progressive
25/3 = 8.33	437.3	401.0	1.09	Mixed
25/3.2 = 7.81	473.8	443.2	1.07	Non-progressive

Table 3.8: Parametric study of *w*/*t* ratio of O2 origami concave tube.

w/*t* ratio	Buckling load of concave tube	Peak reaction force of origami concave tube	Differential ratio	Failure mode
15/0.5 = 30	45.3	26.8	1.69	Progressive
15/0.9 = 16.67	89.5	69.0	1.30	Progressive
15/1 = 15	99.7	82.7	1.21	Progressive
15/1.1 = 13.64	109.9	95.3	1.15	Progressive
15/1.2 = 12.5	120.9	108.8	1.13	Mixed
15/1.3 = 11.54	141.2	123.8	1.14	Mixed
15/1.4 = 10.71	153.4	140.0	1.10	Non-progressive

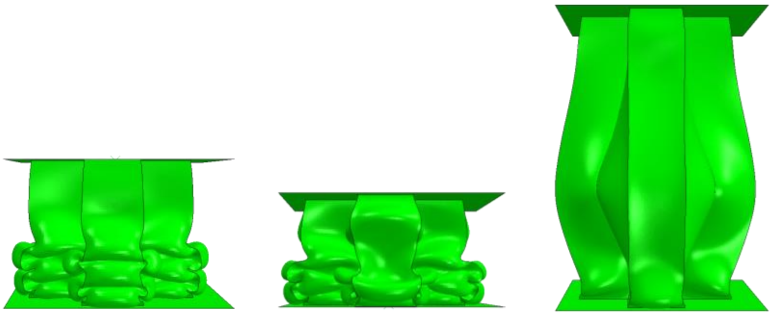

(a) (b) (c)

Figure 3.22. Deformation of crushing of O1 origami concave tubes with *w*/*t* ratio of (a) 8.93, (b) 8.33, and (c) 7.81.

(a) (b) (c)

Figure 3.23. Crushing of O2 origami concave tubes with *w*/*t* ratio of (a) 13.64, (b) 11.54, and (c) 10.71.

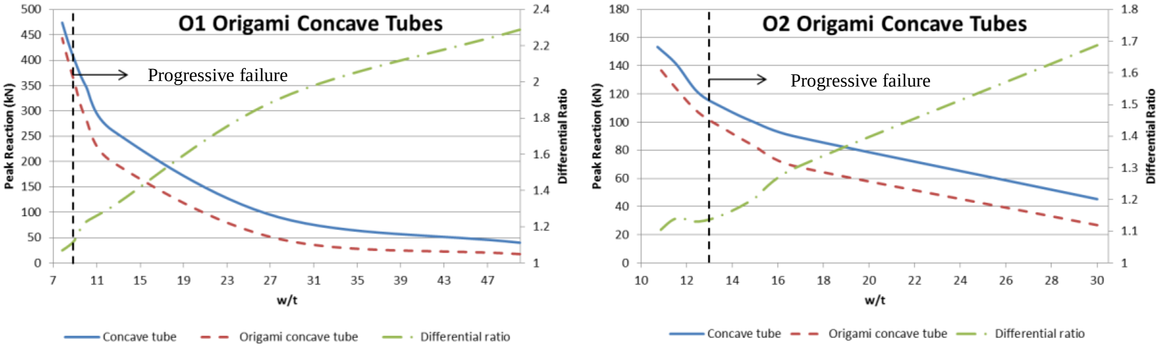

(a) (b)

Figure 3.24. Change of peak forces and differential ratio with change of *w*/*t* for (a) O1 and (b) O2 origami concave tubes.

The increase of *l*, which is the total length of the tube, will also increase of possible instable behaviour of origami concave tubes. Numerical analysis has been done for O1 and O2 origami tubes with different values of *l*, and the results are shown in Table 3.9 and Table 3.10 respectively. They show that O1 origami concave tubes had progressive failure even with *l* = 350 mm, and O2 origami concave tubes could maintain progressive deformation with *l* smaller than 180 mm. Deformations of crushing O1 origami concave tube (*l* = 350mm) and O2 origami concave tubes (*l* = 180 and 200 mm) are shown in Figure 3.25. O1 origami concave tubes demonstrated progressive failure all along. When *l* increased to 200 mm, the material of O2 origami concave tube bulged out. In consequence, it is conservatively recommended that *l*/*w* shall be smaller than 12 for both O1 and O2 origami concave tubes.

Table 3.9: Parametric study of *l*/*w* ratio of O1 origami concave tubes.

l/*w*	150/25=6	250/25=10	300/25=12	350/25=14
O1 origami concave tube	Progressive	Progressive	Progressive	Progressive

Table 3.10: Parametric study of *l*/*w* ratio of O2 origami concave tubes.

l/*w*	150/15=10	180/15=12	200/15=13.3
O2 origami concave tube	Progressive	Progressive	Non-progressive

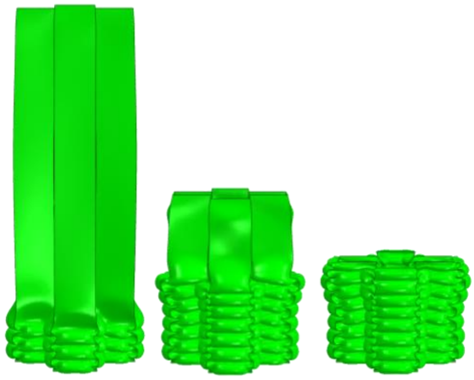

(a) Length is 350 mm, and displacements are 120 mm, 240 mm, and 285 mm respectively

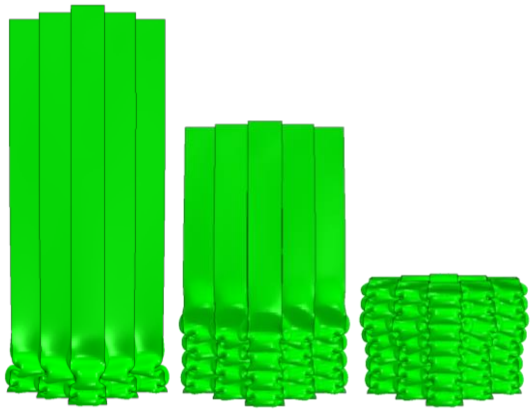

(b) Length is 180 mm, and displacements are 30 mm, 75 mm, and 132 mm respectively

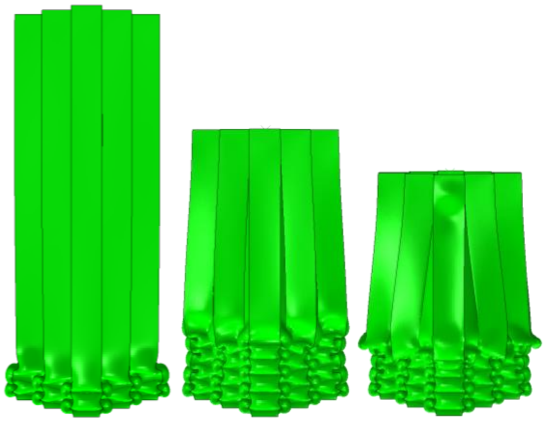

(c) Length is 200 mm, and displacements are 34 mm, 85 mm, and 102 mm respectively

Figure 3.25. Deformations of O1 and O2 origami concave tubes with different tube lengths.

3.6.2 **Design of Origami Initiator**

The geometry of origami initiator is controlled by two parameters α and l_2, shown in Figure 3.2. l_2 was initially set as 7.6 mm, and α was altered to 60° and 85°, and all tubes showed progressive failure mechanism, which are listed in Table 3.11. In order to find out the limit of l_2, α was set as 85°, and l_2 was altered from $h/2$ to $2h$ (h can be calculated from Equation (11) and (12)). It was found out that conservative range of l_2 is from $2/3h$ to $2h$, shown in Table 3.12. Non-progressive failure modes of O1 and O2 origami concave tubes with l_2 of 5 mm and 3 mm respectively are shown in Figure 3.26.

Table 3.11: Parametric study of inclined angle.

α (°)	O1 origami concave tube	O2 origami concave tube
60	Progressive	Progressive
85	Progressive	Progressive

Table 3.12: Parametric study of length of the initiator.

l_2 (mm)	O1 origami concave tube	l_2 (mm)	O2 origami concave tube
$h_1/2=5$	Non-progressive	$h_2/2=3$	Non-progressive
$2/3h_1=7.6$	Progressive	$2/3h_2=6$	Progressive
$2h_1=23$	Progressive	$2h_2=12$	Progressive

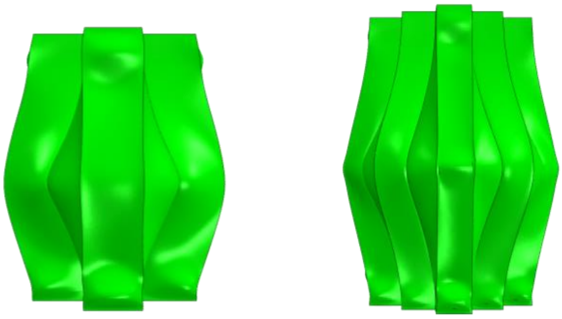

(a) Displacement is 24 mm (b) Displacement is 12 mm

Figure 3.26. Deformation of (a) O1 and (b) O2 origami concave tubes.

3.6.3 **Imperfection and Boundary Condition Sensitivity**

Thinner tubes (with larger w/t ratio) are more sensitive to geometric imperfection (Jones, 2006). It was chosen to add imperfection with an amplitude of 0.5 mm to tubes with same geometry shown in Table 3.1, except for 0.5 mm wall thickness, shown in Figure 3.27. Both of them gave stable progressive failure and demonstrated their low imperfection sensitivity, shown in Figure 3.28. Strong imperfection is not considered in this research.

In order to see the effect of different practical boundary conditions, tubes were partially clamped as shown in Figure 3.10, and other tubes were fully clamped at two ends. Geometries of them were the same with Table 3.1. They showed identical deformation, and the comparison of their reaction forces is in Figure 3.29. It shows the change of boundary condition does not change the performance of tubes except for slightly shifting the phase of reaction curve.

In conclusion, origami concave tubes are not sensitive to practical imperfection and boundary conditions.

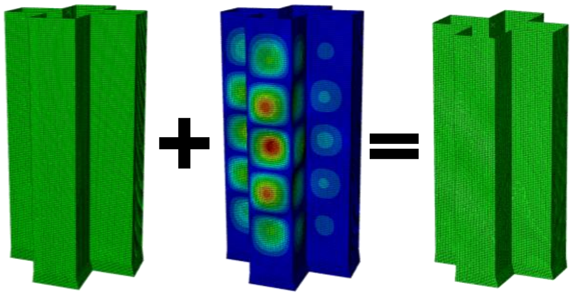

(a) O1 origami concave tube with perfect shape, critical buckling mode with 5 mm amplitude (for clarification), and imperfect shape with 0.5 mm amplitude (which cannot be seen obviously from the figure) obtained by superposing imperfection onto perfect shape.

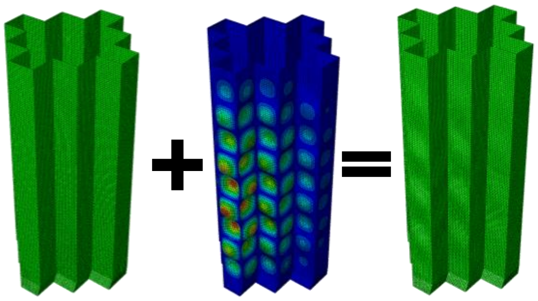

(b) O2 origami concave tube with perfect shape, critical buckling mode with 5 mm amplitude (for clarification), and imperfect shape with 0.5 mm amplitude (which cannot be seen obviously from the figure) obtained by superposing imperfection onto perfect shape.

Figure 3.27. Transferring from perfect shapes to imperfect shapes.

(a) (b)

Figure 3.28. Deformation of crushing imperfect (a) O1 origami concave tube and (b) O2 origami concave tube.

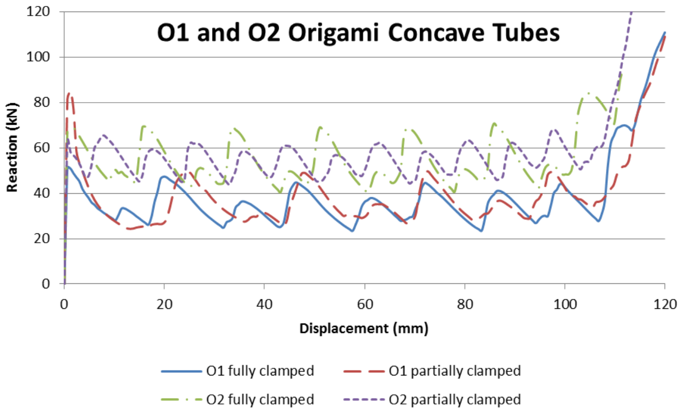

Figure 3.29. Reaction to displacement plot of O1 and O2 origami concave tubes with different boundary conditions.

3.6.4 **Summary on Design Parameters**

After running a series of simulations with different parameters, the valid range of those parameters have been worked out, which is shown in Table 3.13. This can conservatively guarantee stable progressive failure mechanism of origami concave tubes. The performance of origami concave tubes is not sensitive to practical geometric imperfection and boundary conditions. Within the range of Table 3.13, smaller w/t ratio shall give higher energy absorption per unit weight (Section 3.5).

Table 3.13: Prefered range of parameters

Types	w/t	l/w	α (°)	l_2
O1 origami concave tube	≥10	≤12	60 ~ 85	2/3 h_1~2 h_1
O2 origami concave tube	≥15	≤12	60 ~ 85	2/3 h_2~2 h_2

Table 3.7 and Table 3.8 show when *w*/*t* turns small, the load required for progressive buckling of origami concave tube is getting close to the peak buckling load of its corresponding concave tube. Buckling force of concave tubes with relatively short width is highest among different cross sections (in Table 3.4) (Fan et al., 2013, Ning and Pellegrino, 2013). In another word, concave tubes are among tubes with the largest reaction force. In consequence, because of low load uniformity (shown in Table 3.5), origami concave tubes are absorbing energy with reaction force that is close to the buckling force of concave tubes. That is to say, origami concave tubes are among the most efficient energy absorbers in theory.

3.7 Dynamic and Inclined Loading

This section aims to figure out the effect of dynamic and inclined loading. Dynamic loading was considered by increasing the speed of compressing rigid body to 30m/s. For inclined loads, displacements with angles of 5° and 10° have been applied respectively for assessing the performance of tubes. Tubes with parameters listed in Table 3.14 were chosen for simulation. Those parameters are close to the limits suggested in Table 3.13, which shall give tubes most unstable performance and sensitivity to dynamic and inclined loading effects. Clamped boundary condition was applied.

Table 3.14: Parameters chosen for simulation.

Types	w/t	l (mm)	α (°)	l_2
O1 origami concave tube	10	150	85	2/3 h_1
O2 origami concave tube	15	150	85	2/3 h_2

3.7.1 **Dynamic Loading**

Settings of simulation were same with Section 3.6.1, except for the speed of displacement changed to 30m/s (120 mm in 0.004s). Comparison of static and dynamic cases in terms of the reaction force is shown in Figure 3.30. It shows that there were stress waves transmitting through structures and generated more fluctuation in the reaction force. Failure mechanisms were identical between static and dynamic cases, and the ratio of kinematic to internal energy was still well below 5%. From these, it is concluded that dynamic loading (with middle speed) has no obvious effect on failure mechanism and only slight change of reaction force.

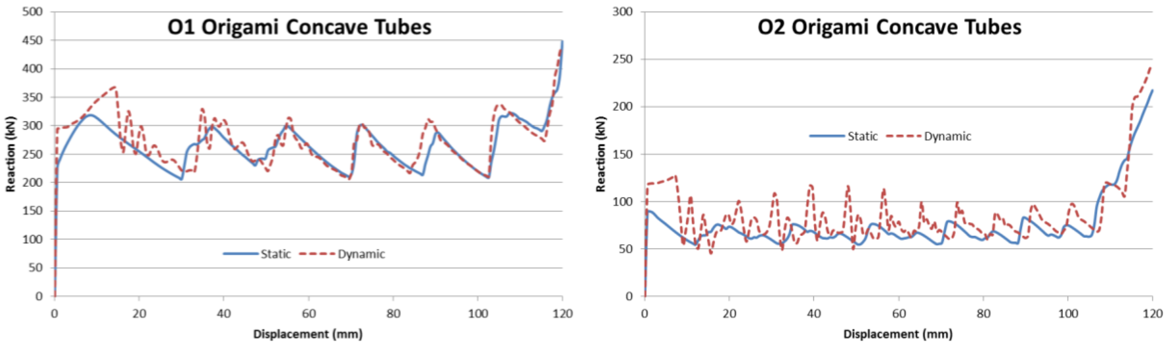

(a) (b)

Figure 3.30. Reaction to displacement plots of static and dynamic loading of (a) O1 and (b) O2 origami concave tubes.

3.7.2 **Inclined Loading**

Two directions of inclination were defined and named as direction 1 and 2, shown in Figure 3.31. Deformations are shown in Figure 3.32, and plots are shown in Figure 3.33. Reaction curves only took account vertical reaction forces. For 5° inclination, both origami concave tubes performed almost identical to vertical loading in terms of both failure mechanisms and reaction forces. For 10° inclination, failure mechanisms and reaction forces of origami concave tubes altered slightly, but their energy absorbing abilities (reaction forces) remained unchanged. From Figure 3.33(b), it can be noticed that inclination of loading could increase the stroke of O2 origami concave tube. This was due to the accommodation of material horizontally during crushing process instead of only piling up vertically, as shown in Figure 3.32. In conclusion, origami concave tubes can function effectively with inclined loadings (at least within 10° inclination).

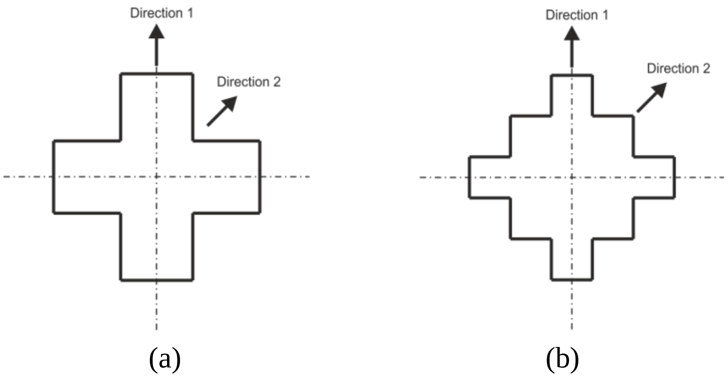

(a) (b)

Figure 3.31. Defining direction 1 and 2 for (a) O1 and (b) O2 origami concave tubes.

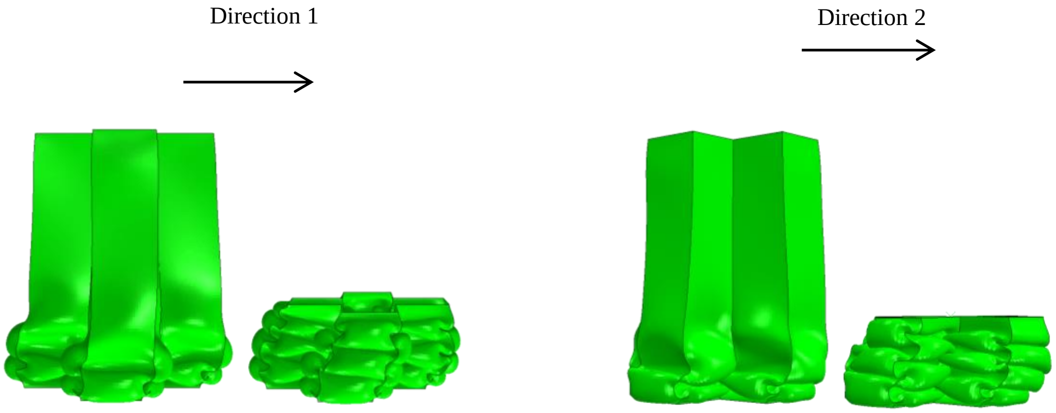

(a) O1 origami tube with 5° inclined loading (in direction 1).

(b) O1 origami tube with 5° inclined loading (in direction 2).

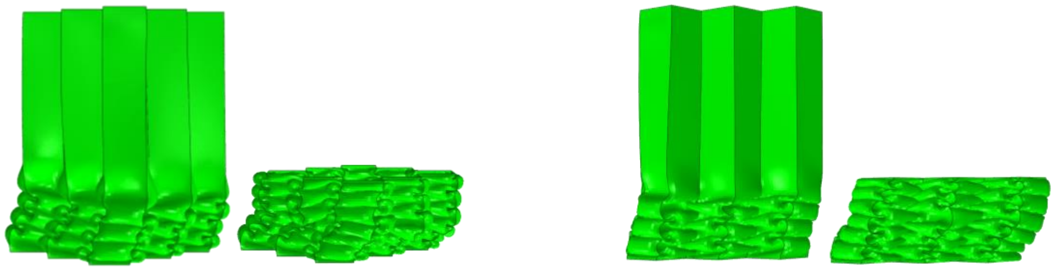

(c) O2 origami tube with 5° inclined loading (in direction 1).

(d) O2 origami tube with 5° inclined loading (in direction 2).

(e) O1 origami tube with 10° inclined loading (in direction 1).

(f) O1 origami tube with 10° inclined loading (in direction 2).

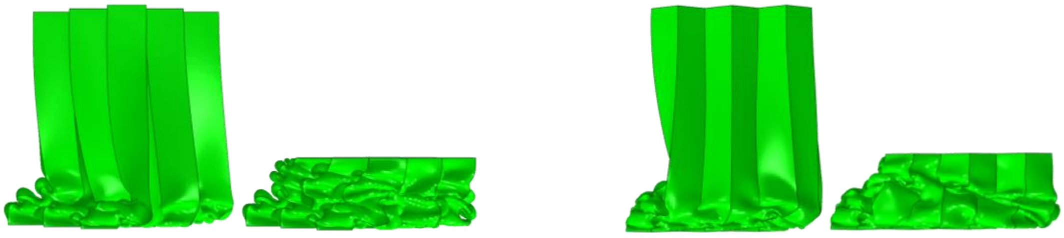

(g) O2 origami tube with 10° inclined loading (in direction 1).

(h) O2 origami tube with 10° inclined loading (in direction 2).

Figure 3.32. Deformation of O1 and O2 origami concave tubes under inclined loadings.

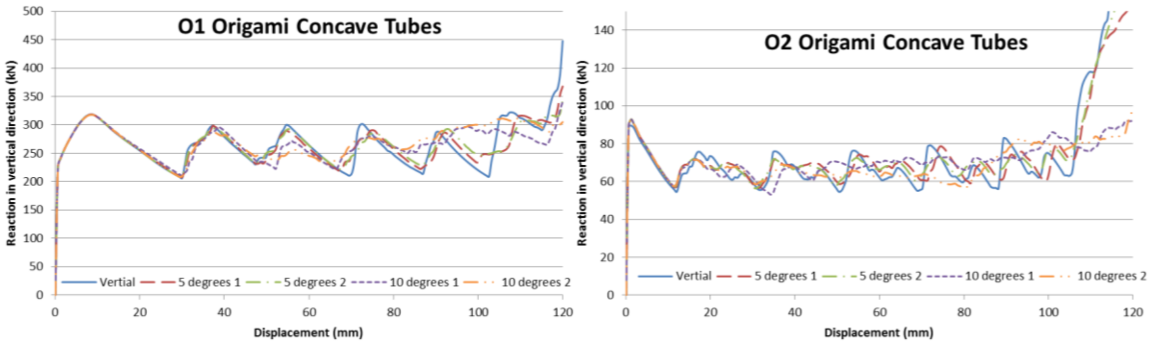

(a) (b)

Figure 3.33. Reaction to displacement plots of (a) O1 and (b) O2 origami concave tubes under inclined loadings.

3.8 Summary

The introduction of corrugated or concave cross-sections to thin-walled tubes can give ultra-high buckling force and multiple corners, which indicate the potential for high energy absorption. However, their unstable failure mode makes them unsuitable for energy absorbing applications as shown in Figure 3.34(a). The geometric solution of this issue is to introduce one layer of origami folds at one end of the tube, which works as an initiator to trigger a series of intriguing and progressive folds, shown in Figure 3.34(b). This simple intervention alters their failure modes from unstable to progressive and realizes their potential for high energy absorption.

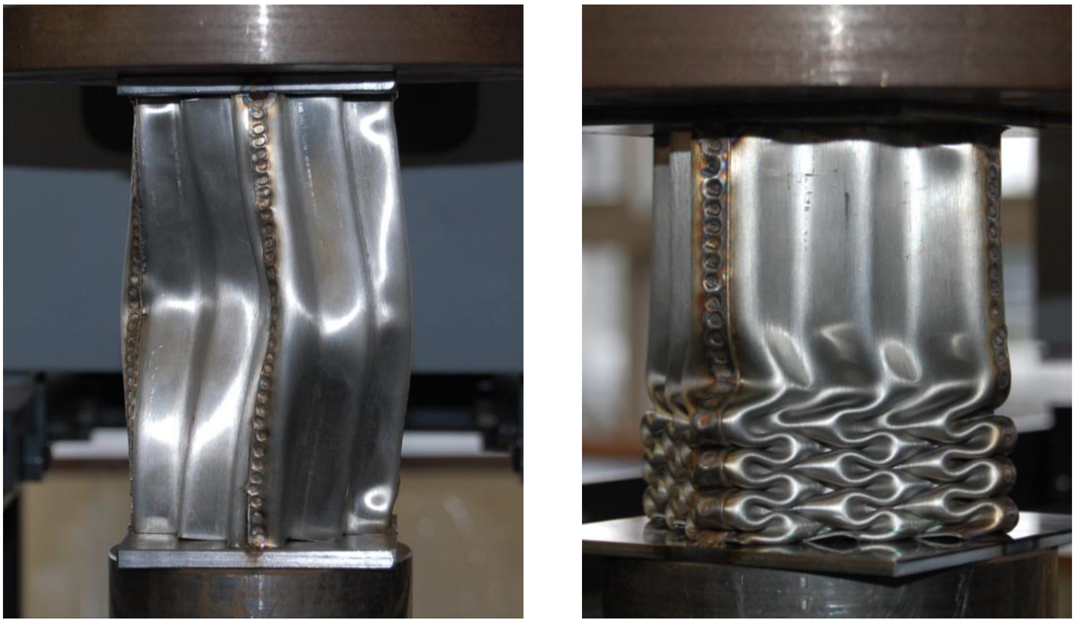

(a) (b)

Figure 3.34. Experimental failure modes of (a) normal concave tubes and (b) origami concave tubes.

This chapter has presented the design of origami concave tubes and demonstrated their superior energy absorbing performance than traditional square tube by experimental, numerical and theoretical studies. Specifically, mean crush force of origami concave tubes is two to four times of that of the square tube as shown in Figure 3.19.

Mean crush force of origami concave tubes can be conservatively estimated by simple theoretical models. Effects related to failure modes of origami concave tubes have been looked into, and appropriate geometric parameters have been worked out. Theoretical models and suggested range for parameters given by this chapter can give guidance for a quick future design of origami concave tubes. The performance of origami concave tube is not sensitive to practical geometric imperfection, boundary conditions, dynamic and inclined loading.

Due to the tremendous increase of energy absorbing ability brought by origami concave tubes, the application of them might contribute greatly to lighter weight vehicles and better protection of people during transportation.

Chapter 4 Inversion of Thin Corrugated Tubes

This chapter proposes to use thin corrugated tubes for inversion. Thin corrugated tubes have higher buckling force and lower inverting force than circular tubes, which contributes to more stable inversion process. In this chapter, the performance of thin circular tubes inversion is studied numerically first. Then inversion of thin corrugated tubes is introduced and numerically simulated. Theoretical modelling, experiments, and parametric study of inversion of thin corrugated tubes are carried out at last.

4.1 Circular Tubes Buckling and Inversion Revisit

4.1.1 Basic Settings

The setting for inversion is shown in Figure 4.1. A circular tube sat on a rigid die, and the top of the die was inserted into the bottom of the tube. Abaqus/Explicit (Abaqus, 2013) was used for simulation. 15700 S4R elements were used for meshing the tube, and the die was set as a rigid body (with 8753 R3D4 and 149 R3D3 elements). Convergence tests with respect to mesh density and analysis time were conducted prior to the analysis. Explicit Dynamic and general contact with penalty method for friction were used. The size of the die was slightly smaller than the tube. Material used in simulation was 304 stainless steel, which has density $\rho =$ 8030 kg/m^3, Young's Modulus E = 193 GPa, Poisson's ratio $\nu = 0.3$, yield stress σ_y = 241.3 MPa, ultimate stress σ_u = 679.6 MPa and strain ε_u = 55.8%, and strain hardening formula $\sigma = 1400\varepsilon^{0.43}$. Its stress-strain curve of the material is shown in Figure 4.2. The tubes had diameter $D = 50$ mm, and length $L = 100$ mm. Friction coefficient $\mu = 0.32$ which was validated in Section 4.4. Die radius r_{die} was chosen as 4 mm. Since it was pointed out by Reid, if the die radius is smaller than 4 mm (with $D = 50$ mm), it will make the leading edge of inverted part pressed against the tube and cause local buckling (Reid, 1993). The height of the die was 20 mm. Thickness t of the tube was set as 1 mm, 0.5 mm, 0.35 mm, and 0.25 mm respectively.

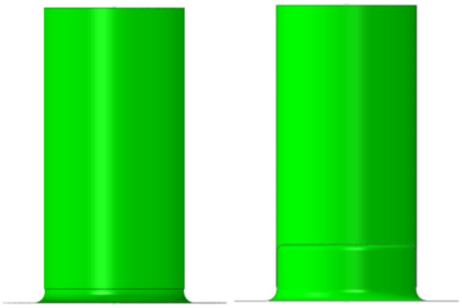

Figure 4.1. Side (in the left) and cut (in the right) views of setting of circular tube inversion.

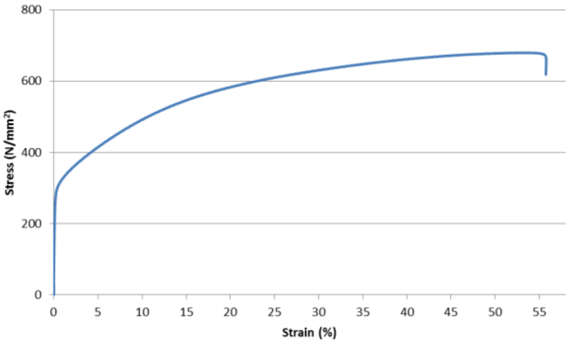

Figure 4.2. Stress strain curve of 304 stainless steel.

4.1.2 Buckling and Inversion of Perfect Circular Tubes with Various Thicknesses

Tubes were put into compression between two rigid plates (without die) to buckle, and also with help of die to be inverted respectively, which gave us both buckling force and inverting force (if inverted). Results of simulations are presented in Table 4.1, which shows that only tubes with $t = 0.35$ mm and 0.25 mm were inverted successfully. The ratio between buckling and inverting forces is defined as buckling force divided by inverting force. Successful inversion requires this ratio to be considerably larger than 1.

In Figure 4.3(a), a tube with $t = 1$ mm was put into direct compression between two rigid plates and was deformed by 2.5 mm, which made it buckle with axisymmetric mode. Figure 4.3(b) shows that the tube was inverted until compressed by 14.4 mm. It buckled with an axisymmetric mode afterward, shown in Figure 4.3(c). The relationship between reaction forces of both buckling and inverting process vs. axial displacement was plotted, shown in Figure 4.7(a), where reaction force is defined as total reaction force divided by cross-section area. The plot shows when reaction force of inversion reached the buckling force, it dropped down, and the tube started to buckle instead of continuing inversion. Buckling and inverting curves are using different displacement scales in the plots. Similar to $t = 1$ mm, a tube with $t = 0.5$ mm failed to invert, and buckled, shown in Figure 4.4 and Figure 4.7(b). However, from Figure 4.7(b), buckling reaction curve dropped more rapidly after its peak value comparing with $t = 1$ mm, which is indicating its increase of imperfection sensitivity. Buckling deformation of the tube with $t = 0.35$ mm is given in Figure 4.5(a), which shows axisymmetric buckling mode occurred. D/t ratio of this tube is 143, while non-symmetric buckling mode shall occur experimentally when $D/t > 90$ (Guillow et al., 2001). Based on this contradiction, it is expected that the buckling force has been slightly overestimated in this simulation comparing to the real situation. Figure 4.5(b) and (c) show that the tube was inverted successfully. It is shown in Figure 4.7(c) that buckling force of the tube was higher by 47.3 N/mm^2 than load required for inversion, which allowed the tube to be inverted instead of buckled. At the same time, it shall be noted that the buckling curve became steeper after the peak buckling force, and it suggests its higher imperfection-sensitivity. The tube with $t = 0.25$ mm again buckled in axisymmetric mode, shown in Figure 4.6(a), and succeeded in inversion, shown in Figure 4.6(b) and (c). From Figure 4.7(d), peak buckling load was higher than required inverting load by 49.9 N/mm^2, and the slope of post-buckling reaction curve after peak force was steepest. Figure 4.7 presents a clear relationship between reaction forces of tubes and their corresponding thicknesses.

Table 4.1: Results of circular tubes inversion with different thicknesses.

Tube	Failure mode	Buckling force (N/mm^2)	Inverting force (N/mm^2)	Ratio between buckling and inverting forces
$t = 1$	Buckled	334.4	-	-
$t = 0.5$	Buckled	302.7	-	-
$t = 0.35$	Inverted	291.5	244.2	1.19
$t = 0.25$	Inverted	281.6	231.7	1.22

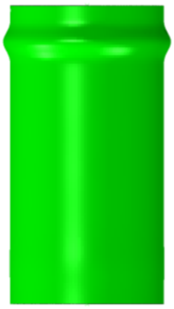

(a) Buckling analysis when displacement was 2.5 mm

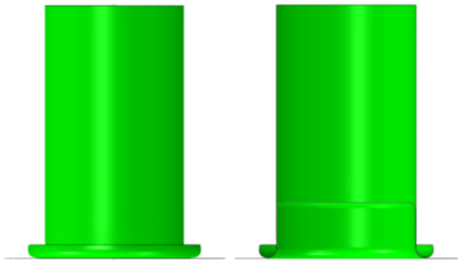

(b) Side and cut view of inverting analysis when displacement was 14.4 mm

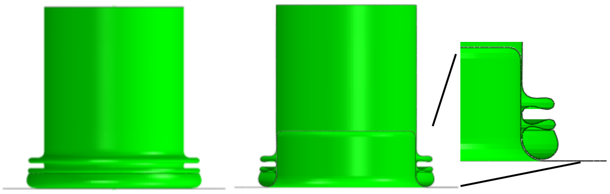

(c) Side and cut view of inverting analysis when displacement was 40 mm

Figure 4.3. Buckling and inverting of tube with $t = 1$ mm.

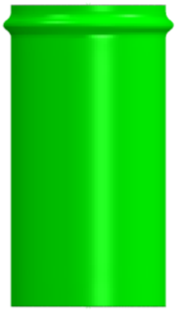

(a) Buckling analysis when displacement was 2.5 mm

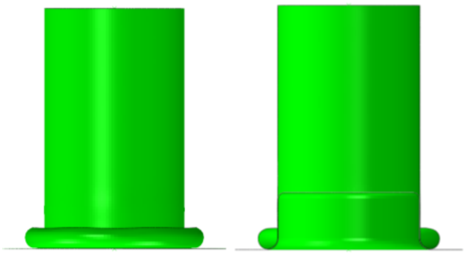

(b) Side and cut view of inverting analysis when displacement was 19.2 mm

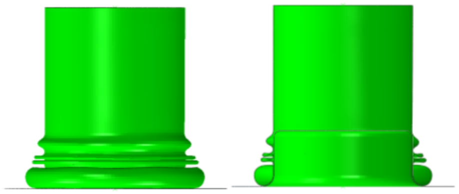

(c) Side and cut view of inverting analysis when displacement was 40 mm

Figure 4.4. Buckling and inverting of tube with t = 0.5 mm.

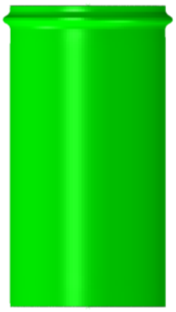

(a) Buckling analysis when displacement was 2.5 mm

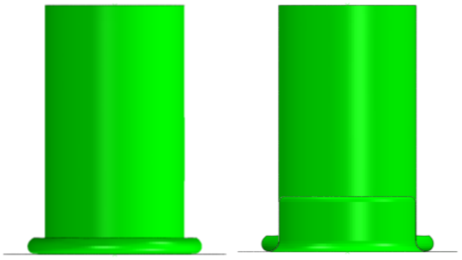

(b) Side and cut view of inverting analysis when displacement was 16 mm

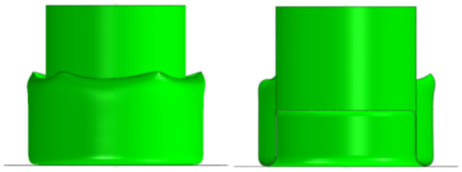

(c) Side and cut view of inverting analysis when displacement was 40 mm

Figure 4.5. Buckling and inverting of tube with t = 0.35 mm.

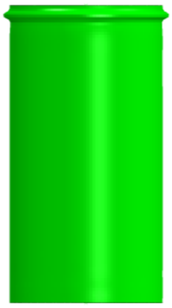

(a) Buckling analysis when displacement was 1.25 mm

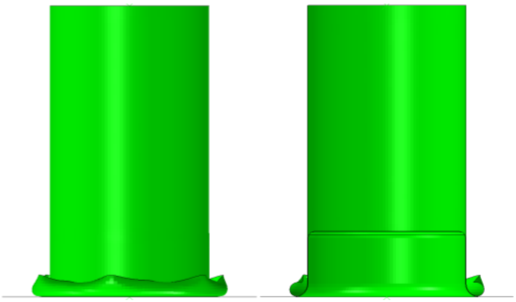

(b) Side and cut view of inverting analysis when displacement was 16 mm

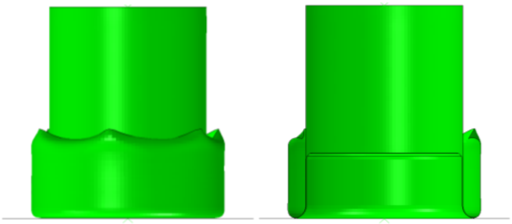

(c) Side and cut view of inverting analysis when displacement was 40 mm

Figure 4.6. Buckling and inverting of tube with t = 0.25 mm.

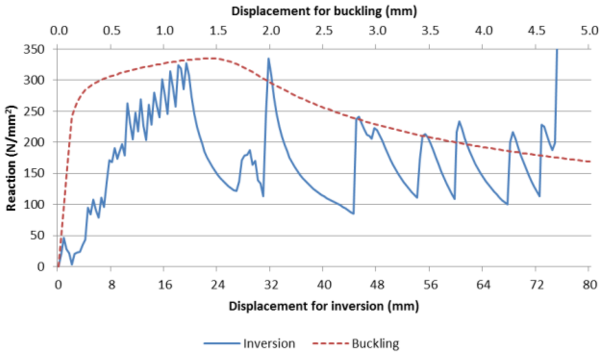

(a) *t* = 1 mm

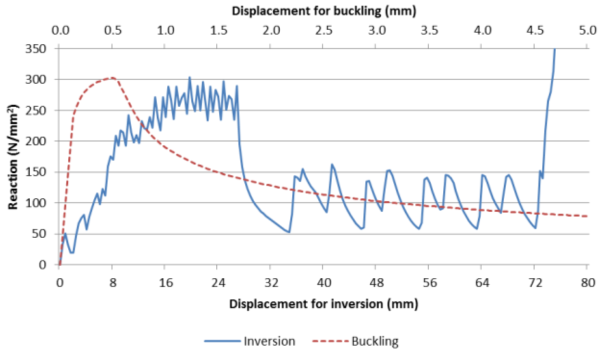

(b) *t* = 0.5 mm

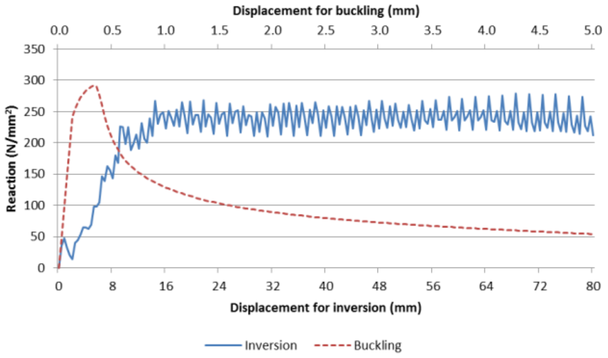

(c) *t* = 0.35 mm

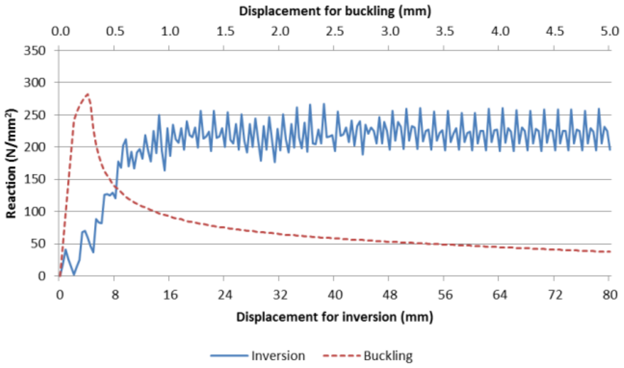

(d) *t* = 0.25 mm

Figure 4.7. Reaction versus displacement curves of buckling and inverting of tubes with (a) *t* = 1 mm, (b) *t* = 0.5 mm, (c) *t* = 0.35 mm, (d) *t* = 0.25 mm.

4.1.3 **Discussion**

In these simulations, it was demonstrated that tubes of 0.35 mm and 0.25 mm thickness could be inverted successfully with frictional contact ($\mu = 0.32$). In previous literature, no research of inverting thin circular tubes (D/t > 50) has been done or claimed the possibility of inverting tubes with frictional contact.

Significant local oscillation in Figure 4.7 can be noticed which mainly due to the transient effect of overclosure of the penalty contact. Comparing curves in Figure 4.7, buckling force (per area) was not reducing as much as load (per area) required for inversion with the decrease of shell thickness. This shows that thinner tubes have a relatively lower required force (per area) for inversion, comparing to its buckling load (per area). It helps tubes to be inverted more easily and even possible with frictional contact. However, for the post-buckling curves, the gradient after peak buckling load was getting steeper with reduction of thickness. It indicated the increase of imperfection sensitivity and raised the question of the reliability of these buckling loads.

From Figure 4.5(a) and Figure 4.6(a), tubes with 0.35 mm and 0.25 mm thickness, which had D/t ratio of 143 and 200 respectively, kept showing axisymmetric buckling mode. It is contradictory to experimental results that non-symmetric buckling mode shall occur when $D/t >$ 90 (Guillow et al., 2001). As a result, buckling force of tubes might be overestimated.

To solve these problems, introduction of imperfection to these thin tubes was proposed to investigate their realistic buckling forces.

4.1.4 Imperfect Circular Tubes Buckling and Inversion

In this sub-section, the buckling and inverting performances of imperfect tubes with 0.35 mm and 0.25 mm thickness were looked into. It showed that imperfection triggered non-symmetric buckling mode, and significantly reduced the buckling force to a lower value than the load required for inversion. In consequence, both of them resulted in buckling when they attempted for inversion.

Introducing imperfection

The imperfect shape was chosen as the first buckling mode, and its amplitude was 0.1 mm to represent experiments shown in Section 4.4, as direct experimental measurement such as 3D scanning was not available. Linear eigenvalue buckling analyses were carried out on previous perfect tubes with 0.35 mm and 0.25 mm thickness respectively, shown in Figure 4.8(a) and (b) and Figure 4.9(a) and (b). Figure 4.8(b) and Figure 4.9(b) show the first eigenmode for each tube. Then first eigenmodes were superimposed to their perfect shapes to get the imperfect shapes, shown in Figure 4.8(c) and Figure 4.9(c). Maximum transverse displacement of the first eigenmode was scaled to 0.1 mm when performing superposition. This imperfection mode and its corresponding amplitude are expected to produce the realistic buckling force of the tube (as compared with experiments later). Mode of buckling is not of interest in this research, as long as the imperfect tube is giving the realistic buckling force. Buckling force of the tube is the only controlling variable for successful inversion in this context as explained in Section 2.3. Inversion process itself is not sensitive to imperfection as there is no bifurcation.

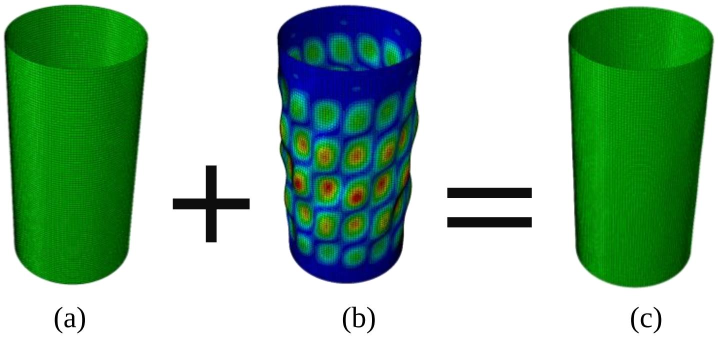
(a) (b) (c)

Figure 4.8. Tube with $t = 0.35$ mm. (a) Perfect circular shell; (b) imperfection shape based on first eigenmode with maximum transverse displacement of 2 mm for clarity; (c) tube with 0.1 mm imperfection amplitude.

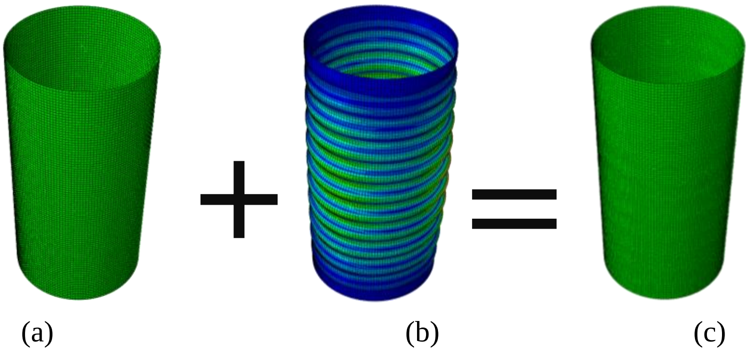
(a) (b) (c)

Figure 4.9. Tube with $t = 0.25$ mm. (a) Perfect circular shell; (b) imperfection shape based on first eigenmode with maximum transverse displacement of 2 mm for clarity; (c) tube with 0.1 mm imperfection amplitude.

Buckling and inversion of imperfect tubes with t = 0.35 mm and 0.25 mm

As the same in last sub-section, tubes were put under compression (without the help of die) to buckle, shown in Figure 4.10(a) and Figure 4.11(a). In Figure 4.10(b) and (c) and Figure 4.11(b) and (c), die was used for attempting to invert the tubes, but tubes buckled instead. Figure 4.12 shows that the reaction force for inverting process dropped down when it reached the peak value of the buckling load, which indicated the tube stopped to be inverted and started to buckle.

(a) Buckling analysis when displacement was 2.5 mm

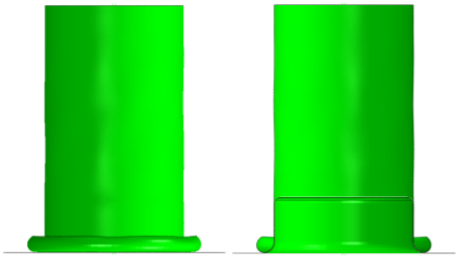

(b) Side and cut view of inverting analysis when displacement was 16 mm

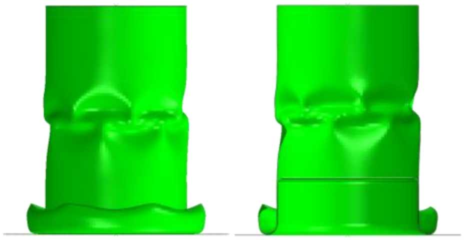

(c) Side and cut view of inverting analysis when displacement was 24 mm

Figure 4.10. Buckling and inverting of imperfect tube with $t = 0.35$ mm.

(a) Buckling analysis when displacement was 2.5 mm

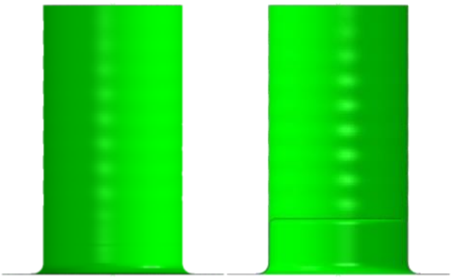

(b) Side and cut view of inverting analysis when displacement was 8 mm

(c) Side and cut view of inverting analysis when displacement was 16 mm

Figure 4.11. Buckling and inverting of imperfect tube with t = 0.25 mm.

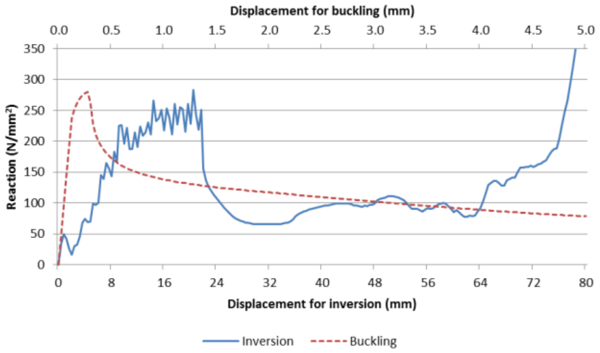

(a) t = 0.35 mm

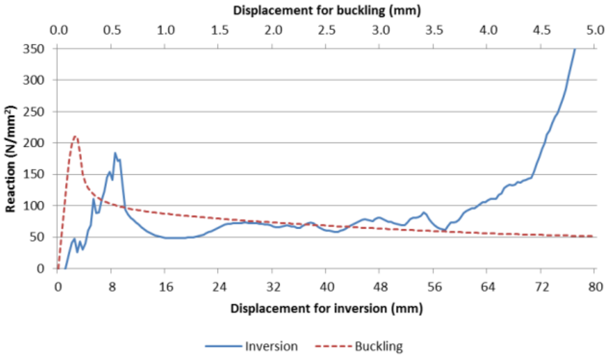

(b) t = 0.25 mm

Figure 4.12. Reaction force versus displacement curves of imperfect tube buckling and inverting with (a) t = 0.35 mm and (b) 0.25 mm.

Discussion

In this section, inversion of thin circular tubes ($D/t > 50$) was numerically simulated, and it demonstrated that thinner circular tubes (0.35 mm and 0.25 mm thickness) with perfect geometry could be inverted with frictional contact, which has not been achieved before in literature. However, its sensitivity to imperfection largely reduced its actual buckling force, so tubes failed to be inverted with a slightly imperfect geometry. Both imperfect 0.35 mm and 0.25 mm thickness tubes could not be inverted with frictional contact (μ=0.32), which shows that thinner tubes are sensitive to imperfection, and it largely affects its reliability in inversion.

A knockdown factor was used to evaluate the effect of imperfection, which is defined as the ratio between buckling load of imperfect and perfect shapes. Equation (7) shows the empirical equation of lower bound which gives a conservative value of knockdown factor based on its *D*/*t* ratio (Jones, 2006). Table 4.2 shows the comparison between the knockdown factors of both tubes with 0.35 mm and 0.25 mm thickness. Those knockdown factors are given by the simulation and Equation (7) respectively. For both 0.35 mm and 0.25 mm imperfect tubes, the buckling loads from simulation might still be overestimated. Even with that overestimated buckling load, those tubes could not be inverted successfully, which suggests their indeed incapability of inversion in real practice. This was confirmed by the experiment presented in Section 4.4. The required load for inverting 0.25 mm tube is at least 231.7 N/mm^2 (in Figure 4.7) which is well above 209.7 N/mm^2 (in Table 4.2).

Table 4.2: Effect of imperfection to buckling force.

Tube Thickness	Perfect Buckling Load Per Area (N/mm^2)	Imperfect Buckling Load Per Area (N/mm^2)	Knockdown Factor from Simulation	Knockdown Factor from Equation **(7)**
0.35 mm	291.5	274.4	0.941	0.630
0.25 mm	281.6	209.7	0.745	0.581

This section demonstrates that only by reducing the thickness of circular tube to ensure reliable tube inversion with frictional contact (μ=0.32) is not possible in reality, and further measures are needed.

4.2 Thin Corrugated Tube Inversion

In this section, both perfect and imperfect thin corrugated tubes were simulated for buckling and inversion. It was demonstrated that they could be inverted with both frictional contact (μ=0.32) and imperfection (amplitude=0.1 mm).

4.2.1 **Geometric Design**

The introduction of corrugation to tube cross-section can reduce its imperfection-sensitivity, and increase the buckling force (Ning and Pellegrino, 2013). It can also reduce load (per area) required for inversion due to its ease to be stretched circumferentially. These lead to the proposal of using the corrugated tube for inversion. Different shapes of corrugations were investigated in advance. Simple circular arcs were employed to form the corrugation, since it showed same buckling force as the optimized shape proposed by Ning (Ning and Pellegrino, 2013) within an interested range of D/t.

The design of corrugated tube and its die are shown in Figure 4.13. Figure 4.13(a) shows the cross-section of the tube, which can be determined by 3 independent parameters: R_{in}, A, and θ. R_{in} is the inner radius of the tube; A is ratio between the amplitude of corrugation and R_{in}; θ is the central angle corresponding to each corrugation. In Figure 4.13(a), r_1 and r_2 are the radiuses of corrugations and equal to each other. θ_1 and θ_2 are the corresponding central angles. R_{mid} and R_{out} are the middle and outer radiuses of the tube. R_{mid} is not halfway between R_{in} and R_{out}, but only corresponding to the switch between r_1 and r_2. L is the length of the tube, shown in Figure 4.13(b), and t is the material thickness. The shape of the die is similar to the one for circular tube inversion, shown in Figure 4.13(c). By satisfying geometric constraints (correspondence to θ and total amplitude of A), r_1 and r_2 can be solved and written as

$$r_1 = r_2 = \frac{R_{in}\left[A + A\tan^2\left(\frac{\theta}{2}\right) + 4\tan^2\left(\frac{\theta}{2}\right)\right]}{4} + \frac{R_{in}\tan^2\left(\frac{\theta}{2}\right)}{A}, \tag{15}$$

and expressions of θ_1 and θ_2 are

$$\theta_1 = \theta_2 = 2\arcsin\left[\frac{A^2\sin(\theta) + 2A\sin(\theta)}{2A - 2\cos(\theta) - 2A\cos(\theta) + A^2 + 2}\right]. \tag{16}$$

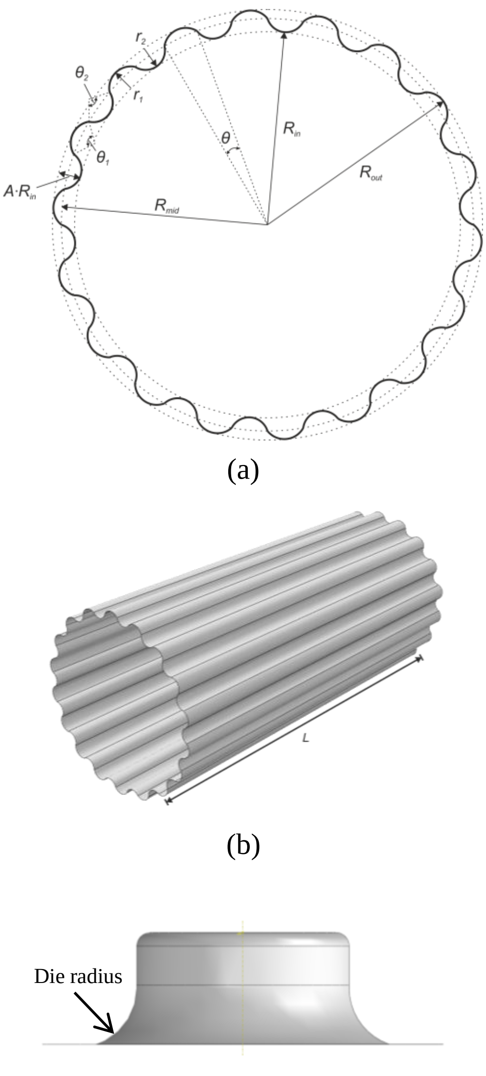

(a)

(b)

(c)

Figure 4.13. Design of corrugated tube and its die.

Parameters of the corrugated tube chosen for simulation are shown in Table 4.3, and the geometry of die was the same as the one for the circular tube, except for 6 mm die radius.

Table 4.3: Parameters used for the corrugated tube.

R_{in} (mm)	A	θ (°)	L (mm)
25	0.04	5	100

4.2.2 Perfect Corrugated Tubes Buckling and Inversion

The setting of tube inversion is shown in Figure 4.14. Same material and friction coefficient (μ=0.32) as previous sections were used. 72000 S4R elements were used to mesh the corrugated tube, and the die was set as a rigid body. Tubes with the thickness of 1 mm, 0.5 mm, 0.35 mm, and 0.25 mm were investigated, and perfect shapes were looked into in this sub-section, which were the same to circular tubes.

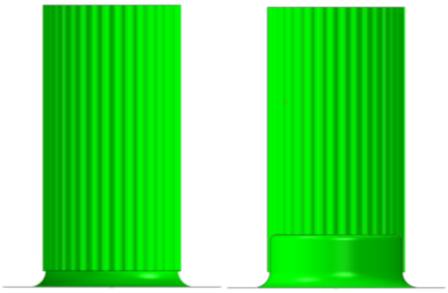

Figure 4.14. The setting of the inversion analysis.

Corrugated tubes with different thicknesses were put into compression (without die) to buckle and to invert (with help of die) respectively, which gave us both buckling force and inverting force. Results of simulations are presented in Table 4.4.

Corrugated tube (*t* = 1 mm) buckling and inverting analysis were done, shown in Figure 4.15, and the corrugated tube failed to be inverted just like the circular tube. Figure 4.19(a) shows the curves of buckling and inverting reaction forces to the crushing displacement. It can be noted that the tube failed to invert and started to buckle after its inverting reaction force reached the peak buckling load. Buckling and inverting analysis of corrugated tube with *t* = 0.5 mm was done, shown in Figure 4.16, and the corrugated tube succeeded to be inverted. Figure 4.19(b) shows the curves of buckling and inverting reaction forces to the crushing displacement. It shows that the peak buckling load was higher than the load needed for inverting, which allowed stable inversion instead of buckling. Corrugated tube with 0.35 mm thickness was inverted successfully, shown in Figure 4.17 and Figure 4.19(c). Corrugated tube with 0.25 mm thickness was also inverted successfully, shown in Figure 4.18 and Figure 4.19(d). Figure 4.19 shows the effect of reaction forces of buckling and inversion from the change of thickness. Slopes of buckling reaction forces right after peak force were significantly shallower than in Figure 4.7.

Table 4.4: Results of corrugated tubes inversion with different thicknesses.

Tube	Failure mode	Buckling force (N/mm^2)	Inverting force (N/mm^2)	Ratio between buckling and inverting forces
t=1	Buckled	328.1	-	-
t=0.5	Inverted	302.8	239.7	1.26
t=0.35	Inverted	293.7	208.2	1.41
t=0.25	Inverted	285.8	177.8	1.61

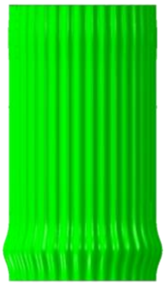

(a) Buckling analysis when displacement was 2.5mm

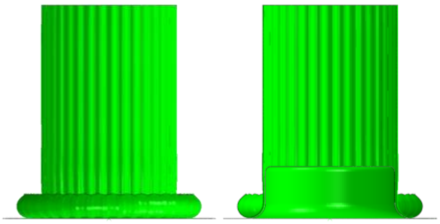

(b) Side and cut view of inverting analysis when displacement was 24 mm

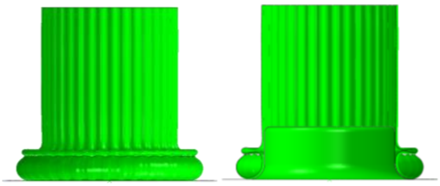

(c) Side and cut view of inverting analysis when displacement was 40mm

Figure 4.15. Buckling and inverting of corrugated tube with $t = 1$ mm.

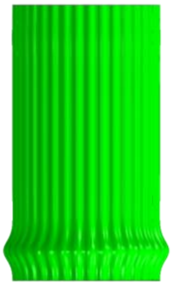

(a) Buckling analysis when displacement was 2.5mm

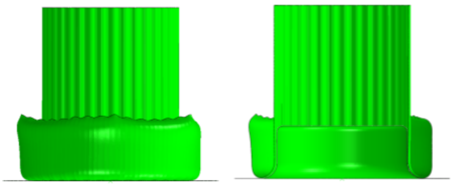

(b) Side and cut view of inverting analysis when displacement was 40mm

Figure 4.16. Buckling and inverting of corrugated tube with $t = 0.5$ mm.

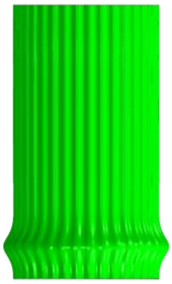

(a) Buckling analysis when displacement was 2.5mm

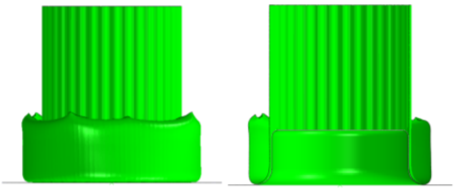

(b) Side and cut view of inverting analysis when displacement was 40mm

Figure 4.17. Buckling and inverting of corrugated tube with *t* = 0.35 mm.

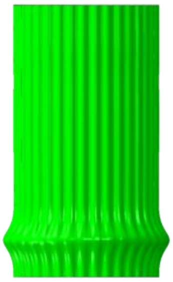

(a) Buckling analysis when displacement was 2.5mm

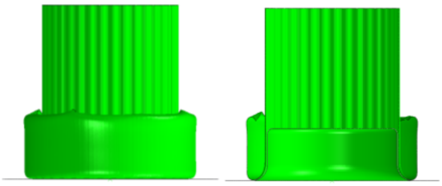

(b) Side and cut view of inverting analysis when displacement was 40mm

Figure 4.18. Buckling and inverting of corrugated tube with *t* = 0.25 mm.

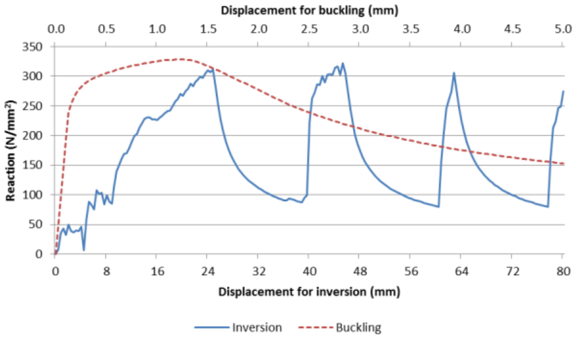

(a) *t* = 1 mm

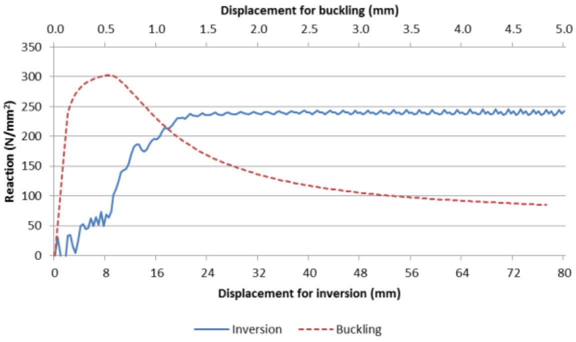

(b) *t* = 0.5 mm

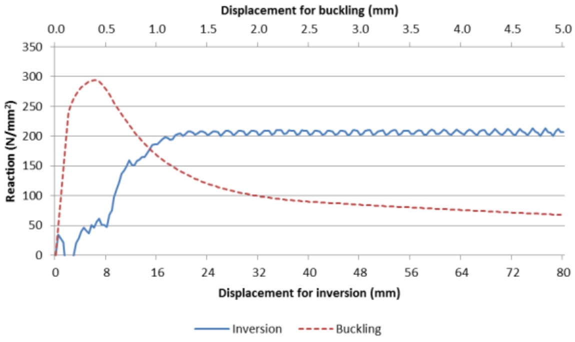

(c) *t* = 0.35 mm

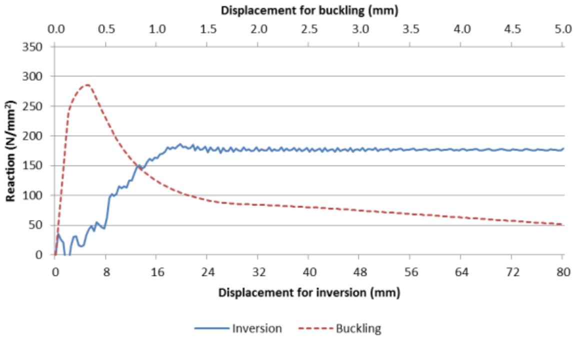

(d) *t* = 0.25 mm

Figure 4.19. Reaction force versus displacement curves of perfect corrugated tube buckling and inverting with (a) *t* = 1 mm, (b) 0.5 mm, (c) 0.35 mm, and (d) 0.25 mm respectively.

4.2.3 Imperfect Corrugated Tubes Buckling and Inversion

Similar to the previous section, imperfect shapes were generated by the superposition of perfect shape and its first eigenmode, as shown in Figure 4.20. Then similarly, imperfect corrugated tubes with 0.5 mm, 0.35 mm, 0.25 mm thicknesses were put under compression without and with the die, for buckling and inverting analysis respectively. All three tubes were inverted successfully, and results are presented in Table 4.5. Figure 4.21(a) shows the failure mechanism of corrugated tubes buckling, and Figure 4.21(b) shows that they were successful inverted. Plots of buckling and inverting reaction forces to the crushing displacement of three tubes are shown in Figure 4.22. Stable and almost reaction forces were observed for inversion process and were significantly lower than the buckling loads.

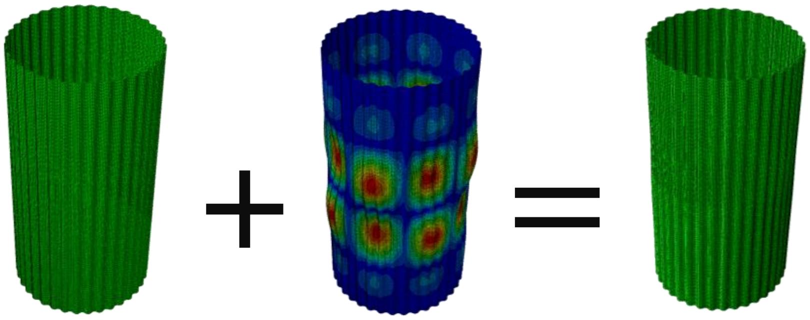

Figure 4.20. Corrugated tube with *t* = 0.5 mm. (a) Perfect shape; (b) imperfection shape based on first eigenmode with maximum transverse displacement of 2 mm for clarity; (c) tube with 0.1 mm imperfection amplitude.

Table 4.5: Results of imperfect corrugated tubes inversion with different thicknesses.

Tube	Failure mode	Buckling force (N/mm^2)	Inverting force (N/mm^2)	Ratio between buckling and inverting forces
t=0.5	Inverted	291.6	239.7	1.22
t=0.35	Inverted	279.2	208.2	1.34
t=0.25	Inverted	266	177.8	1.50

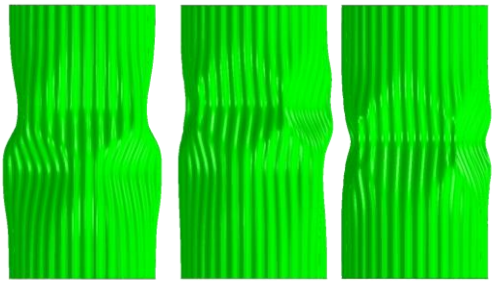

(a) *t* = 0.5 mm (b) *t* = 0.35 mm (c) *t* = 0.25 mm

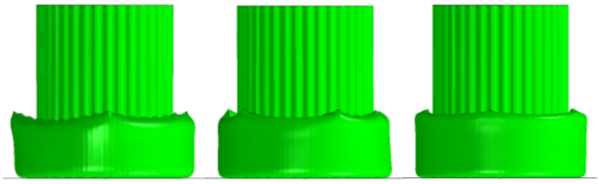

(d) *t* = 0.5 mm (e) *t* = 0.35 mm (f) *t* = 0.25 mm

Figure 4.21. Buckling and inverting analysis of imperfect corrugated tubes with 0.5 mm, 0.35 mm, 0.25 mm thickness.

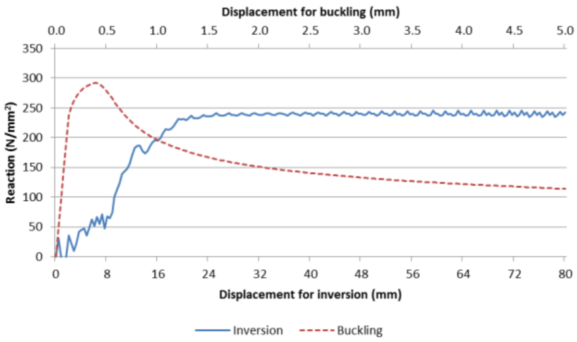

(a) *t* = 0.5 mm

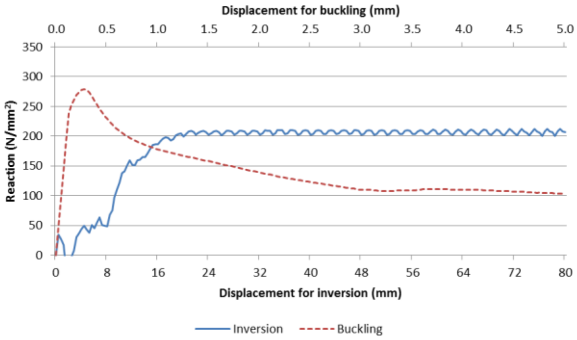

(b) *t* = 0.35 mm

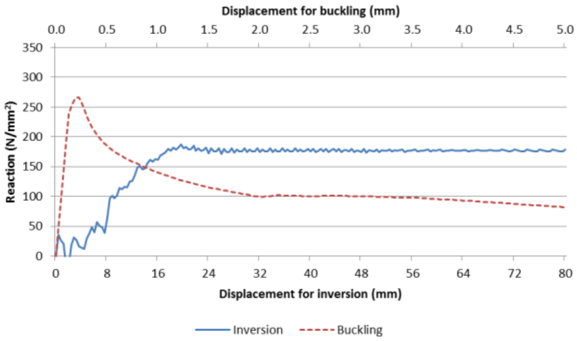

(c) *t* = 0.25 mm

Figure 4.22. Reaction force versus displacement curves of imperfect corrugated tubes buckling and inverting with (a) 0.5 mm, (b) 0.35 mm, (c) 0.25 mm thickness.

4.2.4 **Discussion**

Simulations showed that corrugated tubes were successfully inverted with friction and imperfection. Load (per area) required for corrugated tube inversion was decreasing more significantly with the reduction of thickness than buckling force, which was reflected by the ratio between two, shown in Table 4.5. By introducing the corrugation into thin-walled tubes, imperfect tubes could also be inverted with frictional contact. Knockdown factors of imperfect corrugated tubes are shown in Table 4.6. Comparison between Table 4.2 and Table 4.6 indicates that corrugated tubes can provide considerably higher and more reliable buckling force than the circular tube. Different buckling modes were applied respectively to circular tubes and corrugated tubes, which might affect the knockdown factor slightly. Additional to the improvement of buckling force, the load (per area) required for inversion was also decreased by adding corrugation due to less need for circumferential stretch, shown by comparison of Table 4.1 and Table 4.4. Direct comparison and improvement are given in Table 4.7. Even though FEA has many simplifying assumptions, it can be concluded that thin corrugated tubes can be hopefully inverted stably in a practical situation (frictional contact and imperfect geometry), when $D_{in}/t \geq 100$ is satisfied, where D_{in} is the inner diameter of the corrugated tube. Effects of other geometric parameters of the corrugated tube are discussed in Section 4.5.

Table 4.6: Effect of imperfection to buckling force.

Tube Thickness	Perfect Buckling Load Per Area (N/mm^2)	Imperfect Buckling Load Per Area (N/mm^2)	Knockdown Factor from Simulation
0.5 mm	302.8	291.6	0.963
0.35 mm	293.7	279.2	0.951
0.2 mm	285.8	266	0.931

Table 4.7: Comparison of buckling and inverting forces of circular and corrugated tubes.

Type	Perfect buckling force (N/mm^2)		Imperfect buckling force (N/mm^2)		Inverting force (N/mm^2)	
	0.35 mm	0.25 mm	0.35 mm	0.25 mm	0.35 mm	0.25 mm
Circular	291.5	281.6	274.4	209.7	244.2	231.7
Corrugated	293.7	285.8	279.2	266	208.2	177.8
Improvement	0.75%	1.49%	1.75%	26.85%	14.74%	23.26%

4.3 Theoretical Modelling of Corrugated Tube Inversion

In this section, a theoretical model for the inverting force of corrugated tube was developed, and it can give a quick estimation of its energy absorbing ability.

4.3.1 Analysis and assumptions

Simulation and simplified mechanism of corrugated tube inversion are shown in Figure 4.23. There are three distinct deformed regions: an inverted toroidal region of which one half conforms to the shape of the die and being symmetrical on the other side, which “travels” though the original cylinder; a largely undeformed original cylinder above the torus, which shortens; and a deformed inverted part which is uncorrugated and lengthens. It is expected the inverting force to be constant even though the level of deformation increases. The corresponding three types of energy in this process, which are named as E_1, E_2, and E_3 respectively, and noted in Figure 4.23(a). When the tube is compressed, the corrugated tube conforms to the shape of the die and starts to unfold its corrugation. This portion of plastic energy is noted as E_1, and is considered as rotation of stationary hinges. The bending energy of material being rolled up is noted as E_2, which is considered as travelling hinges (Wierzbicki, 1983). The stretching energy in this process is noted as E_3.

In order to simplify the model, uncoupling of these three types of energy is assumed: the corrugated tube firstly completes losing its corrugation (E_1), and then starts to invert (E_2 and E_3). E_2 and E_3 will be calculated according to Figure 4.23(b), where R_c is the radius when the tube fully loses its corrugation and it can be calculated by treating the total circumference as for circular tube, and written as

$$R_c = \frac{(r_1\theta_1 + r_2\theta_2)n_0}{2\pi} , \tag{17}$$

where θ_1 and θ_2 are the respective central angles of corrugations, shown in Figure 4.23 (c). n_0 is the number of corrugation pairs which is 18 for the cross-section shown in Figure 4.23 (c).

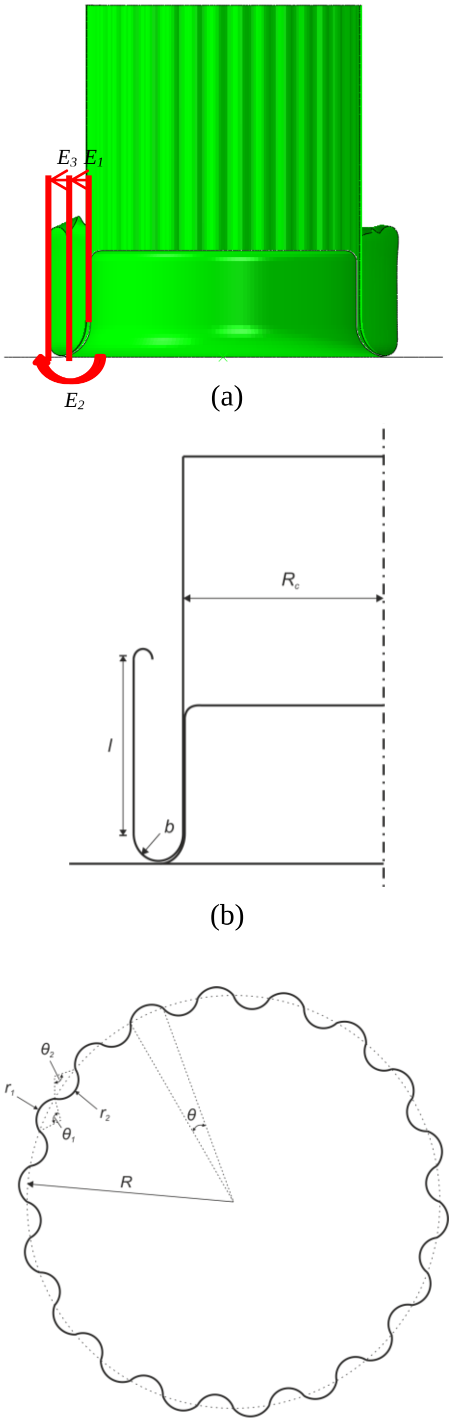

(a)

(b)

(c)

Figure 4.23.Simulation and simplified mechanism of corrugated tube inversion, (a) simulation with three types of energy noted, (b) simplified mechanism, and (c) cross-section of corrugated tube with parameters.

4.3.2 **Calculation of Energy and Reaction Force**

Energy used for unfolding the corrugation (E_1) can be written as

$$E_1 = (\theta_1 + \theta_2) n \cdot M_p \cdot l \,, \tag{18}$$

where M_p is the plastic moment per unit length, and l is the length that has been inverted, shown in Figure 4.23 (b). Energy from travelling hinge lines (E_2) can be expressed as $2\frac{M_P}{b}$ multiplied by the area swiped through by the entire travelling plastic hinge lines (Lu and Yu, 2003b). Then it can be written as

$$E_2 = 4\pi \frac{M_p}{b} \cdot R_c \cdot l \,, \tag{19}$$

where b is the radius of the bending, shown in Figure 4.23(b). The radius of the tube increased by stretching effect is $2b$, and corresponding strain is $2b/R_c$. The area of surface passing through the toroidal region is $2\pi R_c l$. Then the stretching energy (E_3) is

$$E_3 = 4\pi \cdot b \cdot l \cdot N_y \,, \tag{20}$$

where N_y is yielding force per unit length.

Combining all three sources, the total energy is

$$E_{total} = (\theta_1 + \theta_2) n \cdot M_p \cdot l + 4\pi \frac{M_p}{b} \cdot R_c \cdot l + 4\pi \cdot b \cdot l \cdot N_y \,, \tag{21}$$

which has the minimum value when $E_2 = E_3$ after differentiating Equation (21) with respect to b and setting equal to zero. This gives

$$b = \sqrt{\frac{M_p}{N_y} R_c} \cdot \quad (22)$$

Stress-strain curves of 304 stainless steel is fitted as

$$\sigma = 1400\varepsilon^{0.43}\,\text{MPa}, \quad (23)$$

where σ is the stress and ε is the strain. Equivalent plastic flow stress σ_0 can be calculated as (Ma and You, 2013b)

$$\sigma_0 = \sqrt{\frac{\sigma_y \sigma_u}{1 + m_p}}, \quad (24)$$

where m_p is power exponent in stress-strain curve, and equals to 0.43 for 304 stainless steel. This value can replace the non-linear stress-strain curve to a constant and used for calculation of yielding force and plastic moment. $M_p = \sigma_0 \frac{t^2}{4}$, $N_y = \sigma_0 \cdot t$, and t is the material thickness. By substituting Equation (22) into (21), it gives

$$E_{total} = \sigma_0 \cdot l \left[\frac{1}{4}(\theta_1 + \theta_2) n \cdot t^2 + 4\pi \cdot t \cdot \sqrt{t \cdot R_c} \right]. \quad (25)$$

The reaction force F' is constant since the linear relationship between E_{total} and l, which is

$$F' = \sigma_0 \cdot \left[\frac{1}{4}(\theta_1 + \theta_2) n \cdot t^2 + 4\pi \cdot t \cdot \sqrt{t \cdot R_c} \right]. \quad (26)$$

Since the uncoupling assumption and constraints of the die, the model is obviously underestimating the energy of (E_2+E_3). An empirical ratio η = 1.3 is applied to (E_2+E_3) to better fit experimental data. In consequence, the final expression of reaction force (frictionless) is

$$F = \sigma_0 \cdot \left[\frac{1}{4}(\theta_1 + \theta_2) n \cdot t^2 + \eta \cdot 4\pi \cdot t \cdot \sqrt{t \cdot R_c} \right]. \tag{27}$$

Reid (Reid, 1993) attempted to give a simple expression of friction contribution to reaction force, and its result is not matching well for this case. Empirical curve fitting was used in this case for better accuracy, shown in Figure 4.24. Horizontal axis is the actual friction coefficient between the contact surfaces, while vertical axis is the equivalent friction coefficient, which is defined by the ratio between additional reaction force in frictional contact (comparing with frictionless contact) to reaction force without friction. Data points in the graph are from numerical simulations. An empirical relationship between actual friction coefficient and equivalent friction coefficient is established.

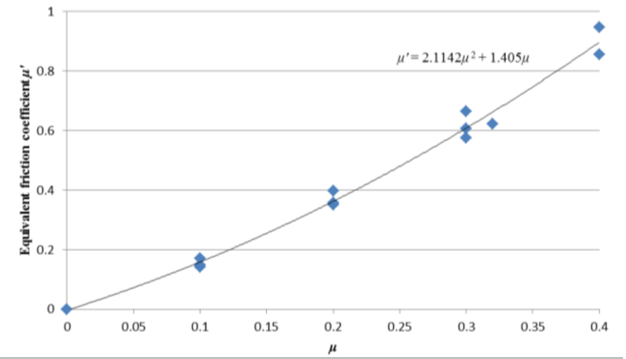

Figure 4.24. Relationship between equivalent friction coefficient to the actual value.

The resultant expression of equivalent frictional coefficient is

$$\mu' = 2.114\mu^2 + 1.405\mu\,, \tag{28}$$

where μ is the friction coefficient of the contact. Frictional reaction force F_f can be written as

$$F_f = (1+\mu') \cdot \sigma_0 \cdot \left[\frac{1}{4}(\theta_1 + \theta_2) n \cdot t^2 + \eta \cdot 4\pi \cdot t \cdot \sqrt{t \cdot R_c} \right]. \tag{29}$$

Its comparison with numerical and experimental results is presented in Section 4.4 and 4.5.

4.4 Experiments of Circular and Corrugated Tubes Inversion

In this section, inversion of circular and corrugated tubes was experimentally tested, and directly showed the improvement of corrugated tube inversion. In the other hand, numerical and theoretical models were compared with and verified by experimental results.

4.4.1 Manufacturing and Setting of Experiment

Test specimens and dies are presented in Figure 4.25. 1 circular tube, which was named as Cir1, and 3 corrugated tubes, which were named as Cor1, Cor2 and Cor3, were manufactured by wire electrical discharging machine, which cut them though electrochemical corrosion from solid 304 stainless steel rod. There was not residual stress generated from this manufacturing process, since no deformation or heat was introduced. Die4 with r_{die} = 4 mm and Die6 with r_{die} = 6 mm are shown in Figure 4.25, which were made from Carrs P552. Instron 5982 was used for compression tests, and setting of tests is shown in Figure 4.26. The speed of displacement loading was 10 mm/min, and no lubrication was used for the contact. The geometries of these specimens were same with those in Section 4.1 and Section 4.2, and all their wall thicknesses were intended for 0.25 mm. However, due to the manufacturing issue, the thickness of Cor2 and Cor3 was 0.29 mm. Practical imperfection was generated in these tubes from manufacturing and transporting process.

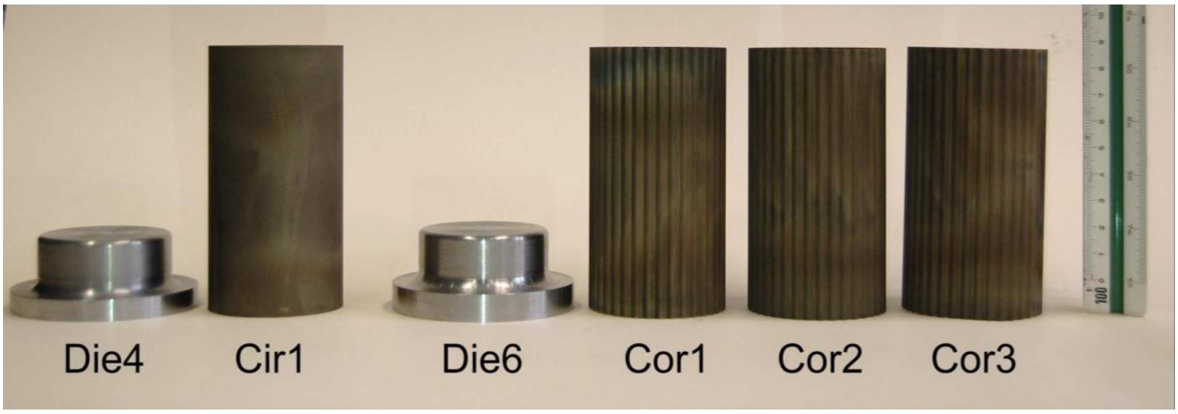

Figure 4.25. Test specimens and dies.

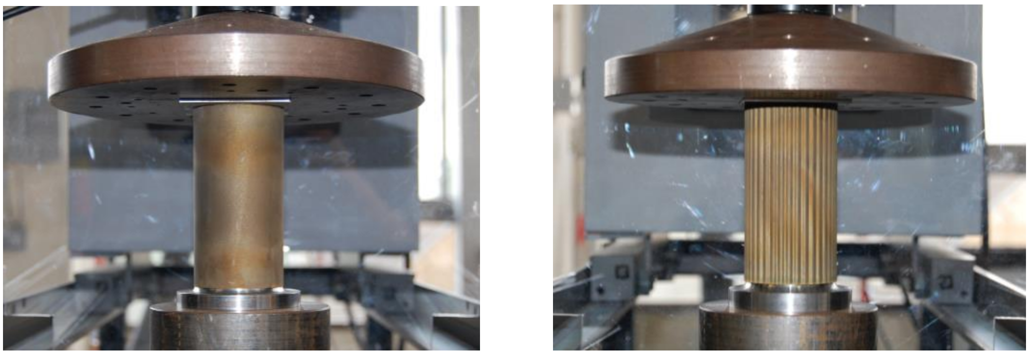

(a) (b)

Figure 4.26. Compression test settings of (a) circular tube and (b) corrugated tube.

4.4.2 Experimental Results and Comparison with Numerical and Theoretical Models

Experiments and corresponding numerical simulations were performed. μ = 0.32 and 0.1 mm imperfection amplitude were used in numerical simulations. Experimental and numerical deformation of circular tube inversion and comparison of their results are given in Figure 4.27. Both experiment and simulation showed that the circular tube failed to be inverted. In the experiment, the circular tube developed axisymmetric concertina folding at first with the lateral support from the die, and then quickly switched to non-axisymmetric mode. In the simulation, the tube failed only in non-axisymmetric mode. This discrepancy is reflected in the plots shown in Figure 4.27(c) that experimental result had three obvious peak values while the numerical result had only one. The buckling forces of both results were almost identical, which suggests that 0.1 mm amplitude for imperfection was reasonable.

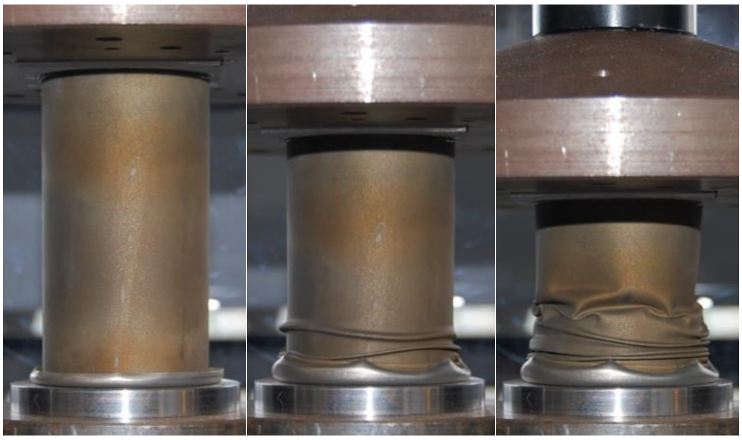

(a) Experimental deformation with displacements of 10 mm, 30 mm, and 50 mm respectively.

(b) Numerical deformation with displacements of 10 mm, 30 mm, and 50 mm respectively.

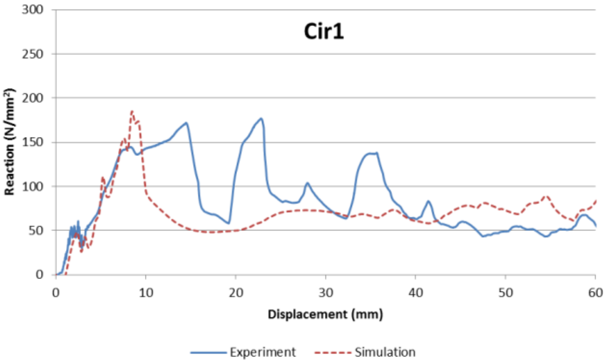

(c) Plots of experimental and numerical results.

Figure 4.27. Experimental and numerical results of circular tube inversion.

Inversion of corrugated tubes with *t* = 0.25 mm and 0.29 mm is presented in Figure 4.28 and Figure 4.29 respectively, which show that corrugated tubes were successfully inverted with no lubrication. Generally, good consistency between experimental and numerical results was observed in terms of both deformation and reaction curve.

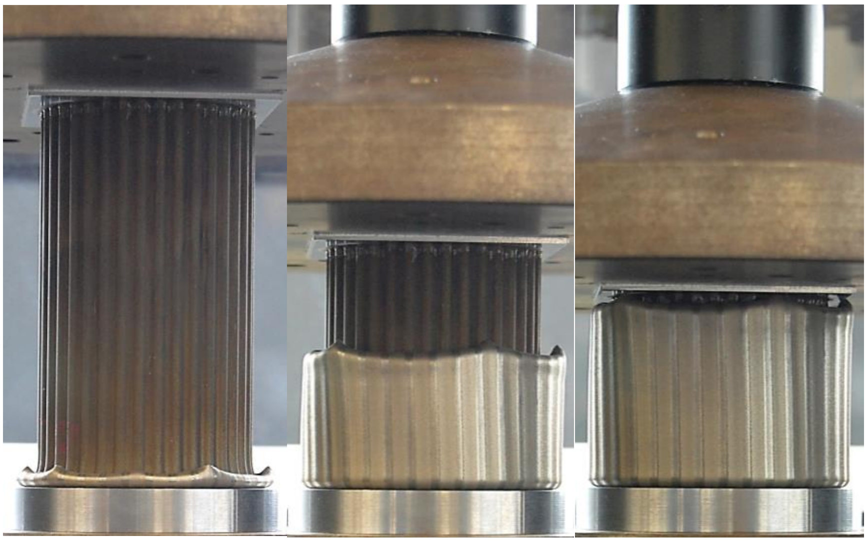

(a) Experimental deformation of Cor1 with displacements of 13.3 mm, 46.7 mm, and 60 mm respectively.

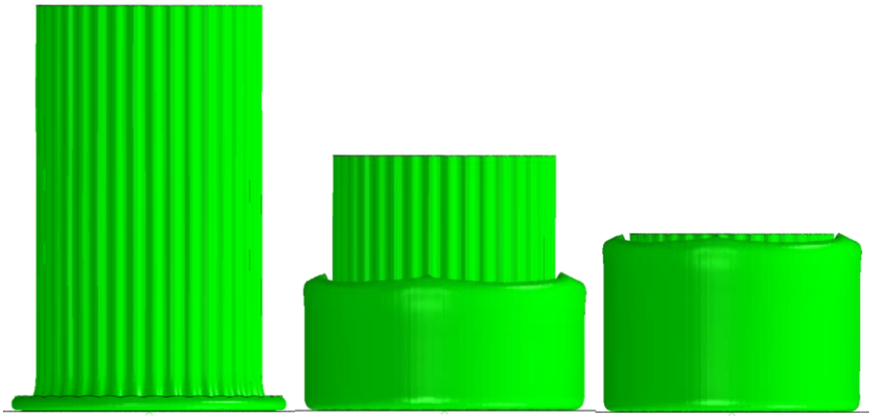

(b) Numerical deformation of Cor1 with displacements of 13.3 mm, 46.7 mm, and 60 mm respectively.

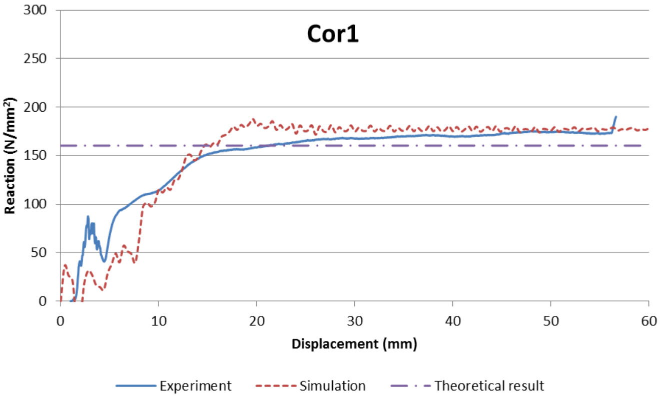

(c) Plots of experimental and numerical results.

Figure 4.28. Experimental and numerical results of corrugated tube inversion with *t* = 0.25 mm.

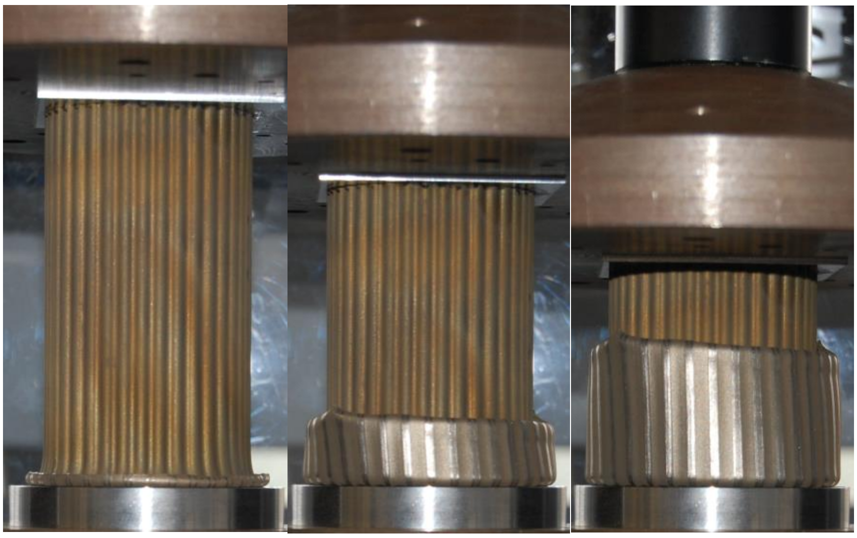

(a) Experimental deformation of Cor2 with displacements of 10 mm, 30 mm, and 50 mm respectively.

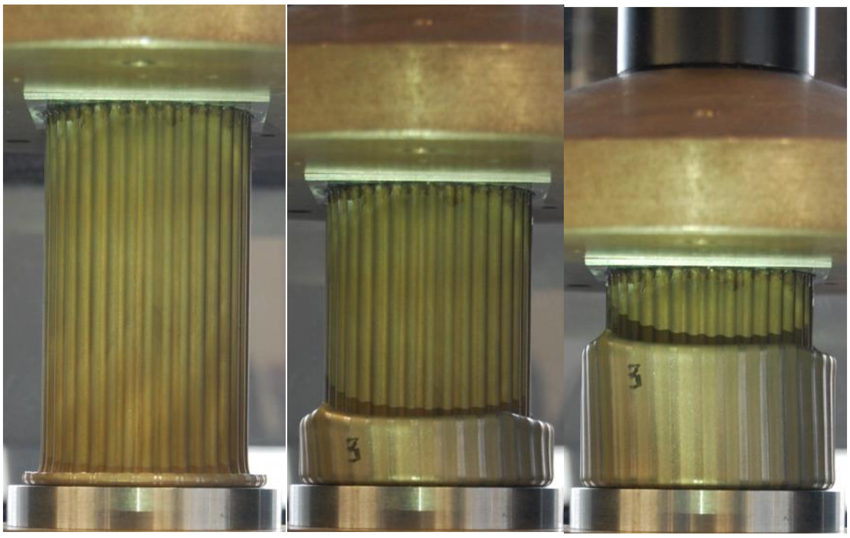

(b) Experimental deformation of Cor3 with displacements of 10 mm, 30 mm, and 50 mm respectively.

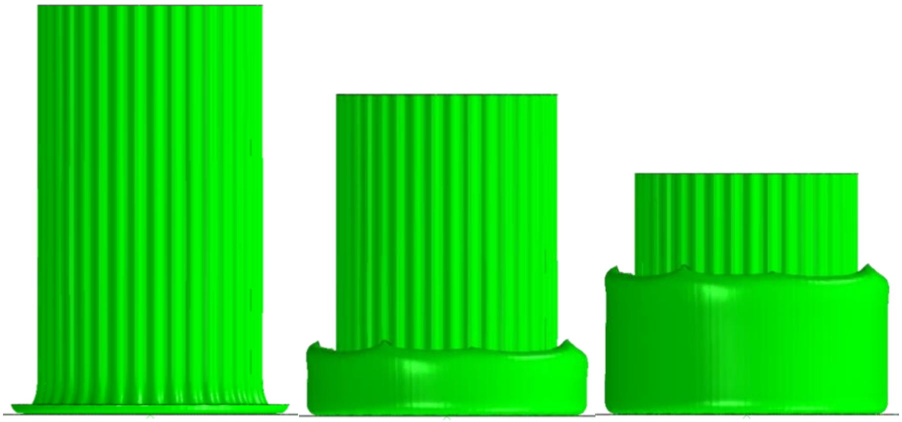

(c) Numerical deformation with displacements of 10 mm, 30 mm, and 50 mm respectively.

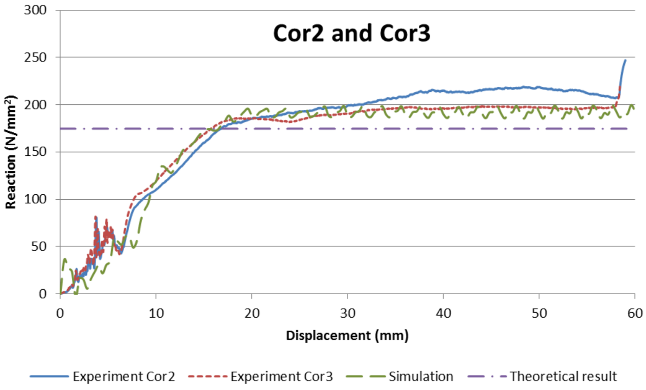

(d) Plots of experimental and numerical results.

Figure 4.29. Experimental and numerical results of corrugated tubes inversion with *t* = 0.29 mm.

In Figure 4.29(d), the reaction force of Cor2 gradually rose up after displacing 30 mm, which was due to its self-contact between the inverted outer tube and the inner tube at two sides, shown in Figure 4.30. The reaction force of numerical simulation matched the experimental result, and this indicates that $\mu = 0.32$ was realistic. Theoretical results according to Section 4.3 are also plotted in Figure 4.28(c) and Figure 4.29(d), and show good uniformity. All tested specimens are presented in Figure 4.31. It shows that Cir1 was buckled, and Cor1, Cor2, and Cor3 were successfully inverted.

Figure 4.30. Self-contact of Cor2.

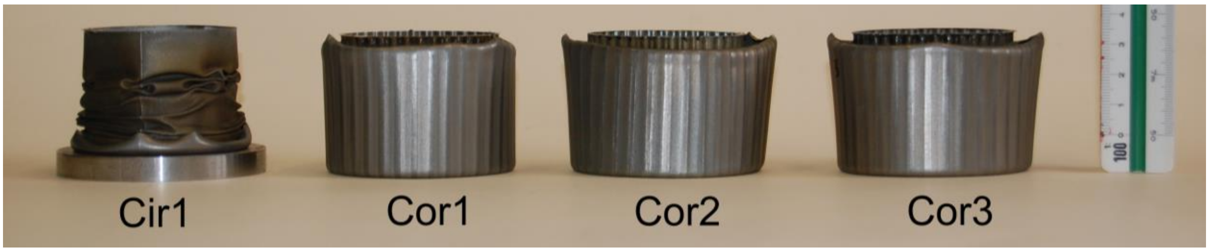

Figure 4.31. Tested specimens.

4.4.3 **Discussion**

It was experimentally demonstrated that without any lubrication thin circular tube could not be inverted, while thin corrugated tubes could. This directly proves the validity of the idea of using thin corrugated tubes for inversion. By achieving good consistency of numerical and theoretical results with the experimental outcome, the effectiveness of both numerical and theoretical technics was confirmed.

4.5 Parametric Study

The further parametric study was carried out and presented in this section, and produced a preferable range of parameters to assist future design.

Corrugated tubes with different thicknesses and geometries were numerically simulated. θ, which is the corresponding central angle to each arc, was altered to different values as illustrated in Figure 4.32(a), as well as the value of A, which is the amplitude of corrugation and is illustrated in Figure 4.32(b). Simulation results with corresponding tube parameters as well as theoretical results are shown in Table 4.8. All tubes had a length of 100 mm, R_{in} of 25 mm, and the same material as previous sections. Since corrugated tubes are insensitive to imperfection as demonstrated previously, no imperfection was added for simplification. Friction coefficient was amplified to 0.4 in this section for conservation.

Failure modes can be categorised as *inverted*, *buckled*, and *twisted*. Inverted and buckled failures are extensively presented in Section 4.2. Twisted mode occurs when A/θ is relatively large comparing to t, and material buckles locally, shown in Figure 4.33. Tubes might still be able to be inverted after twisted mode occurs as shown in Figure 4.33(a), or buckled because the twisting causes tangling as shown in Figure 4.33(b). The relationship between buckling to inverting ratio (the last column of Table 4.8) and geometrical parameters is given in Figure 4.34. Buckling to inverting ratio is defined as buckling force of a corrugated tube divided by the inversion reaction force of the same corrugated tube. This ratio is used as an index for the reliability of inversion. Figure 4.34 shows that higher A and smaller θ give higher buckling to inverting ratio, and this stands for higher reliability of successful tube inversion. Comparison between numerical and theoretical results is presented in Figure 4.35, which shows rough match between the two. The average error of 22.6 % indicates that theoretical model presented in Section 4.3 can only be used for approximate estimation of energy absorbing ability of the design. Scalability has been checked. Preferable ranges of parameters are suggested in Table 4.9, which can be regarded as a guide for design. Desirable die radius shall be around $\frac{\theta_1 r_1 + \theta_2 r_2}{2\theta} - R_{in}$, which is calculated by letting material of the tube just reach the end of the arc in die when got fully uncorrugated. This value needs to be greater or at least equal to 4 mm for avoiding self-contact when rolls up.

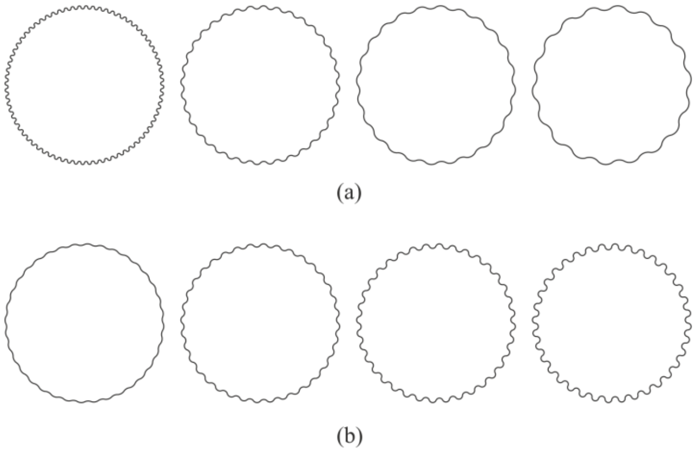

Figure 4.32. Illustration of different values of θ and A.

Table 4.8: Results of parametric study.

Model	t (mm)	θ (°)	A	die radius (mm)	cross-sectional area (mm^2)	Failure mode	Buckling force (N/mm^2)	Numerical inverting force (N/mm^2)	Theoretical inverting force (N/mm^2)	Ratio between buckling and inverting forces
A1_1	0.5	2.5	0.01	4	81.65	Buckled	299.9	-	295.6647	-
A1_2	0.5	2.5	0.02	6	89.82	Inverted	298.1	265.9	331.1359	1.12
A1_3	0.5	2.5	0.03	8	102.23	Inverted	292.9	226.6	342.3021	1.29
A1_4	0.5	2.5	0.04	10	117.98	Inverted	296.4	194.5	336.7961	1.52
B1_1	0.5	5	0.02	4	82.07	Buckled	303.3	-	262.9482	-
B1_2	0.5	5	0.04	6	90.54	Inverted	304.3	278.8	274.3796	1.09
B1_3	0.5	5	0.06	8	103.15	Inverted	301.3	227.6	272.5238	1.32
B1_4	0.5	5	0.08	10	119.00	Inverted	299.7	204.4	262.5192	1.47
C1_1	0.5	7.5	0.04	4	84.93	Buckled	306.6	-	253.9645	-
C1_2	0.5	7.5	0.06	6	91.29	Buckled	306.8	-	254.8424	-
C1_3	0.5	7.5	0.08	6	99.44	Buckled	306.0	-	251.489	-
C1_4	0.5	7.5	0.1	10	109.12	Inverted	301.7	273.8	245.2009	1.10
D1_1	0.5	10	0.06	4	86.97	Buckled	309.9	-	246.2641	-
D1_2	0.5	10	0.08	6	92.06	Buckled	309.7	-	244.6045	-
D1_3	0.5	10	0.1	8	98.14	Buckled	306.6	-	241.0853	-
D1_4	0.5	10	0.12	10	105.09	Buckled	311.6	-	236.1953	-
A2_1	0.25	2.5	0.01	4	40.83	Inverted	279.7	223.5	195.8919	1.25
A2_2	0.25	2.5	0.02	6	44.91	Inverted	280.5	196.8	211.3945	1.42
A2_3	0.25	2.5	0.03	8	51.11	Inverted	275.7	164.2	214.1088	1.68
A2_4	0.25	2.5	0.04	10	58.99	Inverted	271.2	135.8	208.3754	2.00
B2_1	0.25	5	0.02	4	41.03	Inverted	285.7	227.8	179.4116	1.25
B2_2	0.25	5	0.04	6	45.27	Inverted	287.3	200.4	182.8321	1.43
B2_3	0.25	5	0.06	8	51.58	Inverted	282.2	175.9	179.0213	1.60
B2_4	0.25	5	0.08	10	59.50	Inverted	279.2	156.8	171.0745	1.78
C2_1	0.25	7.5	0.04	4	42.46	Inverted	289.2	224.2	174.1097	1.29
C2_2	0.25	7.5	0.06	6	45.64	Inverted	289.6	245.4	172.8774	1.18
C2_3	0.25	7.5	0.08	6	49.72	Inverted + twisted	284.3	213.6	169.2936	1.33
C2_4	0.25	7.5	0.1	10	54.56	Inverted + twisted	286.5	206.0	164.1773	1.39
D2_1	0.25	10	0.06	4	43.48	Inverted + Buckled	291.3	-	169.7	-
D2_2	0.25	10	0.08	6	46.03	Inverted + Twisted + Buckled	287.2	-	167.5635	-
D2_3	0.25	10	0.1	8	49.07	Inverted + Twisted + Buckled	291.4	-	164.3792	-
D2_4	0.25	10	0.12	10	52.55	Inverted + Twisted + Buckled	288.3	-	160.4628	-

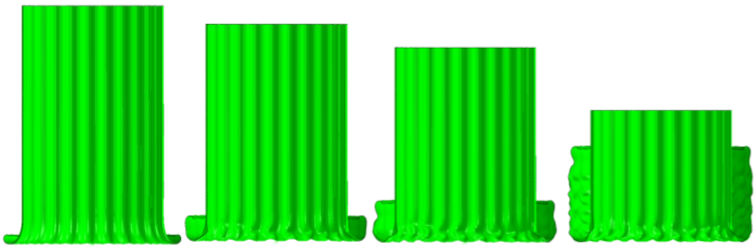

(a) Inverted with displacement of 16 mm, 24 mm, 32 mm, 56 mm.

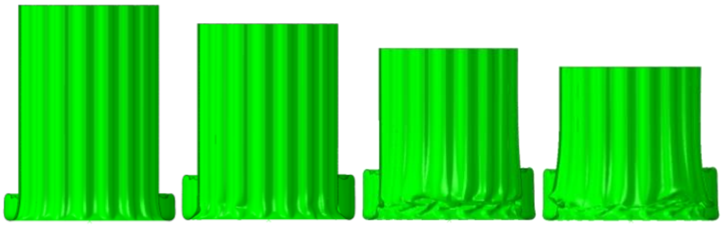

(b) Buckled with displacement of 24 mm, 32 mm, 40 mm, 48 mm.

Figure 4.33. Deformation of twisted mode (cut view with removal of die).

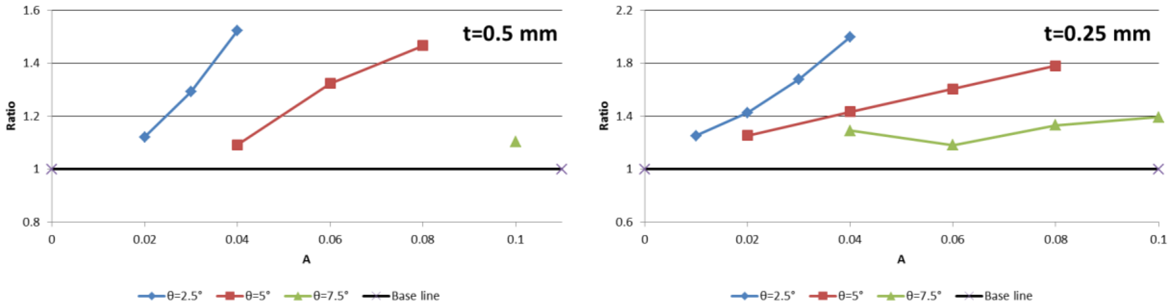

Figure 4.34. Plots of relationship between buckling to inverting force ratio and geometrical parameters.

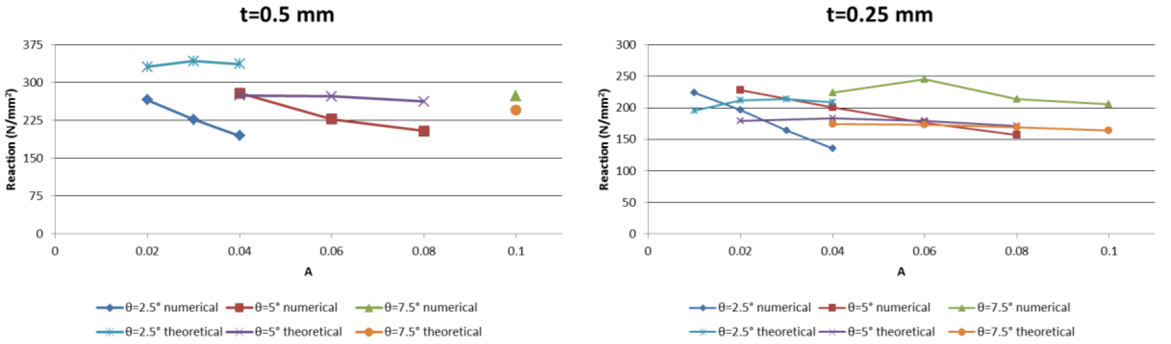

Figure 4.35. Comparison between numerical and theoretical results.

Table 4.9: Suggested range for each design parameter.

Parameter	D_{in}/t	θ	A/θ	μ
Suggested range	100~200	2.5°~5°	0.008~0.016	≤ 0.4

Similar to origami concave tubes, inversion of corrugated tubes also reaches the theoretical limit of energy absorption. Since corrugated tubes are providing almost largest buckling force (Ning and Pellegrino, 2013), and the reaction force of inversion process can approach this value. This implies that energy absorption of inversion process can reach the maximum value in theory by using the reaction force close to the buckling force to absorb energy.

4.6 Summary

The difficulty of tube inversion is caused by insufficient buckling force and exceedingly large inverting force. One main source of inverting force is from the circumferential stretch of the tube during inversion. The introduction of corrugation to the cross-section of the tube not only increases its stiffness in the axial direction, i.e., buckling force, but also reduces its stiffness in the radial direction, i.e., inverting force. In consequence, simply by changing the cross-section of the tube, inversion process can proceed much more reliably. This can permit practical friction coefficient and geometric imperfection in the environment of the experiment (strong friction and imperfection are not considered in this research), which has not been achieved or claimed before.

This chapter has presented several findings relating to tube inversion, and proposed to use a thin corrugated tube for inversion. This new setting is more reliable and allows frictional contact as well as geometric imperfection. It was first illustrated that thinner tubes are more likely to be inverted in theory, since the load needed for inversion decreases faster with reduction of wall thickness than the buckling load of the tube. However, thinner circular tubes are more sensitive to imperfection. This largely decreases their buckling force in practice. The introduction of corrugation into cross-section not only increases the practical buckling force (per area), but also decreases the load (per area) needed for inversion due to its less need for circumferential stretch. In consequence, the thin corrugated tube can be inverted reliably with reasonable frictional contact and imperfection, which has not been claimed or achieved before. This improvement shall largely extend the application of tube inversion mechanism.

Numerical simulations and experiments were carried out, and they proved the validity of this idea. A theoretical model was developed for a quick estimation of the reaction force of corrugated tube inversion. A parametric study was conducted, and provides a preferable range for each design parameter. A preliminary future design of corrugated tubes inversion can rely on the information provided by the theoretical model and the preferable range of parameters.

Chapter 5 Energy Absorption of Origami Beams and Arches

To achieve sustainable bending resistance for thin-walled open-section beams, structural depth of the beam during large deformation needs to be maintained. In this chapter, new designs for thin-walled open-section beams and arches are proposed, which can overcome this problem of reduction of structural height in large deformation associated with the existing beams or arches. All these new beams and arches can be created by folding a thin-walled sheet material using particular origami patterns. The design of origami beams is given first in this chapter. Extensive numerical simulations of a conventional beam and origami beams are conducted afterward. Small scale experiments are carried out. Further development of origami beams into panels, arches, and shell are proposed and preliminarily examined.

5.1 Geometry of Origami Beams

The essential idea of this improvement is by changing the geometry to: in one hand replace the traditional uniform cross-sectional beam by several longitudinally repetitive modules for more sustainable bending resistance during large deformation; and in the other hand design those modules with good ability to maintain their structural depth during large deformation. The geometric solution which satisfies these is presented as follows.

The origami pattern shown in Figure 5.1(a) consists of a set of mountain and valley creases, represented by solid and dash lines respectively. It is a rigid origami pattern, i.e., continuous folding can be carried out by folding along the creases without stretching the sheet, as Figure

5.1(b) shows. A straight beam can be formed once faces A and B (noted in Figure 5.1(a)) are met and welded together, shown in Figure 5.2(a). For clearance, the part facing up in Figure 5.2(a) is noted as the *top face*, which is designed to take compression, and the part facing down, which is designed to resist tension, is named as the *bottom webs*, shown in Figure 5.2 (a). The beam created in this way is developable, i.e., it can be made by bending a metal sheet without stretching it.

The geometry of this beam is defined by seven independent parameters. α is the pattern angle. a, b, c and d are dimensions, and all of which are given in Figure 5.1(a). m_b and n_b are the numbers of units (one of the units is pointed out in Figure 5.2 (a) and (b)) in lateral and longitudinal directions of the beam, respectively. Beam in Figure 5.2(a) has 4 lateral units ($m_b = 4$), while the pattern and beam in Figure 5.1(a) and (b) have 2 lateral units ($m_b = 2$). A portion of the completed beam with 2 lateral units ($m_b = 2$) folded from an aluminium sheet is shown in Figure 5.2 (c).

Geometrically, it can be found that the angle between top surface and horizontal plane, shown in Figure 5.2 (a) and (b), is

$$\theta = \arcsin(\tan\alpha) \ . \tag{30}$$

Other geometric parameters shown in Figure 5.1(a) are

$$g = 2a\sin\alpha \ , \tag{31}$$

and

$$b_1 = b - g \ . \tag{32}$$

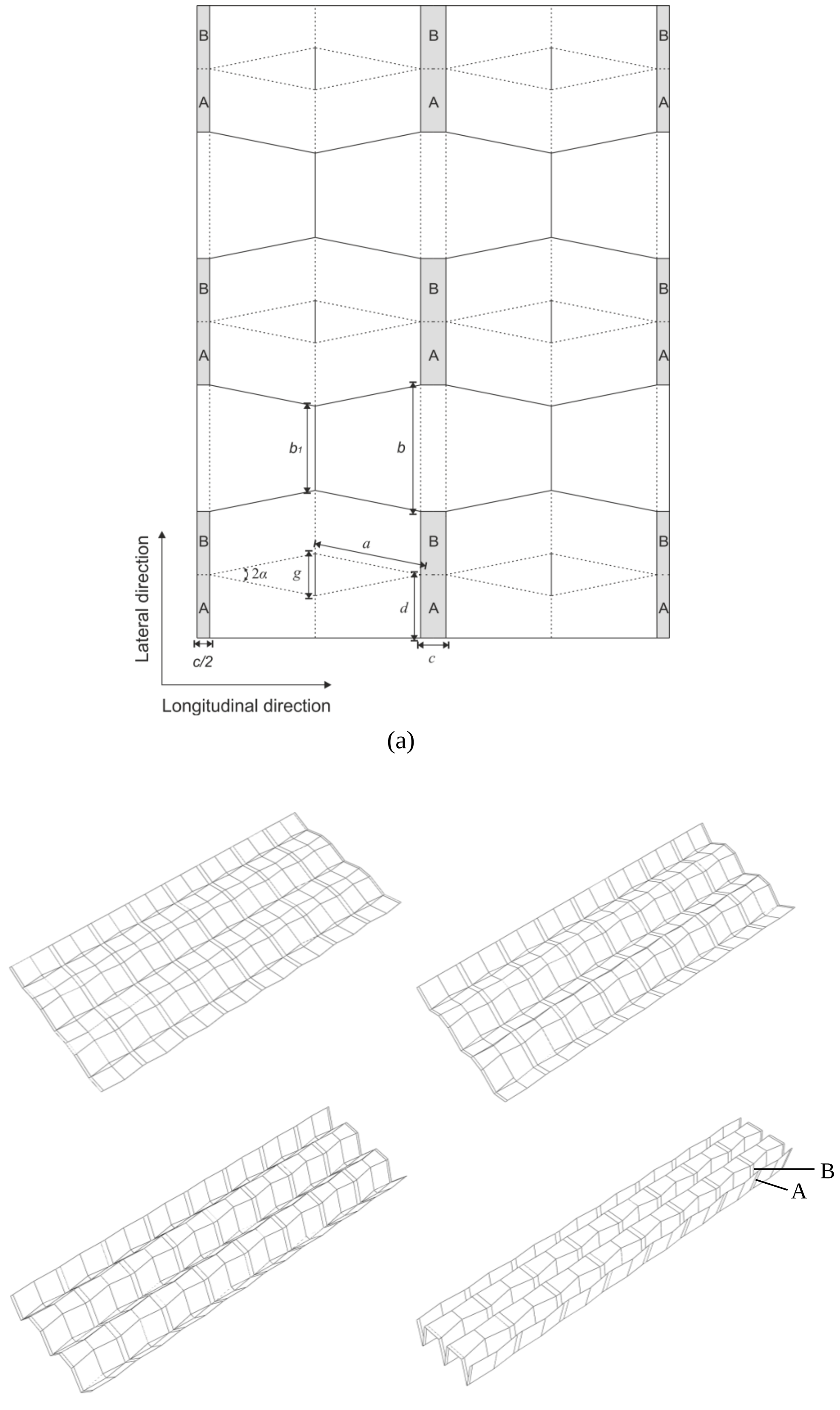

(a)

(b)

Figure 5.1. The design of origami beams: (a) a portion of the origami folding pattern on a sheet material, solid and dash lines represent mountain and valley creases, respectively; (b) gradual folding schematic diagram;

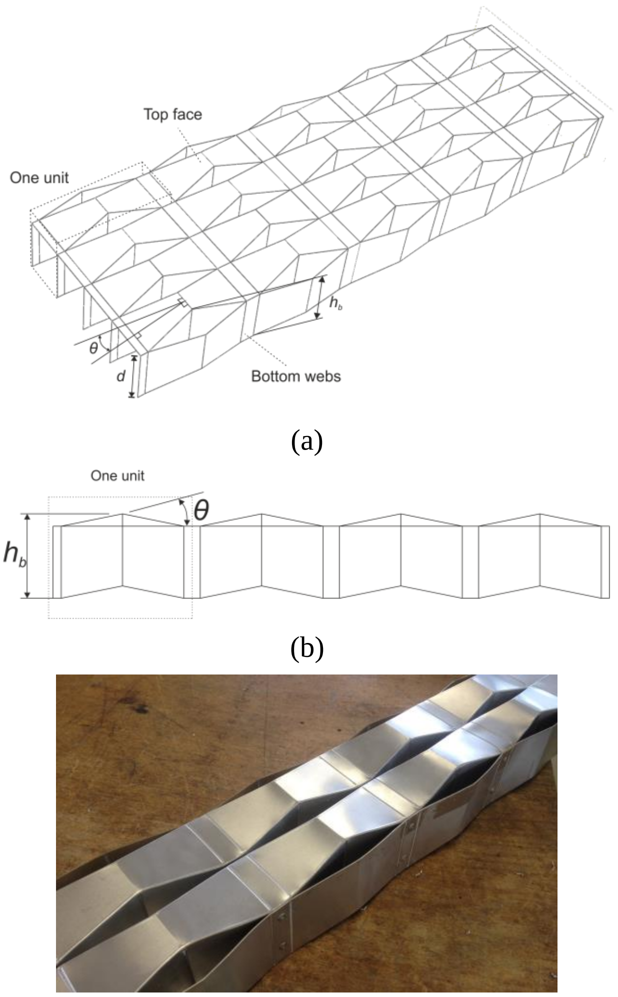

(a)

(b)

(c)

Figure 5.2 (a) The beam obtained from folding the sheet, and parts A and B are bonded together; (b) side view of the design; and (c) an aluminium model.

The overall length of the beam

$$L = n_b\left(2a\cos\alpha\cos\theta + c\right), \tag{33}$$

the width of the beam is

$$W = m_b b, \tag{34}$$

the overall height, shown in Figure 5.2 (a) and (b), is

$$h_b = d + a\cos\alpha\cos\theta, \tag{35}$$

and the surface area of the beam is

$$A_1 = n_b\left(2a\cos\alpha + c\right)\left[m_b\left(b+2d\right)+2d\right]. \tag{36}$$

One unit of the beam is noted in Figure 5.2(a) and (b). Repetitive units can be observed from the geometry of this origami beam, and this feature aims at distributing deformation into multiple units for more sustainable bending response. The top face of the beam is designed as compression side, which has a zigzag shape, shown in Figure 5.1(d). Since the valley parts of zigzag shape are welded together, the top face of the beam can only be squeezed up instead of crushed down, demonstrated in Figure 5.3 where one unit gets bent. This cooperation of origami folding and spot-welding shall maintain the structural depth of the beam for more constant reaction response. Numerical simulations were carried out for validation of this design in next section.

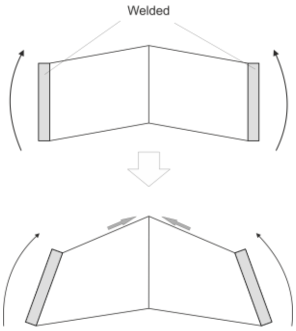

Figure 5.3. Side view of working mechanism of one unit.

5.2 Numerical Simulations of Origami Beams

In this section, a series of numerical simulations were run to demonstrate that origami beams have significantly higher SEA and lower load uniformity than those of a typical conventional beam.

5.2.1 Setting of Comparison and Numerical Simulation

The origami beam is designed for absorbing impact energy, which can be widely used as automobile frames, guardrails, structures in mining, etc.. Specifically, in this chapter, the effectiveness of the origami beam was evaluated by comparing it against a commercial bumper beam, shown in Figure 5.4. The cross section of this bumper beam is shown in Figure 5.4(b), and it was simplified as a straight beam in the simulation. The specific energy absorption (SEA) and load uniformity (LU) were used to evaluate their energy absorbing performance.

(a) (b)

Figure 5.4. (a) A commercial bumper beam and (b) its cross-section.

Material that beams used was 304 stainless steel, and its stress-strain curve is shown in Figure 5.5. Material properties are as follows. Density $\rho = 8030$ kg/m^3, Young's Modulus E = 193 GPa, Poisson's ratio $\nu = 0.3$, yield stress σ_y = 241.3 MPa, ultimate stress and strain σ_u = 679.6 MPa, ε_u = 55.8%, and the frictional coefficient $\mu = 0.25$ (Ma and You, 2013b, Ma and You, 2013a, Gattas and You, 2014, Gattas and You, 2015). Abaqus/Explicit (Abaqus, 2013) was used to simulate the performance of the beams under quasi-static three-point bending. Folding effect and strength of the welding were not considered in the simulation.

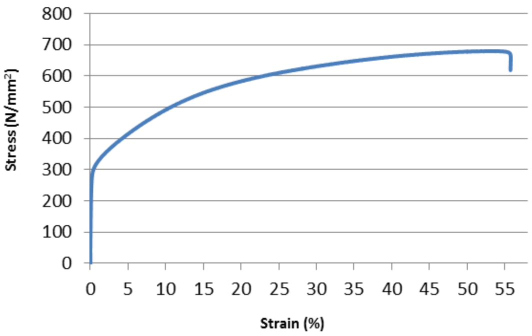

Figure 5.5. Stress strain curve of 304 stainless steel.

Commercial bumper beam, B_0, had cross-section shown in Figure 5.4(b), the material thickness of 2 mm, and length of 1000 mm. A series of origami beams, 20 of them in all, had an identical material thickness, span, and cross section height with those of B_0. The amount of material used for each origami beam was less than conventional beam B_0. All origami beam models and their corresponding parameters are listed in Table 5.1. Simulation results and comparisons are presented in the same table and explained in detail in Section 5.2.2. All origami beam models had $m_b = 1$, $t = 2$ mm, $c = 10$ mm, $d = 55$ mm, and $L = 1000$ mm. The value of α changes from 1.6° to 6.3° in the table, and this pattern angle dominates the inclination of each face. The value of b varies from 15 to 35, and it determines the width of the beam. From previous preliminary research, lower value of α and b gives higher energy absorption but less stability. Other parameters affect the performance of the beam less dramatically than α and b. The geometry of B_0 and B_{1_1} are shown in Figure 5.6. All beams were put under quasi-static three-point bending, which was performed by one moving rigid cylinder while two ends of the beam were simply supported, shown in Figure 5.7. The rigid cylinder had a radius of 50 mm, crushing speed of 5 m/s, and total displacement of 350 mm. Convergence tests with respect to mesh density and analysis time were conducted prior to the analysis. The ratio of artificial energy to internal energy was below 5%, and the ratio of kinetic energy to internal energy was also below 5% as recommended by Abaqus/Explicit (Abaqus, 2013).

Table 5.1: Information of all beams simulated.

Model	n_b	α (°)	b (mm)	Weight (kg)	Unstable failure	LU	LU reduction (%)	SEA (kJ/kg)	SEA increase (%)
B_0	-	-	-	4.15	-	1.5	-	639.5	-
B_{1_1}	10	6.3	35	4.12		1.28	14.7	786.6	23.0
B_{1_2}	10	6.3	30	4.04		1.31	12.7	815.5	27.5
B_{1_3}	10	6.3	25	3.96		1.24	17.3	852.5	33.3
B_{1_4}	10	6.3	20	3.88		1.19	20.7	856.3	33.9
B_{1_5}	10	6.3	15	3.80	Unstable	1.37	8.67	494.3	-22.7
B_{1_6}	12	6.3	25	3.96		1.19	20.7	831.7	30.1
B_{1_7}	12	6.3	20	3.88		1.24	17.3	874.5	36.7
B_{1_8}	14	6.3	25	3.96	Unstable	1.20	20.0	617.2	-3.49
B_{1_9}	14	6.3	20	3.87	Unstable	1.25	16.7	578.4	-9.55
B_{2_1}	10	3.8	35	4.10		1.19	20.7	801.3	25.3
B_{2_2}	10	3.8	30	4.02		1.24	17.3	819.4	28.1
B_{2_3}	10	3.8	25	3.94		1.21	19.3	854.5	33.6
B_{2_4}	10	3.8	20	3.86		1.20	20.0	871.4	36.3
B_{2_5}	10	3.8	15	3.78	Unstable	1.42	5.33	485.1	-24.1
B_{2_6}	12	3.8	25	3.94	Unstable	1.17	22.0	631.1	-1.31
B_{2_7}	12	3.8	20	3.86		1.20	20.0	895.5	40.0
B_{2_8}	14	3.8	25	3.94	Unstable	1.27	15.3	607.6	-4.99
B_{2_9}	14	3.8	20	3.86	Unstable	1.06	29.3	706.3	10.4
B_{3_1}	10	1.6	30	4.02	Unstable	1.20	20.0	686.6	7.36
B_{3_2}	10	1.6	20	3.86	Unstable	1.17	22.0	696.9	8.98

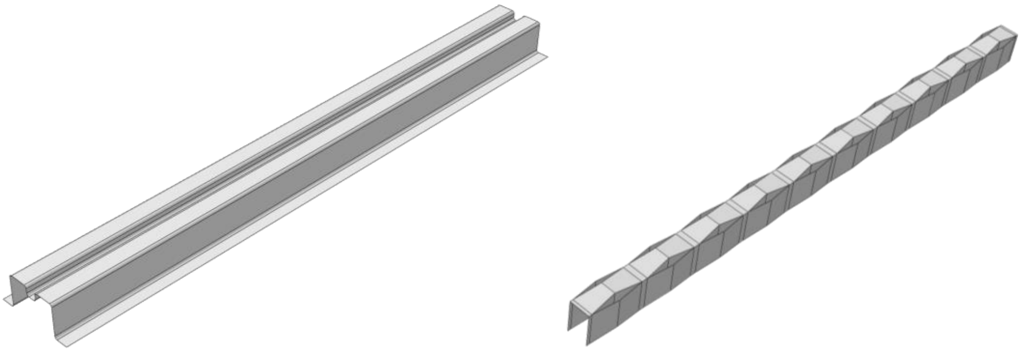

(a) (b)

Figure 5.6. Geometry of (a) B_0 and (b) B_{1_1}.

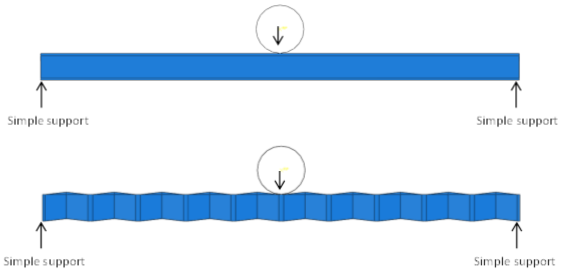

Figure 5.7. Setting of three-point bending.

5.2.2 Simulation of Beams under Three-Point Bending

Numerical results of all 21 beam models are presented in Table 5.1, which contains information of failure mechanism of origami beams, and also their comparison to the conventional beam in terms of specific energy absorption (calculated as internal energy divided by mass) and load uniformity. The conventional beam B_0, which was chosen as a benchmark to assess the improvement of the origami beams, was analysed. Deformation of B_0 provided by numerical simulation is shown in Figure 5.8. It shows the deformation of the beam from three different angles: side view, front view, and inclined view (rigid rod was removed). The material in the middle of the beam was squeezed downwards, and a localised hinge was formed while the rest part of the beam remained non-deformed. In consequence, obvious structural depth reduction occurred in the middle of the beam (Figure 5.8), which caused a significant decrease of stiffness in the later stage of bending, shown in Figure 5.10.

Deformation of origami beam B_{1_1} is shown in Figure 5.9. Two units at top face were squeezed up, and correspondingly the structural depth was increased. This indicated that the stiffness of the beam could be well maintained in large deformation, shown in Figure 5.10. With appropriate parameters, webs of origami beams could be widened during deformation to prevent lateral buckling, shown in the front view of Figure 5.9. All other origami beams which failed stably showed similar deformation to B_{1_1}. Reaction curves of B_0 and B_{1_1} are presented in Figure 5.10, which shows B_{1_1} achieved more constant reaction force than B_0. The fluctuation of reaction forces at the beginning was caused by dynamic bouncing effect when the rigid cylinder hit the beam initially.

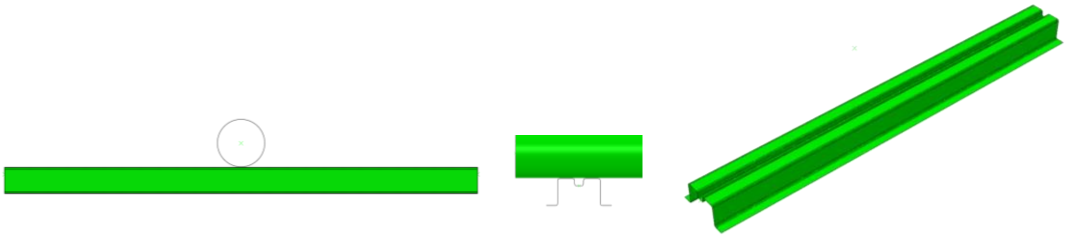

Displacement=0 mm

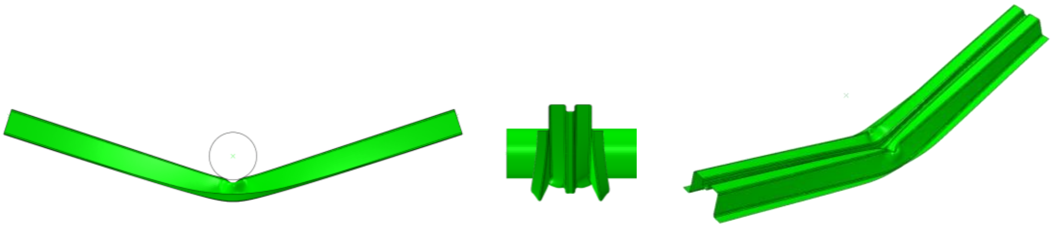

Displacement=150 mm

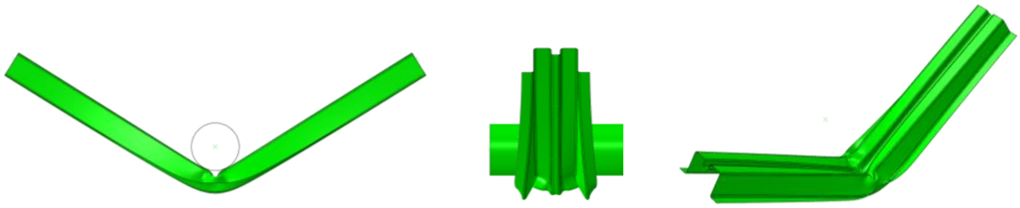

Displacement=250 mm

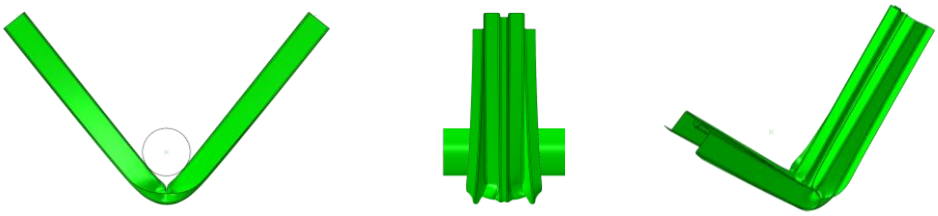

Displacement=350 mm

Figure 5.8. Deformation of B_0.

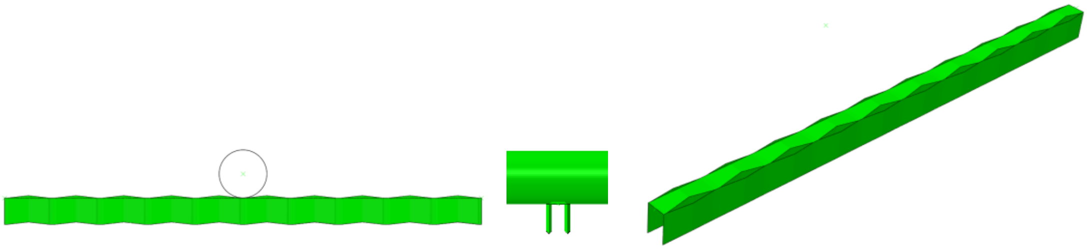

Displacement=0 mm

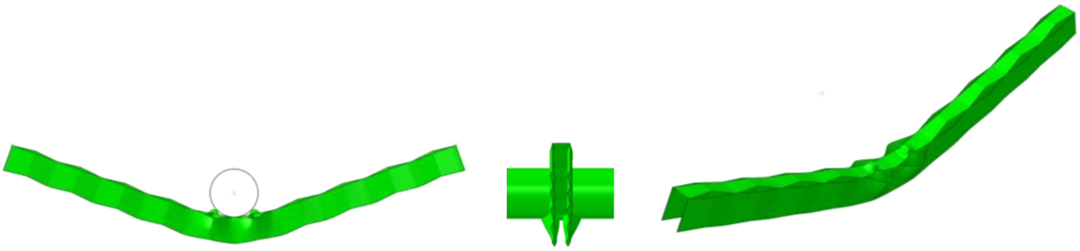

Displacement=150 mm

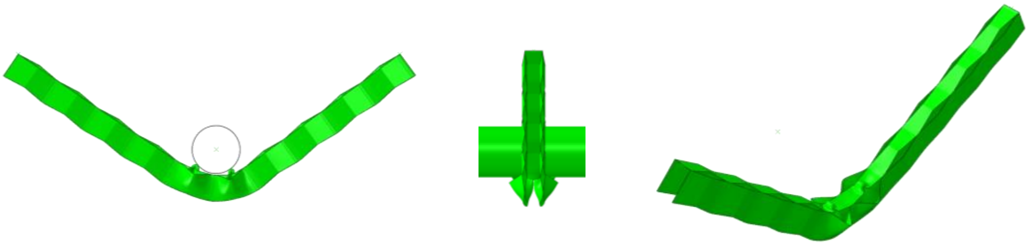

Displacement=250 mm

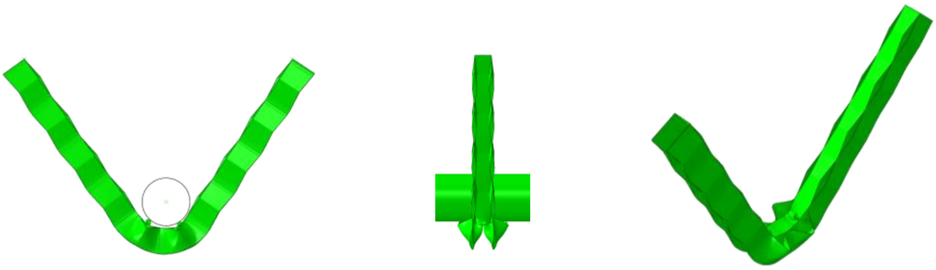

Displacement=350 mm

(b)

Figure 5.9. Deformation of B_{1_1}.

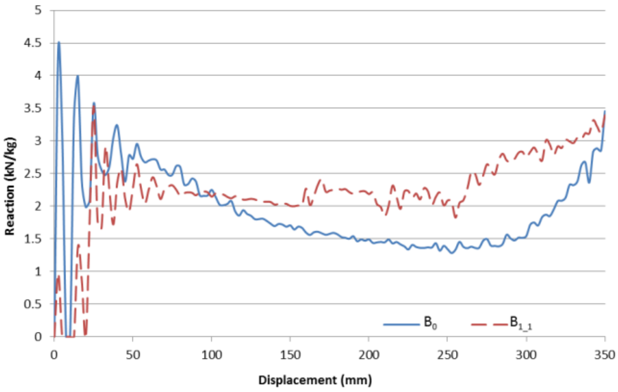

Figure 5.10. Reaction forces of B_0 and B_{1_1}.

Table 5.1 shows that unstable failure mechanism (lateral torsional buckling of webs) could occur to origami beams when the width of web or beam is too small and led to low energy absorption. Deformation of B_{3_1} is shown in Figure 5.11. It shows that material in top face bulged out at first, while webs of the beam swayed laterally when bent further. This caused reduction of stiffness in the later stage. All other origami beams listed in Table 5.1 which failed unstably deformed in a similar way and caused relatively low energy absorption.

Displacement=0 mm

Displacement=150 mm

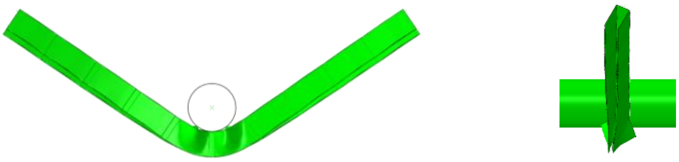

Displacement=250 mm

Figure 5.11. Side and frontal view of deformation of B_{3_1}.

From Table 5.1, origami beams (except for those failed unstably) achieved 12.7%-20.7% lower load uniformity and 23.0%-40.0% higher specific energy absorption (SEA) than those of a typical conventional open-section beam B_0.

A smaller value of b and large value of α can increase SEA of origami beams, but also decrease the stability of the structure. Instable failure of origami beams (Figure 5.11) suffer a huge drop of SEA. In order to avoid that, appropriate ranges of parameters for origami beams are proposed in Table 5.2 with predetermination of $m_b = 1$, $t = 2$ mm, $c = 10$ mm, $d = 55$ mm, and $L = 1000$ mm. Scalability has been checked, and these parameter ranges can be used in different applications and scales. Within the table, the beam B_{1_3} has $\alpha = 6.3°$ and $b = 25$ mm is most optimized, while the beam B_{1_1} has $\alpha = 6.3°$ and $b = 35$ mm is most conservative. Simulation results of origami beams with different settings and scales can be found from (Li, 2014).

Table 5.2: Appropriate ranges of parameters

Parameters	n	α (°)	b (mm)
Range	10	3.8-6.3	25-35

5.3 Experimental Study and Its Comparison with Numerical Results

This section is to in one hand demonstrate the function of origami beam and its merits to conventional beam with experiments, and in the other hand to validate numerical modelling technique by its comparison with experimental results.

5.3.1 Experiment Setting

Small-scale prototypes of B_0 and B_{1_1} were made by using the same amount of material, which are noted as B_{0_exp} and $B_{1\_1\_exp}$ respectively. Dimensions of B_{0_exp} and $B_{1\_1\_exp}$ were scaled down to 1/5, except for thickness to 1/10 of B_0 and B_{1_1}. Scale ratio of thickness was different due to material availability, and manufacturing and loading feasibility.

All beams were constructed from 0.2 mm thick aluminium 1100-0. Tensile tests were conducted on the material, which gave the stress-strain curve shown in Figure 5.12. Beams were built by gradual stamping of sheet material with 3D printed male and female moulds, shown in Figure 5.13. Similar stamping technique was used by (Gattas and You, 2015, Gattas and You, 2014). Aluminium sheet was put into shallow moulds first and compressed by a heavy load, and then compressed by deeper moulds. In this way, beams can be folded into shape step by step. The material had good ductility, and the beam stayed in shape after formation with no observable rebounding. In consequence, residual stress from manufacturing process was very small comparing to the stress experienced in the crushing process. Parts which needed to be welded in origami beam were glued by Super Glue. Since direct welding of a thin aluminium sheet can be difficult and this glue is significantly harder than aluminium used, this way of connection was employed to replace spot-welding. Two ends of beams were made sufficiently rigid by wrapping and gluing with additional material, which is noted in Figure 5.13(b). Beams were put under Instron 5582 for three-point bending tests, shown in Figure 5.14. The span between supports was 100 mm, the rigid rod at the centre had a radius of 10 mm, and rods at support had a radius of 7.5 mm. The loading speed was 5 mm/min, and total displacement was 40 mm. In total, 3 specimens were prepared for each type of the beam, and all of them are presented in Figure 5.13(b).

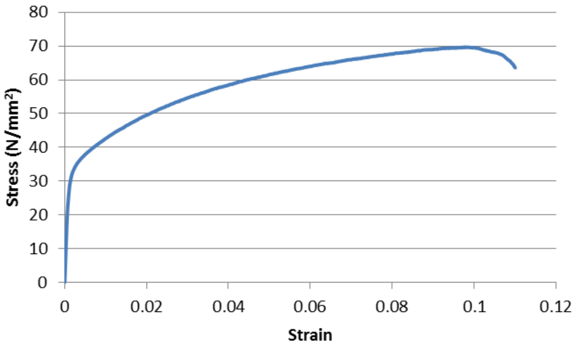

Figure 5.12. Stress strain curve of aluminium 1100-0.

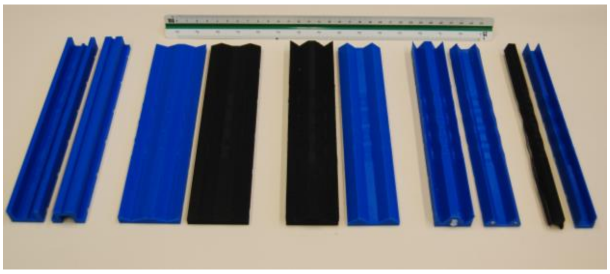

(a)

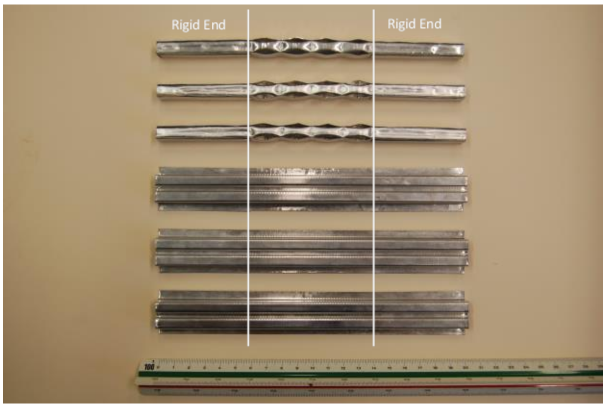

(b)

Figure 5.13. Manufacturing by (a) a series of moulds and forming (b) 6 beam prototypes.

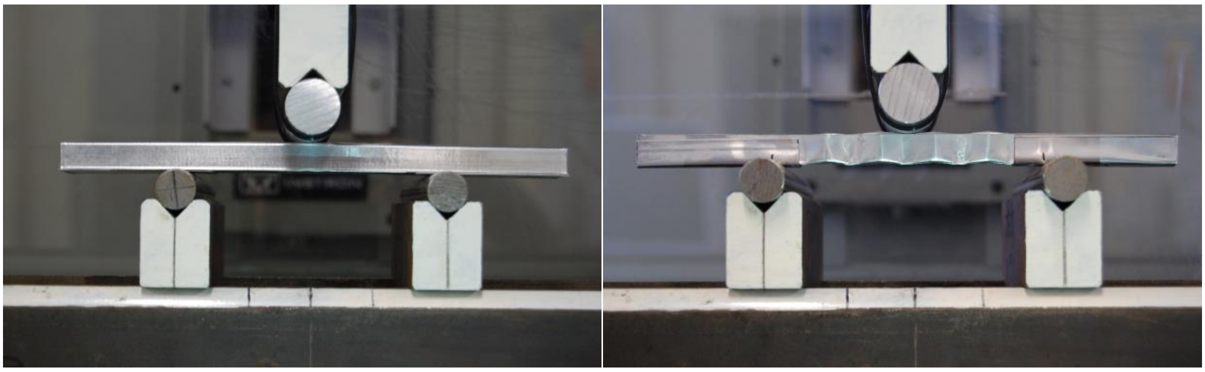

(a) (b)

Figure 5.14. Setting of three point bending of (a) B_{0_exp} and (b) $B_{1\_1\_exp}$ in Instron.

5.3.2 Modelling of Experimental Beams

Numerical models of B_{0_exp} and $B_{1\_1\_exp}$, shown in Figure 5.15, were made with the same technique of Section 5.2. Two ends were stiffened with more material as in the experiment. 19088 S4R elements were used for B_{0_exp}, and 22960 S4R and 32 S3 elements for $B_{1\_1\_exp}$. The setting of loading and supports were the same as the experiment, which is shown in Figure 5.16. Loading speed was 1 m/s, and kinematic energy was well below 5% of total energy.

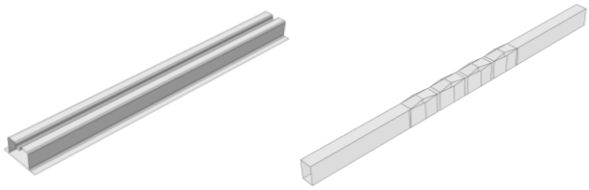

Figure 5.15. Geometries of numerical models of B_{0_exp} and $B_{1\_1\_exp}$.

Figure 5.16. Loading setting in numerical simulation.

5.3.3 Experimental and Numerical Results

Six experiments and two simulations were finished as described in previous subsections. One set of experimental and simulated deformations of B_{0_exp} are presented in Figure 5.17 with respective displacements of 0 mm, 20 mm, and 40 mm. Three experiments of B_{0_exp} were carried out and showed identical deformation, and only one experiment is presented in Figure 5.17(a). Reaction curves of three experiments are given in Figure 5.19(a), and good consistency can be seen. No obvious discrepancy can be noticed between experimental and simulated deformations in Figure 5.17. Reaction curves from experiment (average of three curves) and numerical simulation are shown in Figure 5.20(a), and provide a generally good match between the two, except for slight fluctuation in numerical simulation. This fluctuation was probably due to some numerical noise and the dynamic bouncing effect. Significant structural depth reduction could be observed from B_{0_exp} in both of experiment and simulation. This is corresponding to the huge decrease of stiffness in the later stage of deformation, shown in Figure 5.19(a) and Figure 5.20(a).

One set of experimental and numerical deformations of $B_{1\_1\_exp}$ are presented in Figure 5.18. In comparison with B_{0_exp}, the top face of $B_{1\_1\_exp}$ bulged out instead of crushed down in experiment and simulation. In total, three experiments were done and showed similar failure modes. $B_{1\_1\_exp}$ maintained its section height in large deformation. This demonstrated the designed merits of origami beams. Experimental reaction forces of $B_{1\_1\_exp}$ are shown in Figure 5.19(b). It shows some phase shift and magnitude variation to each other, which was mainly due to its highly imperfect manufacturing method. The performances of $B_{1\_1\_exp}$ still demonstrated good repeatability in terms of deformation and reaction curve, and this suggested that the manufacturing method was acceptable. Reaction curves from experiment (average of three curves) and numerical simulation of $B_{1\_1\_exp}$ are shown in Figure 5.20(b), and numerical simulation gave overall higher reaction force than experiments. Experimental initial peak force of origami beam was lower than simulation, which was likely due to its highly imperfect initial geometry. The lower overall stiffness of experiments to simulation could be caused by the lack of consideration of the strength of Super Glue in numerical analysis, since the sound of the splitting of Super Glue could be heard in the later stage of loading during experiments. Fluctuation of numerically simulated reaction forces was not reflecting the real behaviour of beams as it should be relatively smooth in most of the region. This problem could be caused by numerical noise introduced in sliding contact and dynamic bouncing effect as loading speed in the simulation was higher than the experiment.

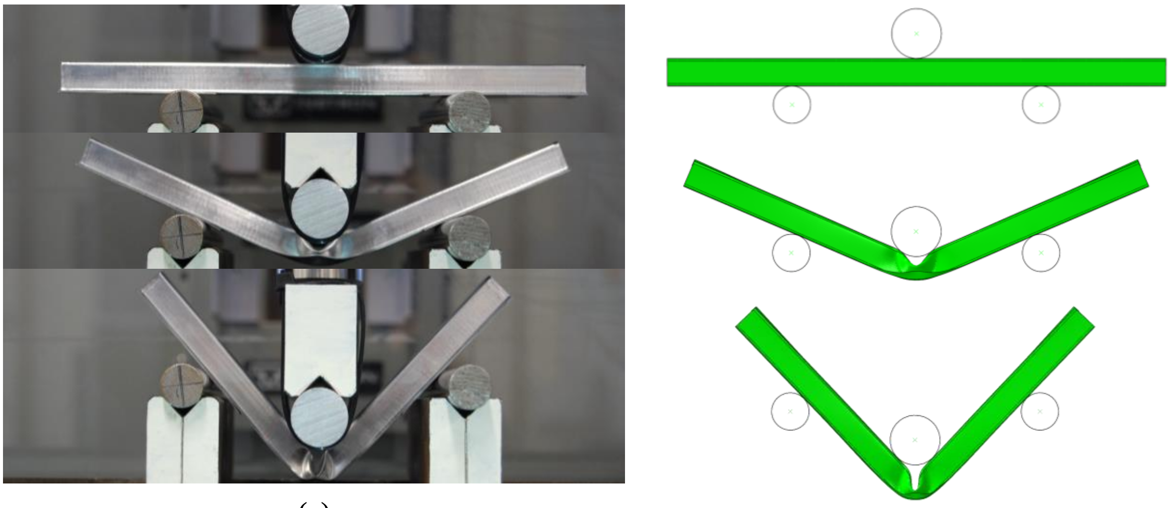

(a) (b)

Figure 5.17. (a) Experimental and (b) numerical deformation of B_{0_exp}.

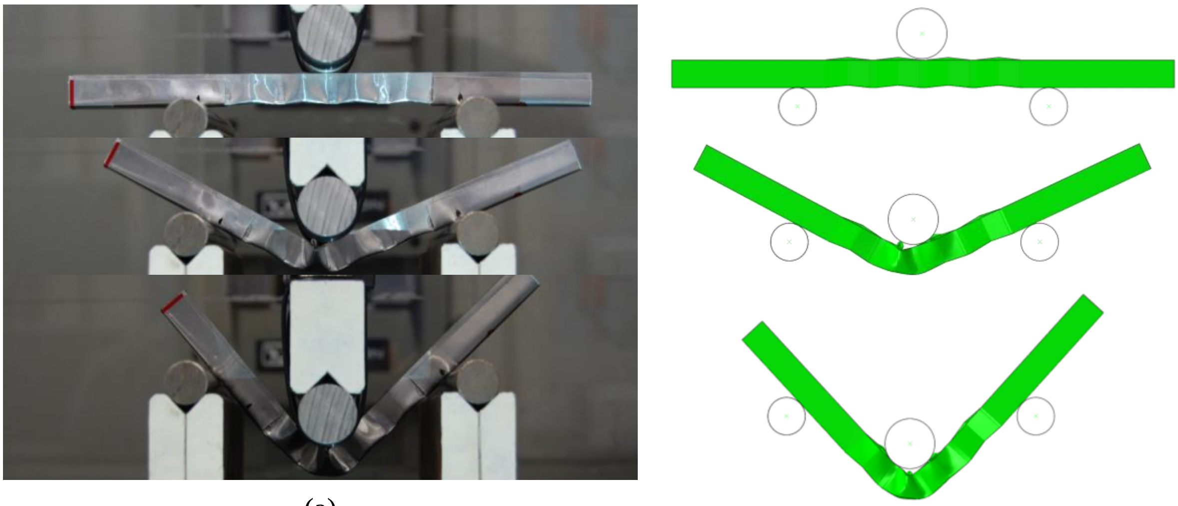

(a) (b)

Figure 5.18. (a) Experimental and (b) numerical deformations of $B_{1\_1\_exp}$.

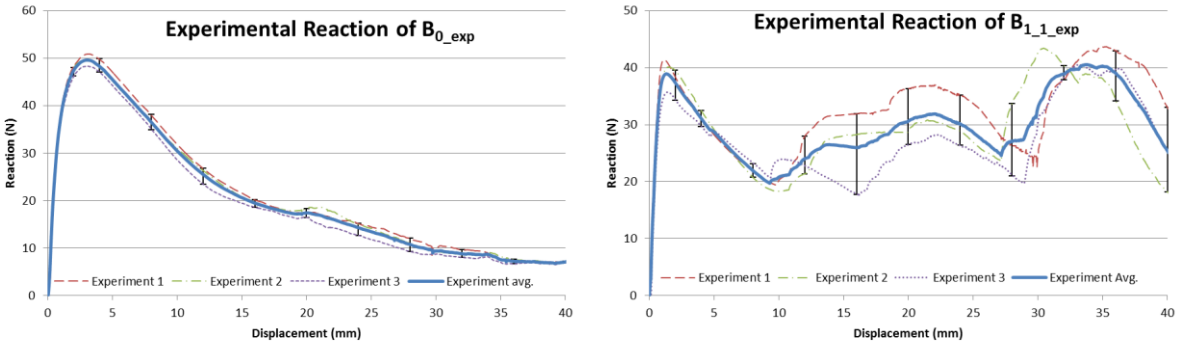

(a) (b)

Figure 5.19. Experimental reaction forces of (a) B_{0_exp} and (b) $B_{1\_1\_exp}$.

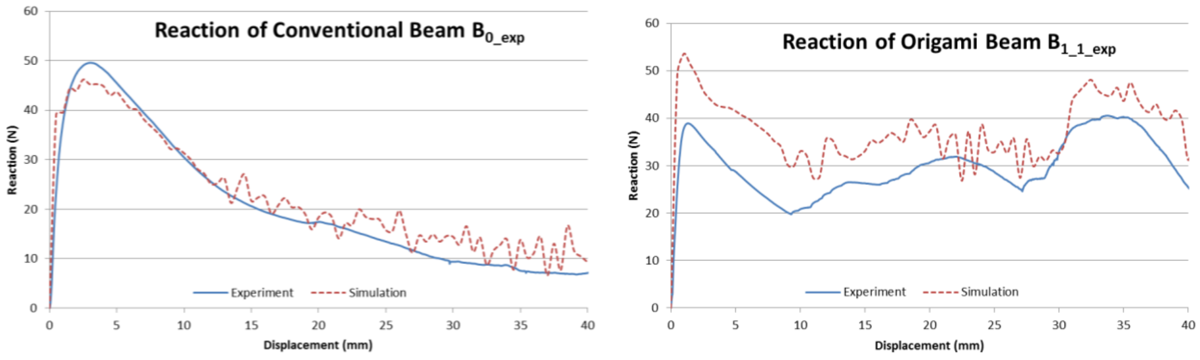

(a) (b)

Figure 5.20. Comparison between experiments and numerical simulations of (a) B_{0_exp} and (b) $B_{1\_1\_exp}$.

Direct comparison of averaged experimental reaction forces of a conventional beam and the origami beam is shown in Figure 5.21, and it shows that origami beam $B_{1\_1\_exp}$ gave more constant reaction force and overall significantly higher energy absorption. Improvement of origami beam $B_{1\_1\_exp}$ to conventional beam B_{0_exp} is shown in Table 5.3. It shows that 40%-60% increase of SEA and 30%-40% decrease of LU were achieved by origami beam.

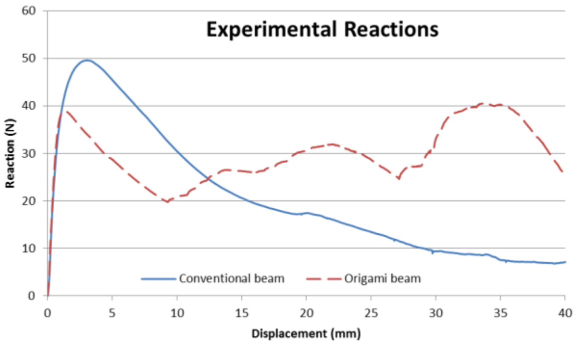

Figure 5.21. Comparison of experimental reaction forces of B_{0_exp} and $B_{1\_1\_exp}$.

Table 5.3: Results of experimental and numerical analysis.

	Mean crush force (N)		Load uniformity		Increase of Mean crush force		Decrease of load uniformity	
Types	Exp.	FEA	Exp.	FEA	Exp.	FEA	Exp.	FEA
B_{0_exp}	20.65	22.38	2.40	2.07	-	-	-	-
B_{1_1exp}	29.61	37.31	1.37	1.44	43.40%	66.71%	42.98%	30.41%

In this section, improved performance of origami beam to the conventional beam was experimentally demonstrated. This experimentally proved that this idea can enable beams to provide more consistent bending resistance in large deformation. Numerical simulation technique used was validated by showing good correlation with experimental results.

5.4 Further Development of Origami Beams

As previous sections demonstrated, origami beams have desired failure mechanism which enables high energy absorption and low load uniformity. Similar failure mechanism can be also triggered in other forms of origami beams and panels. More related designs are presented and discussed in this section.

5.4.1 **Origami Panels**

Panels can be made when origami beam get repeated laterally. Let's set m_b of B_{1_3} as 2 and 4, and name them as $B_{1\_3\_2}$ and $B_{1\_3\_4}$ respectively, shown in Figure 5.22(a). It shows that wider origami beams or panels are formed. These structures can also be manufactured from one single sheet material according to the folding pattern shown in Figure 5.1(a), except for more repetition in the lateral direction in origami pattern. One-way origami panels made in this method can work in the same way as origami beams. Numerical simulations were done as in Section 5.2, and deformations are shown in Figure 5.22(b). The material in the top face also bulged out and demonstrated same working mechanism as origami beams studied in previous sections. Specific energy absorption (SEA) of B_{1_3}, $B_{1\_3\_2}$, and $B_{1\_3\_4}$ were 852.5, 981.9, and 1120.5 kJ/kg respectively. $B_{1\_3\_2}$ and $B_{1\_3\_4}$ showed same failure mechanism as B_{1_3}, while higher SEA. It was observed generally that larger m_b contributed to significantly larger SEA.

This is because the material at two lateral sides of the beam/panel absorbs less energy than the material in the middle, and larger m_b reduces the proportion of material at sides, which increases SEA. A larger value of m_b also increases the stability of the beam/panel due to its increase in overall width, which might enable further optimization. The increase of m_b can extend origami beams into panels, which might suit different applications.

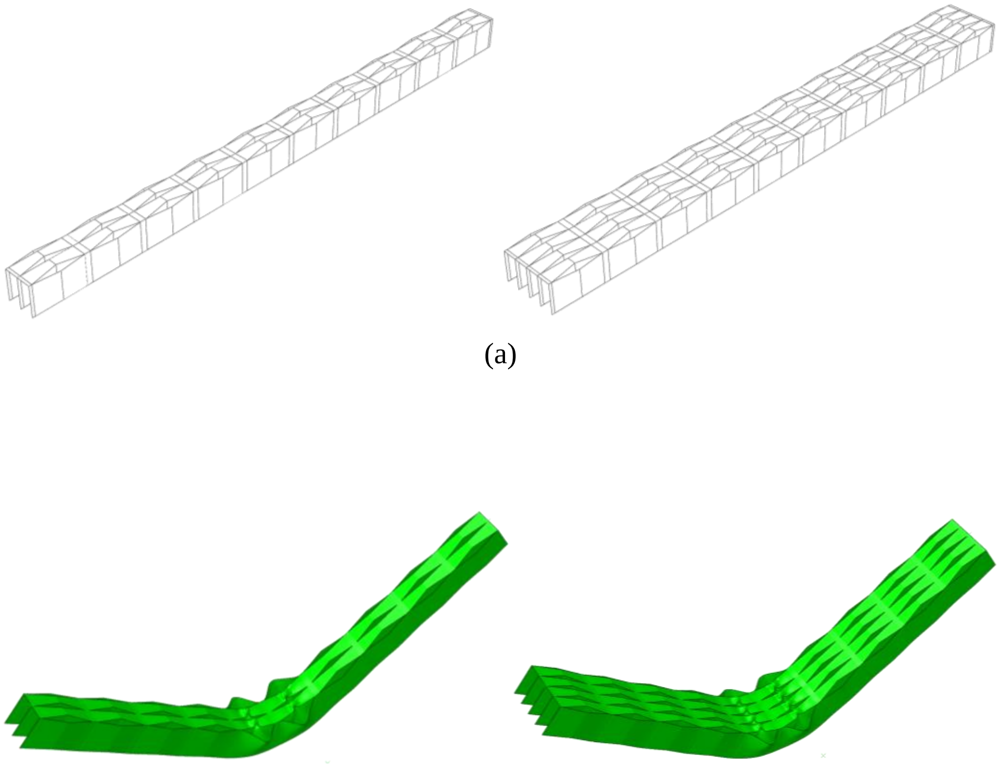

(a)

(b)

Figure 5.22. (a) Geometries of origami beams/panels with m_b = 2 and 4, and (b) their corresponding simulated deformations.

5.4.2 Face-switcher

The top face of the beam is designed to resist compression and bottom webs for tension. However, there are situations that bending moment switches its sign within the beam, such as a continuous beam or clamped boundary condition. In consequence, the geometry of the origami beam needs to be switched upside down correspondingly within the beam, which leads to the design of a special structure named as *face-switcher*.

Its origami folding pattern and geometry are shown in Figure 5.23. A linear offset is introduced to the origami pattern so that it can achieve the flipping effect of the face-switcher. In the folding pattern shown in Figure 5.23(a), it starts with the same form as Figure 5.1(a) on its left side, and switches into a different form on the right side after going through face-swither in the middle part. The geometric function of this process can also be seen from Figure 5.23(b), in which the structure starts with the top face facing up on the left side, and ends with bottom webs facing up on the right side. A paper folded model is presented in Figure 5.23(c), and it shows that webs are facing up at its end. This design enables origami beams/panels to cope with different loading situations flexibly. The geometry of face-switcher is governed by two parameters α_s and a_s, which are noted in Figure 5.23(a). These two parameters shall satisfy

$$a_s = \frac{b}{2\sin\alpha_s}\,. \tag{37}$$

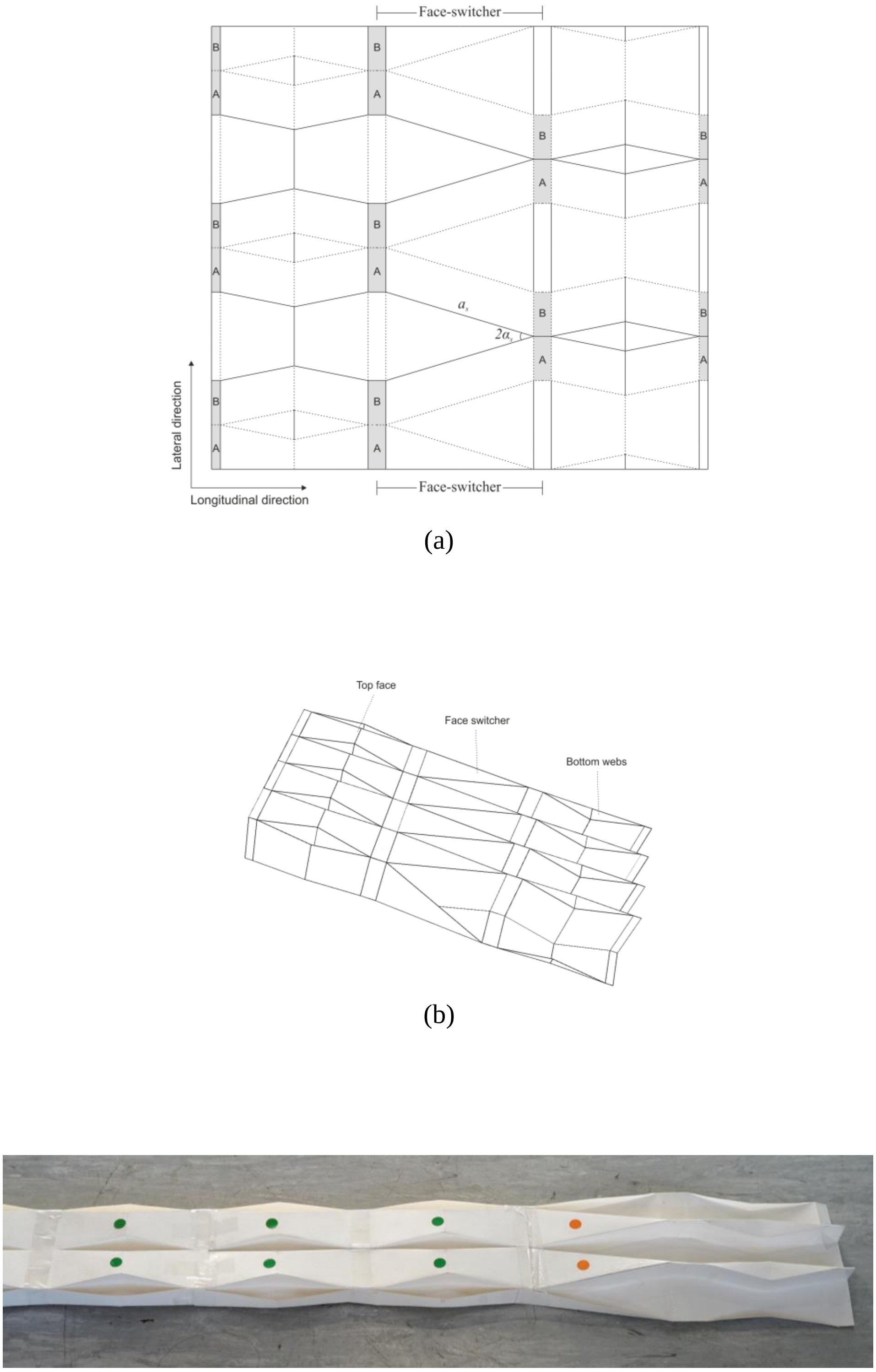

(a)

(b)

(c)

Figure 5.23. Design of face-switcher: (a) a portion of folding pattern; (b) geometry of face-switcher; and (c) a paper folded model.

The geometry of face-switcher enables origami beams/panels to be designed according to anticipated moment distribution. However, face-switcher is only applicable when $m_b \geq 2$ due to the geometrical constraint. Let's consider to add face-switcher with a_s=91.4 mm into $B_{1\_3\_2}$ and name it as $B_{1\_3\_2s}$, shown in Figure 5.24(a). It can be noticed that the geometry at the ends of the beam is different from the middle, and this beam can be folded out of one single sheet material. Now putting B_0, $B_{1\_3\_2}$, and $B_{1\_3\_2s}$ all under clamped boundary condition (allow lateral movement but no rotation at two ends) and loaded by a rigid cylinder as in Section 5.2. This boundary condition and loading caused different directions of the moment in the middle and at ends of the beam. Deformations of three beams are shown in Figure 5.24. Bottom webs at ends (connected to boundaries) of $B_{1\_3\_2}$ buckled laterally due to compression, and their stiffness was reduced afterward. In contrary to that, parts of $B_{1\_3\_2s}$ in both middle and ends experienced the same type of deformation, which could generate sustainable bending resistance in large deformation. Plots of reaction force are shown in Figure 5.25. The reaction force of $B_{1\_3\_2s}$ was significantly higher and more constant than the other two beams. Comparison of specific energy absorption (SEA) of B_0, $B_{1\_3\_2}$, and $B_{1\_3\_2s}$ are given in Table 5.4, which shows that $B_{1\_3\_2s}$ achieved significantly higher energy absorption than the other two. This demonstrated that design of face-switcher is effective in enabling origami beams or panels to cope with different loading scenarios, in order to maximize their energy absorbing capacity.

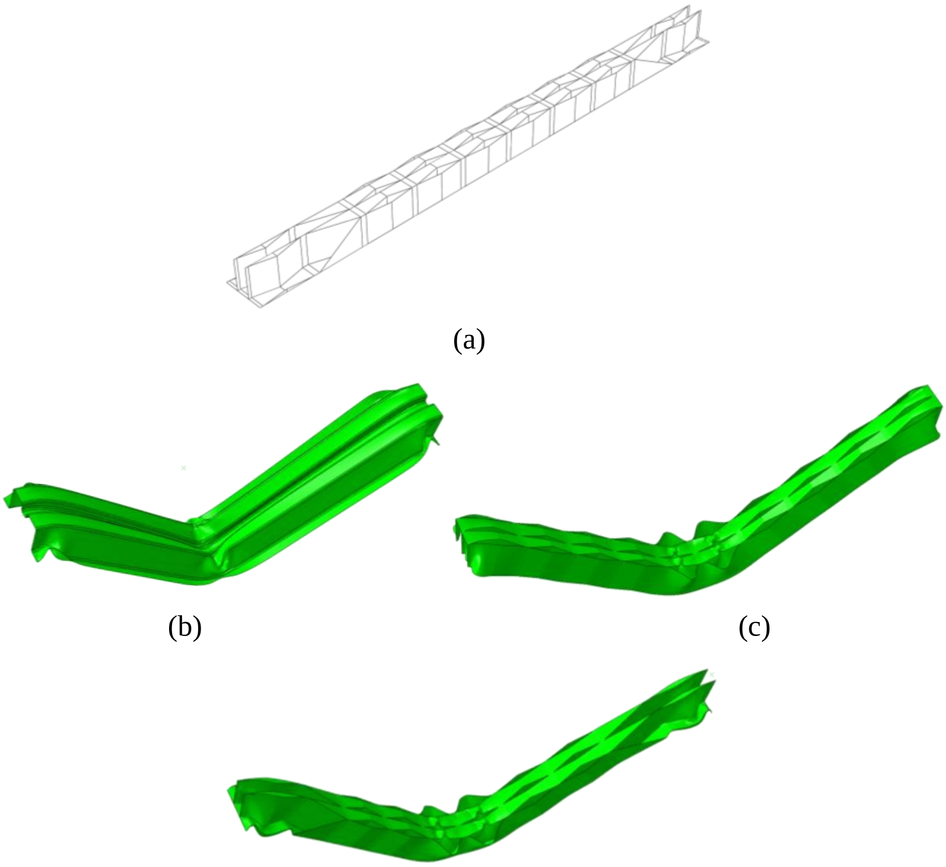

(a)

(b) (c)

(d)

Figure 5.24. (a) Geometry of $B_{1\_3\_2s}$, and simulated deformation of (b) B_0, (c) $B_{1\_3\_2}$, and (d) $B_{1\_3\_2s}$ with displacement of 250 mm.

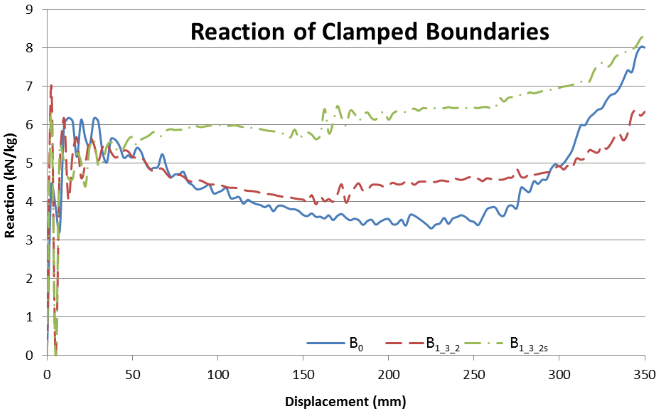

Figure 5.25. Reaction force plots.

Table 5.4: Performance of three beams.

Types	B_0	$B_{1\_3\_2}$	$B_{1\_3\_2s}$
SEA	1514.6	1602.3	2156.0
Increase of SEA	-	5.8%	42.3%

5.4.3 Two-way Bending Beam

Frontal view of the design of origami beam ($m_b = 2$) is given in Figure 5.26(a). This design has the top face to take compression and bottom webs to take tension effectively. However, if the loading direction is uncertain, then it will require the beam to be able to take compression and tension in both sides. Based on the same idea, two-way bending beam is developed. Its folding pattern is shown in Figure 5.26(b), and a beam can be made when A meets B and C meets D and welded together. Controlling parameters are noted in the folding pattern, and $e_t' = \frac{e_t}{2}$. Frontal view of its folded geometry is given in Figure 5.26(c), which shows that both top and bottom faces of two-way bending beam have similar geometry to the top face shown in Figure 5.26(a). The geometry of folded beam is given in Figure 5.27, in which (a) has same placement as in Figure 5.26(c), and it is named as *placement 1*. Beam in Figure 5.27(b) is orientated upside down which is named as *placement 2*. The difference of two placements is the opposition of the top and bottom sides of the beam. Both Figure 5.27(a) and (b) show similar geometries.

Geometric parameters of the beam are set as in Table 5.5. Overall depth, length, and mass of the beam are 55 mm, 1000 mm, and 6.77 kg. Numerical simulation with the same technique as previous ones was done by loading two-way bending beam with two different placements as presented in Figure 5.27(a) and (b) respectively. Beams were simply supported. Deformation and reaction force plots are given in Figure 5.28. Deformations of the middle part of both beams showed that material bulged outwards. Figure 5.28(c) shows that bending in both directions gave almost constant reaction responses. Sustainable reaction response was achieved by this design as same as previous origami beams. When more lateral units are added, it is expected to increase SEA of the structure, and the difference between responses of two placements shall decrease.

This design has much wider application. It might also be used as long struts to provide more sustainable reaction force in global buckling. However, two-way bending beam is more complicated due to its concave cross-section and costlier in manufacturing.

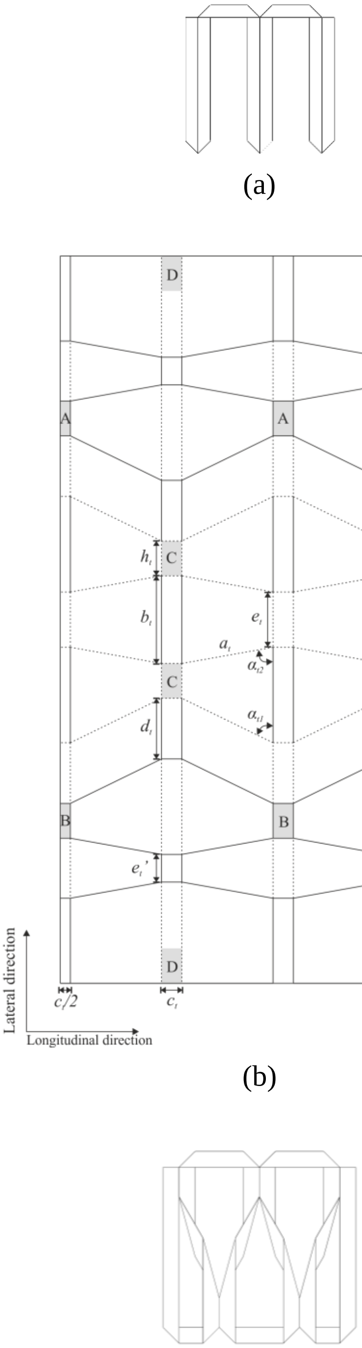

(a)

(b)

(c)

Figure 5.26. Design of two-way bending beam: (a) Frontal view of previous origami beam; (b) folding pattern of two-way bending beam; and (c) frontal view of folded two-way bending beam.

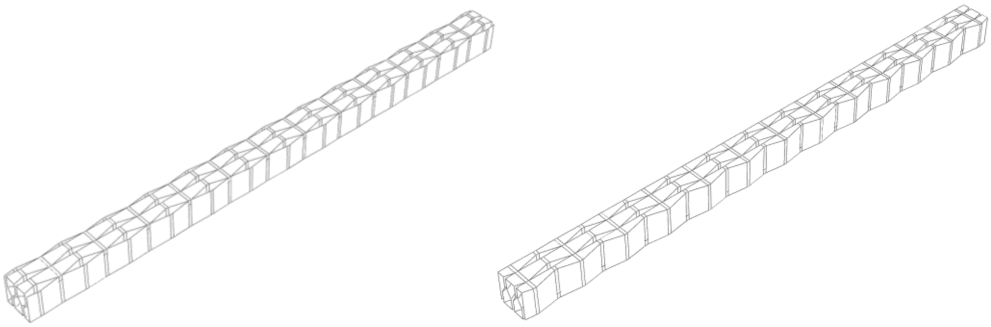

(a) (b)

Figure 5.27. Geometries of two-way bending beam with (a) placement 1 and (b) placement 2.

Table 5.5: Parameters of two-way bending beam.

Parameters	α_{t1}	α_{t2}	a_t	b_t	c_t	d_t	h_t
Values	62.2	82.0	35.7	25	10	15	9.17

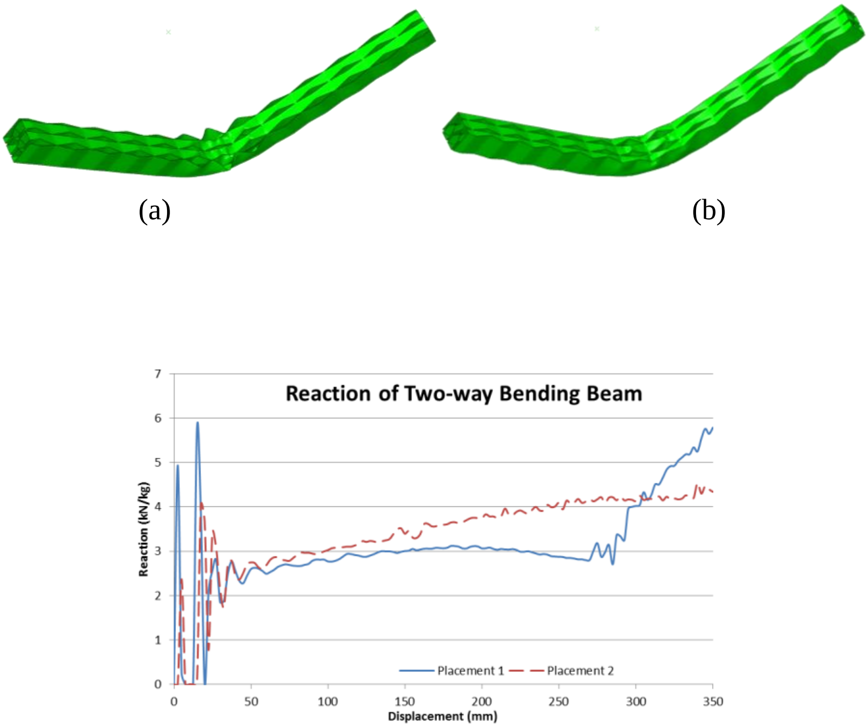

(a) (b)

(c)

Figure 5.28. Numerical simulation: deformation with displacement of 250 mm of (a) placement 1 and (b) placement 2; and (c) their reaction force plots.

5.5 Introduction of Origami Arches and Shells

All the beams and panels presented in previous sections can be transferred into arches and shells by modifying their origami folding patterns. This shall extend the applicability of these designs. A preliminary study of these designs is presented in this section.

5.5.1 Geometry

There can be two directions of curvature, which are named as *curve* 1 and *curve* 2 and are shown in Figure 5.29(a) and (b) respectively. It shows that additional folding lines are added to origami patterns comparing to origami beam (Figure 5.1). There are several ways of creating arches from origami beam, which essentially make sure that one side of the beam is folded with a larger angle than the other side. One simple solution is to make some pattern lines unparalleled to each other, and add diagonal lines for rigid-foldability. Design details and folding mechanism of origami arches and shells are comparable to beams and panels, except for the replacement of α to α_1 and α_2, noted in Figure 5.29. As in Section 5.4.2, face-switcher (Figure 5.23) is also applicable in origami arches and shells.

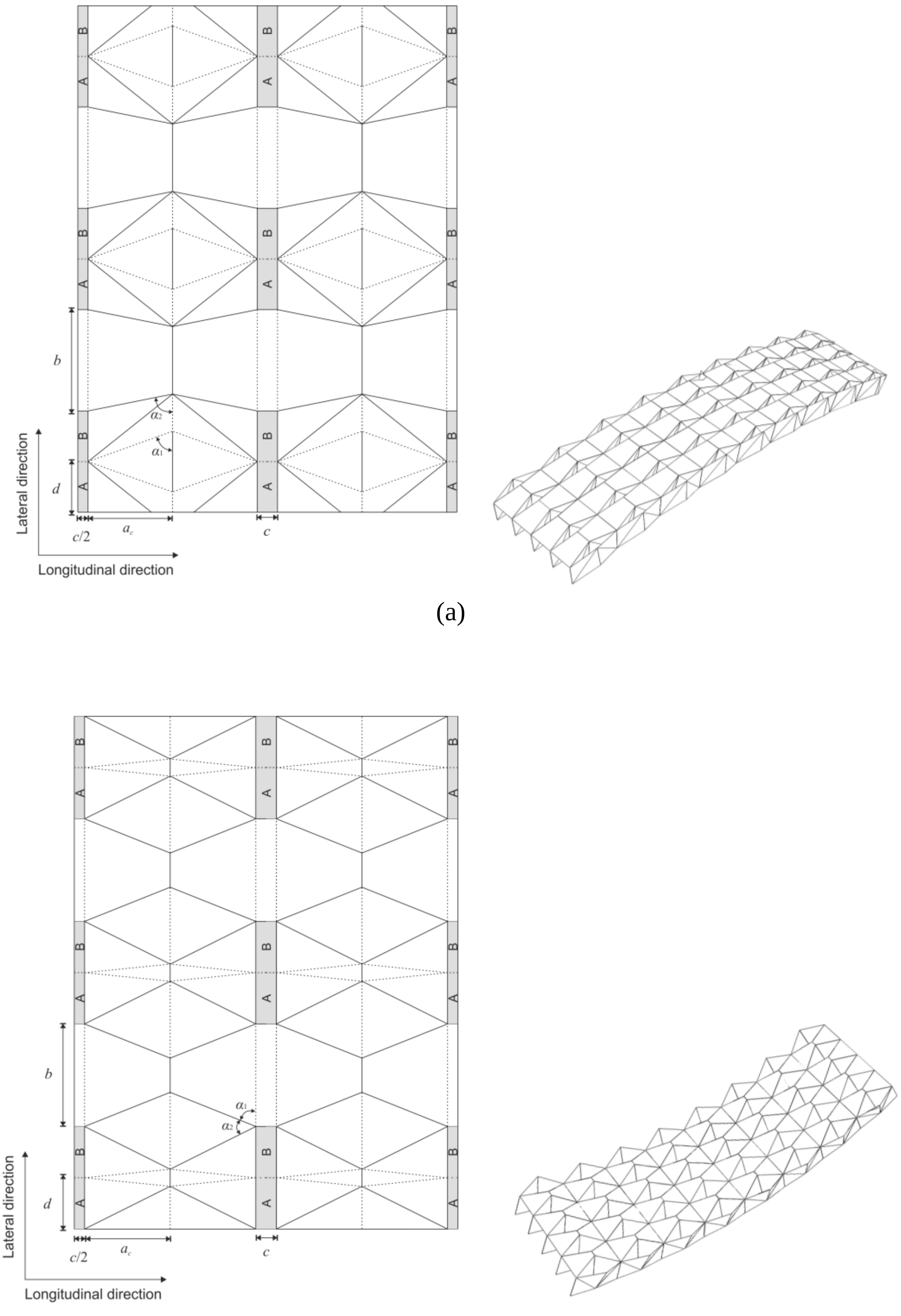

(a)

(b)

Figure 5.29. Folding pattern and folded geometry of (a) curve 1 and (b) curve 2.

5.5.2 Preliminary Numerical Simulation

A conventional arch named as A_0 was made from cross-section shown in Figure 5.4 with a radius of 2832 mm, depth of 55 mm, and span of 983.5 mm, shown in Figure 5.30(a). Based on parameters used by B_{1_3}, a numerical model of origami arch, named as A_1, was made of curve 1 geometry, shown in Figure 5.30(a). Values of α_1 and α_2 were 77.7° and 83.7°, and all other parameters were the same with origami beam B_{1_3}. This gave the origami arch same radius, depth, and span of A_0. Numerical simulations of three-point bending of arches were done to assess their bending resistance in large deformation, and corresponding deformations are shown in Figure 5.30(b). This showed that the material in the middle of origami arch bulged upwards as same as in origami beam (Figure 5.9), while A_0 demonstrated structural depth reduction. Reaction force plots of the conventional arch A_0 and origami arch A_1 are presented in Figure 5.31. It shows that origami arch had more constant reaction force and higher SEA by 14.5%.

Origami shells with m_b = 2 and 4, which were named as A_2 and A_3 respectively, were also numerically simulated, shown in Figure 5.32. They showed same failure mechanism as A_1. SEA of A_1, A_2 and A_3 were 735.0, 869.4, and 999.3 kJ/kg respectively, which indicates that higher SEA can be achieved with more lateral units.

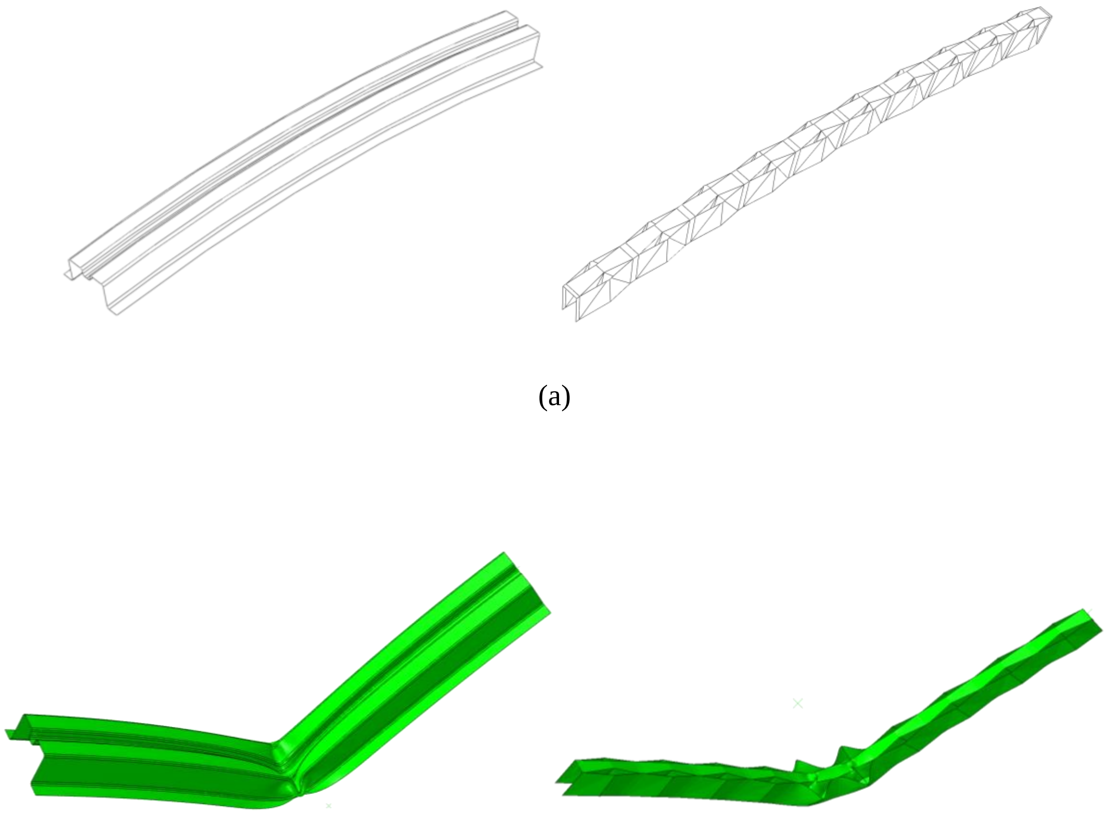

(a)

(b)

Figure 5.30. (a) Geometries and (b) simulated deformation with displacement of 300 mm of conventional arch A_0 and origami arch A_1.

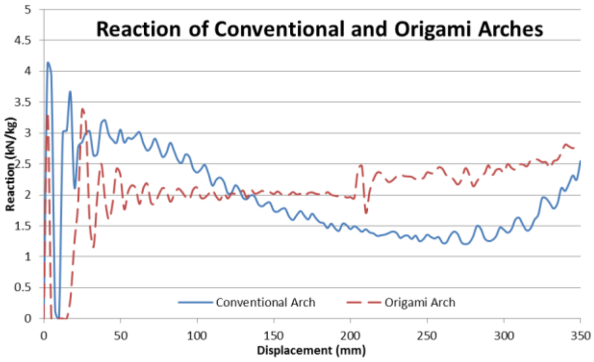

Figure 5.31. Reaction force plots of conventional and origami arches.

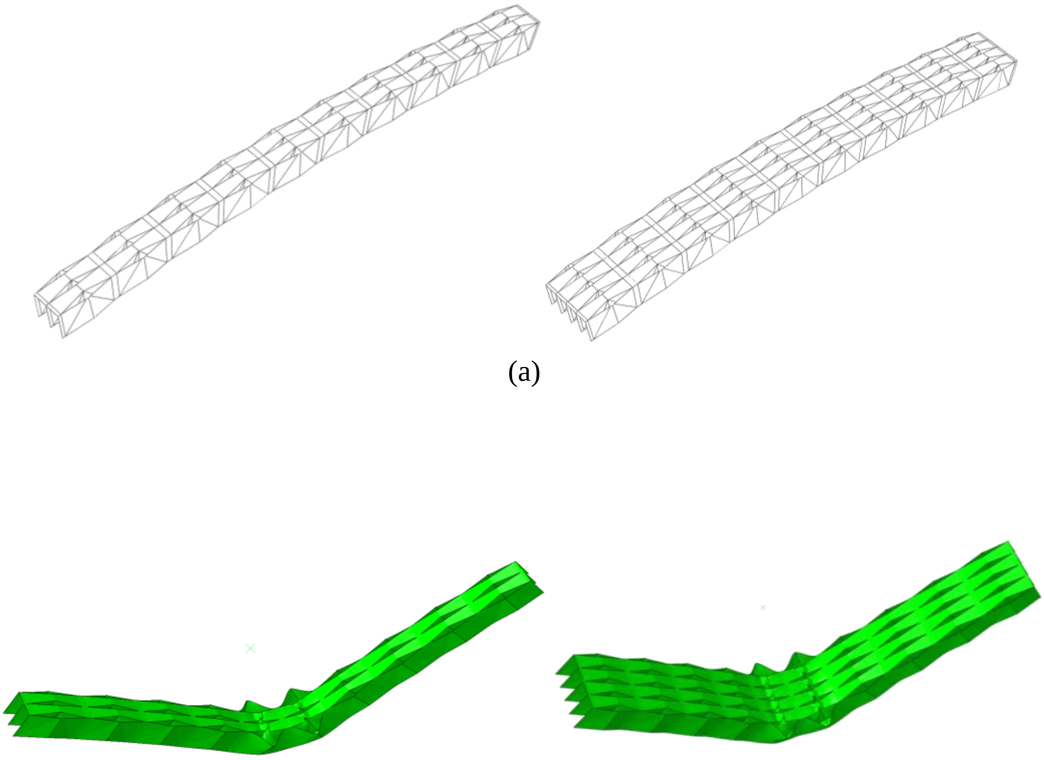

(a)

(b)

Figure 5.32. (a) Geometries and (b) simulated deformation with displacement of 300 mm of origami arches/shells with $m_b = 2$ and 4.

Like presented in Section 5.4.2, face-switchers can be also introduced to origami arches and shells. A paper folded model is presented in Figure 5.33(a), and it shows that webs are facing up at two ends of the arch. A numerical arch model with face-switcher was made, named as A_{2s} and shown in Figure 5.33(b). Values of α_1 and α_2 for curve 1 part were 77.7° and 87.5°, and for curve 2 part were 89° and 80°. Other parameters were kept as same as $B_{1\_3\_2s}$, and arch A_{2s} had a radius of 2820 mm and a span of 989.2 mm. Numerical simulations of A_{2s} was done with the same setting as in Section 5.4.2. Simulated deformation is shown in Figure 5.33(c), which gave the same deformation as Figure 5.24.

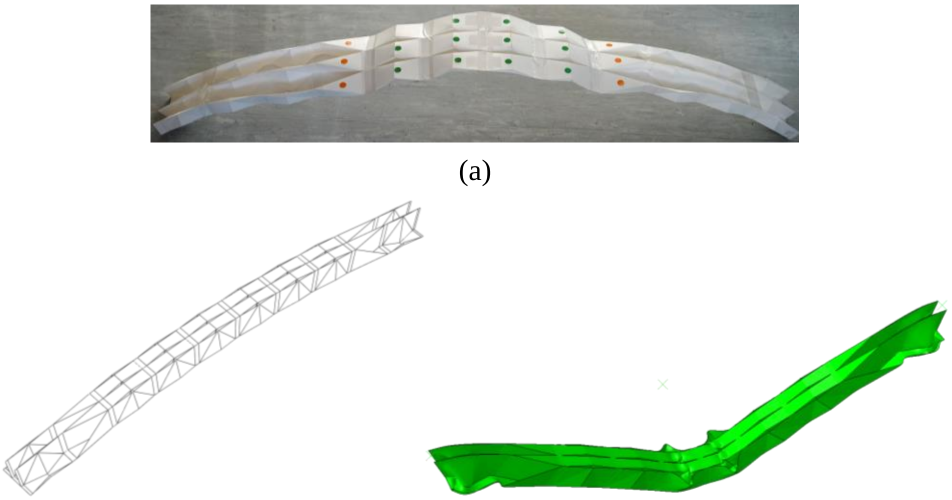

(a)

(b) (c)

Figure 5.33. (a) Paper folded model, (b) numerical geometry, and (c) simulated deformation with displacement of 300 mm of origami arches with face-switcher.

5.6 Summary

One problem of thin-walled beams when bent in large deformation is the reduction of cross-section height, shown in Figure 5.34(a). Correspondingly, the reaction force of beam is reduced significantly as shown in Figure 5.34(b). The geometric intervention given in this thesis is to replace straight beam with zig-zag origami geometry, shown in Figure 5.34(c). This geometry indicates respectively the positions of indentation and bulge during bending. Spot-welding is applied to stiffen the locations of expected indentation, which allows only increase of cross-section height, shown in Figure 5.34(d). The experimental demonstration is shown in Figure 5.34(e).

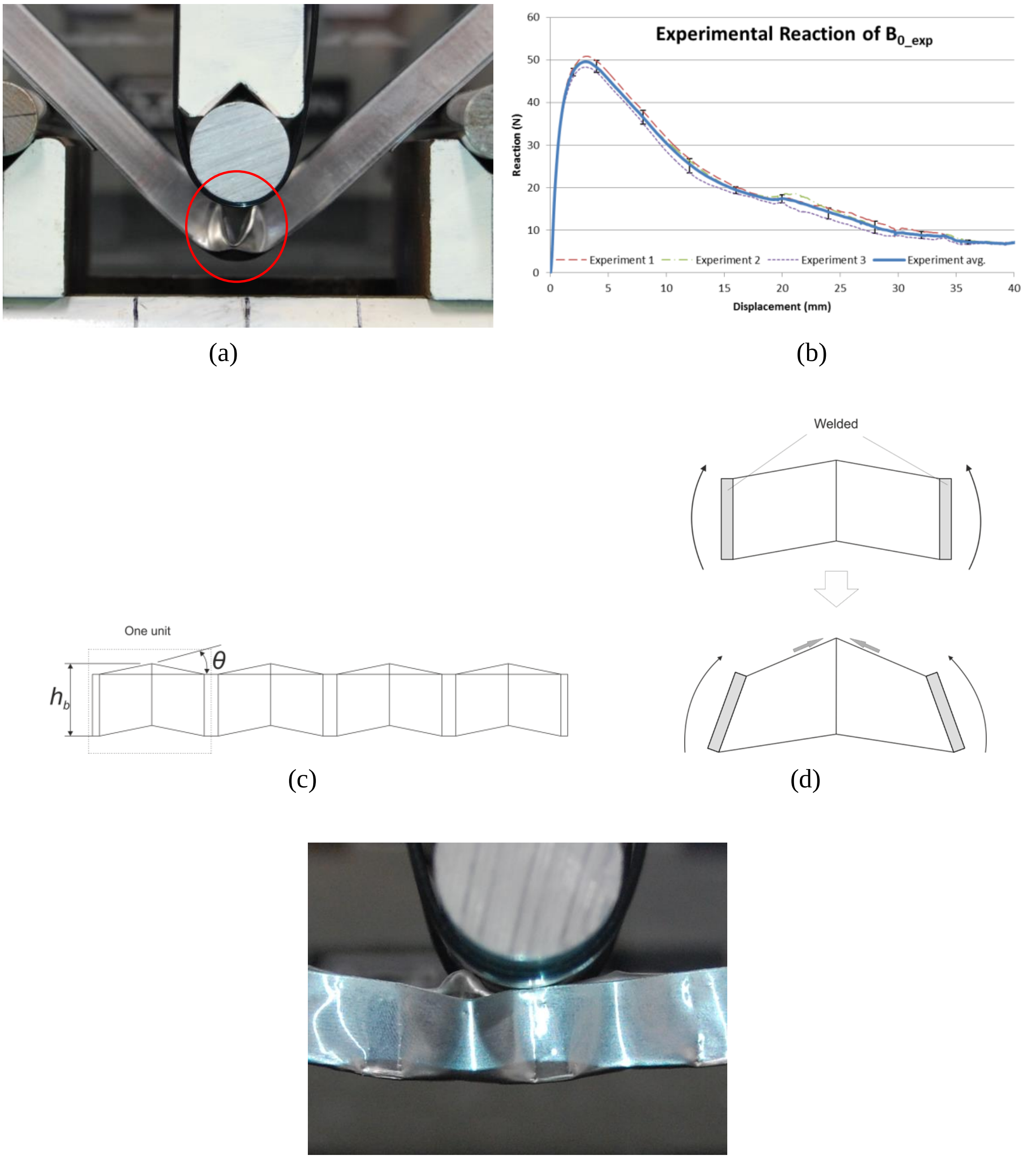

(a) (b)

(c) (d)

(e)

Figure 5.34. Problem of beam bending reflected in (a) experimental deformation and (b) reaction curves, and (c) its corresponding (side view) geometric solution with (d) deformation illustration, and (e) its experimental demonstration.

This chapter presents a series of energy absorbing bending devices according to this design, which aim for high and sustainable bending resistance. The key solution provided in this chapter is by modifying geometry to create a bending device which does not suffer section height reduction in large deformation. Numerical and experimental works have been done to validate the effectiveness of those new designs, and demonstrated their improvement to conventional open-section beam in terms of both specific energy absorption and load uniformity.

The design of basic origami beam is provided at first, and corresponding numerical simulations with different parameters have been done afterward. These show that 12.7%-20.7% lower load uniformity and 23.0%-40.0% higher specific energy absorption (SEA) than those of a typical conventional open-section beam can be achieved with appropriate parameters. Small-scale experiments of origami and conventional beams, and their comparison with numerical results have been done. It confirmed the merits of origami beams and the accuracy of numerical simulation used in this chapter. Further geometric modifications of basic origami beam are presented. Origami panels can be made with a larger number of lateral units, which significantly increases their SEA and stability. Since the top face of origami beam/panel is designed for compression and bottom webs only for tension, developable face-switcher is introduced to enable them to switch their face-sides within the beam/panel to cope with different pre-decided loading scenarios. For uncertain loading situations, two-way bending beam/panel is proposed, which has a similar geometric shape at both top and bottom sides. All these modifications of basic origami beam were simulated, which demonstrated their effectiveness. Origami arches and shells can be made by altering folding patterns of origami beams and panels, and similar performances have been achieved.

Chapter 6 Conclusion

This thesis has been primarily concerned with three types of newly developed energy absorbing structures, including both compression and bending devices. Summary of achievements and future work are presented in this chapter.

6.1 Summary of Achievements

6.1.1 Origami Concave Tubes

Chapter 3 presents designs and performances of a series of origami concave tubes. These tubes have concave cross-sections and origami initiators, which are designed for preserving progressive failure mode which is not possible or stable in tubes with concave cross-sections. This modification is expected to largely increase the number of effective corners comparing to the square tube during progressive buckling. This can introduce failure mechanism with more complex folds of material, and in consequence, dramatically increase energy absorption based on their theoretical models.

Totally 13 tubes were made with the only geometrical difference, which consist of the square tube, normal concave tubes, and origami concave tubes. Compression tests were conducted to those tubes. The result showed that normal concave tubes always failed unstably which made them unsuitable for energy absorbing applications. In contrary, origami concave tubes demonstrated stable progressive failure, and achieved around three times of energy absorption of square tube.

Numerical and theoretical analysis were conducted and showed a good match with experimental results, which validated our numerical and theoretical models. Theoretical models can give a quick estimation of energy absorbing ability of those origami concave tubes to assist future design. Further numerical parametric study of origami concave tubes was carried out and gave practical ranges of parameters to ensure progressive failure, which provided guidelines for the future design of origami concave tubes. It also showed that reaction force of origami concave tubes can approach peak buckling force of corresponding concave tubes, which suggests origami concave tubes can reach the theoretical limit of energy absorption. Different loadings were considered and showed that merits of origami concave tubes are preserved in dynamic and inclined loadings within practical ranges.

6.1.2 Thin Corrugated Tube Inversion

Chapter 4 proposes to use thin corrugated tubes for inversion instead of circular tubes. Tubes with corrugated cross-section have higher specific buckling force and less imperfection sensitivity than circular tubes, and they also require a smaller load to be inverted due to less need of the circumferential stretch. These improvements enable thin corrugated tubes to be inverted stably with practical friction (with a friction coefficient of 0.3 to 0.4) and imperfection, which has not been achieved or claimed before for circular tube inversion.

Numerical simulations of inverting circular and corrugated tubes were conducted, and the results confirmed merits of using thin corrugated tubes for inversion. In general, thinner tubes are easier to be inverted, but more sensitive to imperfection. Thin corrugated tubes with $100 \leq D/t \leq 200$ can be inverted with practical friction (μ=0.32) and imperfection (amplitude of 0.1 mm), while circular tubes buckled instead of being inverted.

A theoretical model of the reaction force of corrugated tubes inversion was proposed, which can give a quick estimation of energy absorbing capacity of the design. Experiments of inverting thin circular and corrugated tubes were conducted. Numerical, theoretical, and experimental analysis agreed with each other, and confirmed the validity of this idea and the models. An extensive numerical parametric study was carried out, and generated a valid range for each parameter. Engineers can design thin corrugated tubes for inversion conveniently based on the theoretical model and the suggested range for parameters.

6.1.3 **Origami Beams and Arches**

Chapter 5 proposes a series design of origami bending devices, which consist of beams, panels, arches, and shells. Section height of thin-walled beams always reduces significantly in large deformation, and this effect dramatically decreases its stiffness. These new designs essentially solve this problem by using origami technique and spot-welding, which triggers a failure mode without structural depth reduction. In consequence, these new designs maintain almost constant stiffness, and achieve higher energy absorption and lower load uniformity than those of typical beam structure in large deformation.

Extensive numerical simulations were conducted on a commercial bumper beam and a series of origami beams with different parameters. The results showed that properly designed origami beams eliminate structural depth reduction, and can achieve 40% higher specific energy absorption and 20% less load uniformity than those of the commercial beam. Ranges of proper parameters were given for guidance of future design. Small scale experiments were carried out on both commercial and origami beams. The experimental results confirmed the merits of the origami beam, and also showed good consistency with numerical results, which validated the numerical models used.

Further extensions of origami beams were presented. Based on the same idea, different modifications can be done, and have produced many bending devices with different geometries and features, such as beams with different features, panels, arches, and shells. Preliminary numerical studies have been done on those structures, and showed their effectiveness, but more researches are needed in the future.

6.1.4 Summary of Design Methodology

Solutions provided in this thesis are all simple modifications using developable geometry (which can be formed from a flat sheet without stretching), but can make a significant difference in mechanical performance. The methodology of geometric intervention is briefly summarized in Table 6.1 and might be applicable to other situations. Generally, the first step is to identify problems in current failure mechanism, as well as the desired and targeted mechanism. Then use geometric interventions to build a bridge between the two. Main geometrical interventions used in this thesis and their corresponding mechanical effects are listed in Table 6.1. Specific solutions and core ideas in this thesis were generated by appropriate usage of these techniques.

Table 6.1:. Corresponding mechanical effects of geometrical interventions.

Geometric interventions	Mechanical effects
Origami folding	Increase tendency to fail as initially folded
Introduction of corrugation	Increase stiffness in one direction while reduce stiffness in the perpendicular direction
Spot-welding	Stiffen certain parts and prevent deformation

6.2 Future Work

This thesis has developed many new designs for energy absorbing applications, and presented preliminary results of their performances. More extensive designs and details can be worked out. There are three types of future work can be done based on that. One type is the extension and generalization of the research in this thesis, which shall generate more conceptual models, designs, and conclusions. Another one is to turn research outcomes into commercial products, and work on specific details in the process. More work can be done in the analysis part, such as ways of reducing the computational cost of a full FEM model, more realistic impact simulations, investigate different contact models, more accurate analytical model, and so on.

6.2.1 **Origami Concave Tubes**

In research of origami concave tubes, future work is required in mainly four areas. First, theoretical models for the effective stroke concerning the effect of w/t can be developed. This shall lead to a more accurate analytical modelling of energy absorption of origami concave tubes. Theoretical models of evaluating peak buckling force of concave tubes can be developed. It was attempted but not included in this thesis, and found the possibility of modelling it in simple ways. This research is greatly meaningful for the design of origami concave tubes. Second, more experiments can be done to confirm numerical results in the parametric study. Third, further research can be carried out for modified geometries, such as working out features of various tapered tubes and tubes with different concave cross sections or different origami initiators (given in Appendix). This direction is introduced further below.

There are other forms of origami concave tubes based on the same concepts. One type of modifications is to change the cylindrical shape of the tube into a tapered shape. Another type of modification is to change the cross section into other kinds of concave shapes. Several examples are given below to illustrate that both directions of modification are effective.

Tapered origami concave tubes

Due to the reduced stroke of O2 origami concave tube, one tapered version can be developed to solve this problem, shown in Figure 6.1. The geometry of it was modified from O2 origami concave tube with parameters of Table 3.1. Simulation of the tapered tube was done, and its deformation is shown in Figure 6.2. It shows that the material was not only accommodated vertically, but also horizontally, which led to larger stroke from 72.4% (cylindrical shape) to 79.3% (tapered shape). Different forms of tapered shape and corresponding folding patterns are given in Appendix.

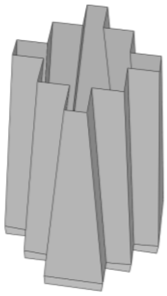

Figure 6.1. Geometry of one type of tapered O2 origami concave tube.

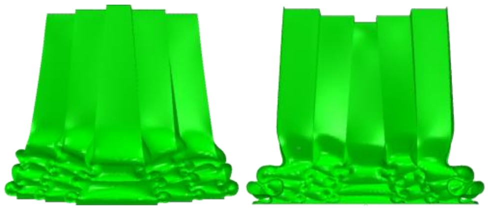

Deformation when displacement is 60 mm and its sectional view.

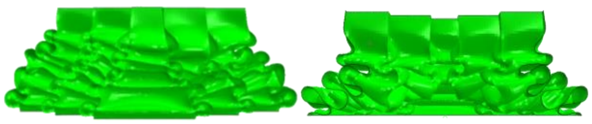

Deformation when displacement is 108 mm and its sectional view.
Figure 6.2. Deformation tapered O2 origami concave tube.

Other concave cross-sections

Further development based on previous cross-sections can be done, such as extending the shape in Figure 2.4(c) into O3 origami concave tube. Other than focusing on the same base, concave cross-sections from different bases can also be used to develop origami concave tubes with the same idea. This conclusion was demonstrated with two cross-sections from two different bases, which are shown in Figure 6.3. Two corresponding origami concave tubes were made with equivalent parameters of O2 origami concave tubes listed in Table 3.1. Simulated crushing deformations are shown in Figure 6.4, which indicates they also achieved progressive buckling modes. Geometry shown in Figure 6.3(a) and Figure 6.4(a) can be used as an alternative for the traditional circular tube. This demonstrates that the same idea is also applicable to concave cross-sections from different bases. More examples of concave shapes are given in Appendix.

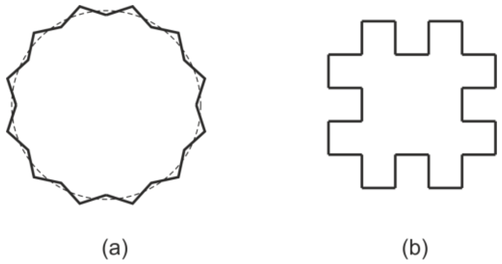

Figure 6.3. Two different concave shapes as tube cross sections.

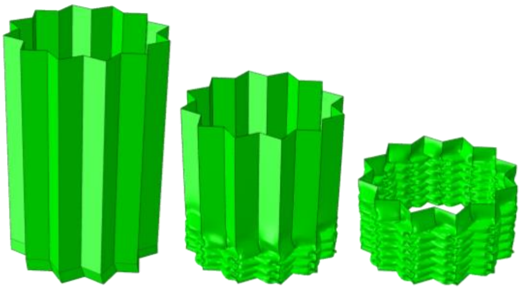

(a)

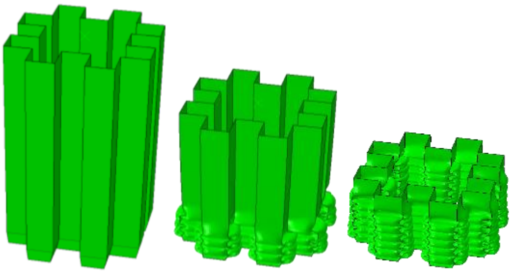

(b)

Figure 6.4. Deformation of two origami concave tubes with different concave cross-sectional shapes.

Different cross-sections and configurations might have different features. Comparison of those results can be done to find out more generally optimized designs in different situations, such as in inclined loading.

Finally, practical research can be carried out in turning these designs into real products, which shall need an extensive corporation with industry.

6.2.2 **Inversion of Thin Corrugated Tubes**

In the inversion of thin corrugated tubes, further investigation for thinner tubes (with $D_{in}/t > 200$) can be carried out if needed. More works can be done in theoretical modelling of inverting force of corrugated tube. Especially the coupling effect between losing corrugation and inversion process, as well as friction contribution shall be looked into. A theoretical model of buckling force of corrugated tube can also be established, which shall largely simplify the design process. Tube inversion mechanism is a good energy absorbing strategy, and further design of corresponding energy absorbing devices and commercialization can be looked into. Other applications of this mechanism, such as certain shape forming, can also be looked into.

6.2.3 Energy Absorption of Origami Beams and Arches

In research of origami bending devices, a number of designs and possibilities based on the same idea are presented, which have opened many more avenues for research. Varieties of bending devices are proposed, but only the basic design of origami beam has been carefully examined. More work can be done to analyse those other bending devices both numerically and experimentally. More geometric modifications can be explored, such as two-way bending arches and shells. Theoretical models can be developed to estimate their energy absorption, which can be quite difficult due to some five-crease vertexes in the kinematical model. Other applications of these bending devices can be investigated, such as energy absorbing improvement of slim struts. For the development into actual products of these designs, further investigations are required as a follow-up to this initial study of origami bending devices. Foremost, fields of specific industrial application for these designs shall be identified. Manufacturing, full-scale experiments, and detailed design shall be carried out afterward.

References

ABRAMOWICZ, W. 1983. The effective crushing distance in axially compressed thin-walled metal columns. 1**,** 309-317.

ABRAMOWICZ, W. & JONES, N. 1984. Dynamic axial crushing of square tubes. *International Journal of Impact Engineering,* 2**,** 179-208.

ABRAMOWICZ, W. & JONES, N. 1986. Dynamic progressive buckling of circular and square tubes. *International Journal of Impact Engineering,* 4**,** 243-270.

ABRAMOWICZ, W. & WIERZBICKI, T. 1989. Axial crushing of multicorner sheet metal columns. *Journal of Applied Mechanics, Transactions ASME,* 56**,** 113-120.

ADACHI, T., TOMIYAMA, A., ARAKI, W. & YAMAJI, A. 2008. Energy absorption of a thin-walled cylinder with ribs subjected to axial impact. *International Journal of Impact Engineering,* 35**,** 65-79.

AIROLDI, A. & JANSZEN, G. 2005. A design solution for a crashworthy landing gear with a new triggering mechanism for the plastic collapse of metallic tubes. *Aerospace Science and Technology,* 9**,** 445-455.

AL-HASSANI, S. T. S., JOHNSON, W. AND LOWE, W. T. 1972. Characteristics of inversion tubes under axial loading. Journal of Mechanical Engineering Science.

ALLAN, T. 1968. Experiment and Analytical Investigation of the Behavior of Cylindrical Tubes Subject to Axial Compressive Forces. *Journal of Mechanical Sciences* 10(2)**,** 182-197.

BARDI, F. C. & KYRIAKIDES, S. 2006. Plastic buckling of circular tubes under axial compression—part I: Experiments. 48**,** 830-841.

BELCASTRO, S.-M. & HULL, T. C. 2002. Modelling the folding of paper into three dimensions using affine transformations. 348**,** 273-282.

BRUSH, D. O. & ALMROTH, B. O. 1975. *Buckling of bars, plates, and shells,* McGraw-Hill.

Calladine, C. R., 1989, Theory of Shell Structures, Cambridge University Press.

Callister, W. D., 2005, Fundamentals of Materials Science and Engineering: An Integrated Approach, John Wiley & Sons.

CARPENTER, R. A. 1990. Vehicle Bumper System. US Patent, 4,961,603.

CHEN, D. H. & OZAKI, S. 2009. Numerical study of axially crushed cylindrical tubes with corrugated surface. *Thin-Walled Structures,* 47**,** 1387-1396.

CHEN, W. & WIERZBICKI, T. 2001. Relative merits of single-cell, multi-cell and foam-filled thin-walled structures in energy absorption. *Thin-Walled Structures,* 39**,** 287-306.

CHEN, Y., PENG, R. & YOU, Z. 2015. Origami of thick panels. *Science,* 349**,** 396-400.

EL-DOMIATY, A. 1997. Curling of thin tubes: Analytical and experimental study. *Journal of Materials Engineering and Performance,* 6**,** 481-495.

EVGUENI T. FILIPOV, T. T., AND GLAUCIO H. PAULINO 2015. Origami tubes assembled into stiff, yet reconfigurable structures and metamaterials. *PNAS*.

FALLER, R. K., SICKING, D. L., BIELENBERG, R. W., ROHDE, J. R., POLIVKA, K. A. & REID, J. D. 2007. Performance of steel-post, W-beam guardrail systems. Transportation Research Record.

FAN, Z., LU, G. & LIU, K. 2013. Quasi-static axial compression of thin-walled tubes with different cross-sectional shapes. *Engineering Structures,* 55**,** 80-89.

FELTON, S., TOLLEY, M., DEMAINE, E., RUS, D. & WOOD, R. 2014. A method for building self-folding machines. *Science,* 345**,** 644-646.

FILIPOV, E. T., PAULINO, G. H. & TACHI, T. 2016. Origami tubes with reconfigurable polygonal cross-sections. *Proceedings of the Royal Society of London A: Mathematical, Physical and Engineering Sciences,* 472.

GATTAS, J. 2013. *Quasi-static Impact of Foldcore Sandwich Panels.* Doctor of Philosophy, University of Oxford.

GATTAS, J. M., WU, W. & YOU, Z. 2013. Miura-Base Rigid Origami: Parameterizations of First-Level Derivative and Piecewise Geometries. 135**,** 111011-111011.

GATTAS, J. M. & YOU, Z. 2014. Quasi-static impact of indented foldcores. 73**,** 15-29.

GATTAS, J. M. & YOU, Z. 2015. The behaviour of curved-crease foldcores under low-velocity impact loads. 53**,** 80-91.

GUILLOW, S. R., LU, G. & GRZEBIETA, R. H. 2001. Quasi-static axial compression of thin-walled circular aluminium tubes. *International Journal of Mechanical Sciences,* 43**,** 2103-2123.

HOSSEINIPOUR, S. J. & DANESHI, G. H. 2003. Energy absorbtion and mean crushing load of thin-walled grooved tubes under axial compression. *Thin-Walled Structures,* 41**,** 31-46.

ISHIDA, S., UCHIDA, H. & HAGIWARA, I. 2014. Vibration isolators using nonlinear spring characteristics of origami-based foldable structures. 80**,** DR0384-DR0384.

JIN, L. & KEPING, L. 2013. Improved design on guardrail used for frequent accident occurring highway section.

JOHNSON, W. & WALTON, A. C. 1983a. Protection of car occupants in frontal impacts with heavy lorries: Frontal structures. *International Journal of Impact Engineering,* 1**,** 111-123.

JOHNSON, W. & WALTON, A. C. 1983b. An experimental investigation of the energy dissipation of a number of car bumpers under quasi-static lateral loads. *International Journal of Impact Engineering,* 1**,** 301-308.

JONES, R. M. 2006. *Buckling of Bars, Plates, and Shells*, Bull Ridge Publishing.

JONSSON, M. & JUNTTI, M. 2005. Bumper beam for a vehicle and a method of adapting a bumper beam to various vehicle models. *US Patent, 6,863,321*.

KANAE, Y., SASAKI, T. & SHIMAMURA, S. 1986. Experimental and Analytical Studies on the Drop-Impact Test with Lead-Shielded Scale Model Radioactive Material Shipping Casks. *Kikai Gijutsu Kenkyusho Shoho/Journal of Mechanical Engineering Laboratory,* 40**,** 201-213.

KURIBAYASHI, K., TSUCHIYA, K., YOU, Z., TOMUS, D., UMEMOTO, M., ITO, T. & SASAKI, M. 2006a. Self-deployable origami stent grafts as a biomedical application of Ni-rich TiNi shape memory alloy foil. 419**,** 131-137.

KURIBAYASHI, K., TSUCHIYA, K., YOU, Z., TOMUS, D., UMEMOTO, M., ITO, T. & SASAKI, M. 2006b. Self-deployable origami stent grafts as a biomedical application of Ni-rich TiNi shape memory alloy foil. *Materials Science and Engineering: A,* 419**,** 131-137.

LANG, R. J. 2001. *Eyeglass Telescope* [Online]. [Accessed].

LEE, T.-U. & GATTAS, J. M. 2016. Geometric Design and Construction of Structurally Stabilized Accordion Shelters. 8**,** 031009-031009.

Z. B. Lei, Z. Chen, M. X. Lei, R. Al, "Research on Safety Technology for Initiative Anti-Collision of Bridge", Applied Mechanics and Materials, Vols. 204-208, pp. 2196-2199, 2012

LI, Y., YOU, Z. 17-20 August, 2014. Thin-walled Open-section Origami Beams for Energy Absorption. *Proceedings of the ASME 2014 International Design Engineering Technical Conferences and Computers and Information in Engineering Conference.* Buffalo, New York.

LIU, S., TONG, Z., TANG, Z., LIU, Y. & ZHANG, Z. 2015. Bionic design modification of non-convex multi-corner thin-walled columns for improving energy absorption through adding bulkheads. 88**,** 70-81.

LU, G. 1993. A study of the crushing of tubes by two indenters. *International Journal of Mechanical Sciences,* 35**,** 267-278.

LU, G. & YU, T. X. 2003. *Energy Absorption of Structures and Materials,* Elsevier Science.

LV, C., KRISHNARAJU, D., KONJEVOD, G., YU, H. & JIANG, H. 2014. Origami based Mechanical Metamaterials. 4**,** 5979.

MA, J. 2011. Thin-Walled Tubes with Pre-folded Origami Patterns as Energy Absorption Devices. *Thesis, Oxford University*.

MA, J. & YOU, Z. 2013a. Energy absorption of thin-walled beams with a pre-folded origami pattern. 73**,** 198-206.

MA, J. & YOU, Z. 2013b. Energy Absorption of Thin-Walled Square Tubes With a Prefolded Origami Pattern—Part I: Geometry and Numerical Simulation. *Journal of Applied Mechanics,* 81**,** 011003-011003.

MAMALIS, A. G., MANOLAKOS, D. E., DEMOSTHENOUS, G. A. & IOANNIDIS, M. B. 1996. Energy absorption capability of fibreglass composite square frusta subjected to static and dynamic axial collapse. *Thin-Walled Structures,* 25**,** 269-295.

MANUAL, A. A. U. S. 2013. Abaqus Documentation Version 6.13. *Dassault Systems SIMULIA corp., Providence, RI, USA*.

MISCOW F, P. C. & AL-QURESHI, H. A. 1997. Mechanics of static and dynamic inversion processes. *International Journal of Mechanical Sciences,* 39**,** 147-161.

NING, X. & PELLEGRINO, S. 2013. Imperfection-Insensitive Axially Loaded Cylindrical Shells. *54rd AIAA/ASME/ASCE/AHS/ASC Structures, Structural Dynamics and Materials Conference*.

NOJIMA, T. 2002. Modelling of folding patterns in flat membranes and cylinders by Origami. *JSME International Journal, Series C: Mechanical Systems, Machine Elements and Manufacturing,* 45**,** 364-370.

P. K. GUPTA, N. K. G. 2013. Investigation of External Inversion of Thin-Walled Tubes. Proc. Indian Natn. Sci. Acad. 79 No. 4.

PODJADTKE, R., WITTHAUS, H. & BREEDLOVE, J. 2008. Development in Steel Roadway Support. *27th International Conference on Ground Control in Mining*.

REDDY, S., ABBASI, M. & FARD, M. 2015. Multi-cornered thin-walled sheet metal members for enhanced crashworthiness and occupant protection. 94**,** 56-66.

REDDY, T. Y. & REID, S. R. 1980. Phenomena associated with the crushing of metal tubes between rigid plates. *International Journal of Solids and Structures,* 16**,** 545-562.

REDDY, T. Y. & REID, S. R. 1986. Axial splitting of circular metal tubes. *International Journal of Mechanical Sciences,* 28**,** 111-131.

REID, J. D. & SICKING, D. L. 1998. Design and simulation of a sequential kinking guardrail terminal. *International Journal of Impact Engineering,* 21**,** 761-772.

REID, S. R. 1993. Plastic deformation mechanisms in axially compressed metal tubes used as impact energy absorbers. *International Journal of Mechanical Sciences,* 35**,** 1035-1052.

REID, S. R. & REDDY, T. Y. 1986. Static and dynamic crushing of tapered sheet metal tubes of rectangular cross-section. *International Journal of Mechanical Sciences,* 28**,** 623-637.

REID, S. R., REDDY, T. Y. & GRAY, M. D. 1986. Static and Dynamic Axial Crushing of Foam-Filled Sheet Metal Tubes. *International Journal of Mechanical Sciences,* 28**,** 295-322.

ROSA, P. A., BAPTISTA, R. M. O., RODRIGUES, J. M. C. & MARTINS, P. A. F. 2004. An investigation on the external inversion of thin-walled tubes using a die. *International Journal of Plasticity,* 20**,** 1931-1946.

SCHENK, M. 2011. *Folded Shell Structures.* Doctor of Philosophy, University of Cambridge.

SCHENK, M., GUEST, S. D. & MCSHANE, G. J. 2014a. Novel stacked folded cores for blast-resistant sandwich beams. 51**,** 4196-4214.

SCHENK, M., VIQUERAT, A. D., SEFFEN, K. A. & GUEST, S. D. 2014b. Review of Inflatable Booms for Deployable Space Structures: Packing and Rigidization. *Journal of Spacecraft and Rockets,* 51**,** 762-778.

SCHWARTZ, R. & RAMOO, R. 1999. Energy absorbing bumper. *US Patent, 6,007,123*.

SEKHON, G. S., GUPTA, N. K. & GUPTA, P. K. 2003. An analysis of external inversion of round tubes. *Journal of Materials Processing Technology,* 133**,** 243-256.

SILVERBERG, J. L., EVANS, A. A., MCLEOD, L., HAYWARD, R. C., HULL, T., SANTANGELO, C. D. & COHEN, I. 2014. Using origami design principles to fold reprogrammable mechanical metamaterials. *Science,* 345**,** 647-650.

SILVERBERG, J. L., NA, J.-H., EVANS, A. A., LIU, B., HULL, T. C., SANTANGELO, CHRISTIAN D., LANG, R. J., HAYWARD, R. C. & COHEN, I. 2015. Origami structures with a critical transition to bistability arising from hidden degrees of freedom. 14**,** 389-393.

SINGACE, A. A., ELSOBKY, H. & REDDY, T. Y. 1995. On the eccentricity factor in the progressive crushing of tubes. 32**,** 3589-3602.

TANG, Z., LIU, S. & ZHANG, Z. 2012. Energy absorption properties of non-convex multi-corner thin-walled columns. 51**,** 112-120.

TIMOSHENKO, S. 1961. *Theory of elastic stability*, McGraw-Hill.

WEI, J., JIN, X. N., DONG, R. Z. & YANG, M. J. 2013. Influence of structure parameters on W-beam guardrail crashworthiness. *Wuhan Ligong Daxue Xuebao/Journal of Wuhan University of Technology,* 35**,** 90-95.

WHO 2015. World report on road traffic injury prevention.

WIERZBICKI, T. & ABRAMOWICZ, W. 1983. On the Crushing Mechanics of Thin-Walled Structures. *Journal of Applied Mechanics,* 50**,** 727-734.

WIERZBICKI, T. & JONES, N. 1989. *Structural failure*, Wiley.

WU, E. & JIANG, W.-S. 1997. Axial crush of metallic honeycombs. *International Journal of Impact Engineering,* 19**,** 439-456.

WU, W. 2010. Rigid Origami: Modelling: Application in Pre-folded Cylinders and Manufatureing. *Thesis, Oxford University*.

WU, W. & YOU, Z. 2010. Modelling rigid origami with quaternions and dual quaternions. *Proceedings of the Royal Society of London A: Mathematical, Physical and Engineering Sciences*.

XIE, S. & ZHOU, H. 2014. Impact characteristics of a composite energy absorbing bearing structure for railway vehicles. *Composites Part B: Engineering,* 67**,** 455-463.

YASUDA, H. & YANG, J. 2015. Reentrant Origami-Based Metamaterials with Negative Poisson's Ratio and Bistability. *Physical Review Letters,* 114**,** 185502.

ZHANG, X., CHENG, G., YOU, Z. & ZHANG, H. 2007. Energy absorption of axially compressed thin-walled square tubes with patterns. *Thin-Walled Structures,* 45**,** 737-746.

ZHANG, X. & HUH, H. 2009. Energy absorption of longitudinally grooved square tubes under axial compression. *Thin-Walled Structures,* 47**,** 1469-1477.

ZHANG, X. W., SU, H. & YU, T. X. 2009. Energy absorption of an axially crushed square tube with a buckling initiator. *International Journal of Impact Engineering,* 36**,** 402-417.

Appendix

Tapered Origami Concave Tubes

Two forms of tapered origami tubes are given in Figure. a1. Corresponding folding patterns are given in Figure a2.

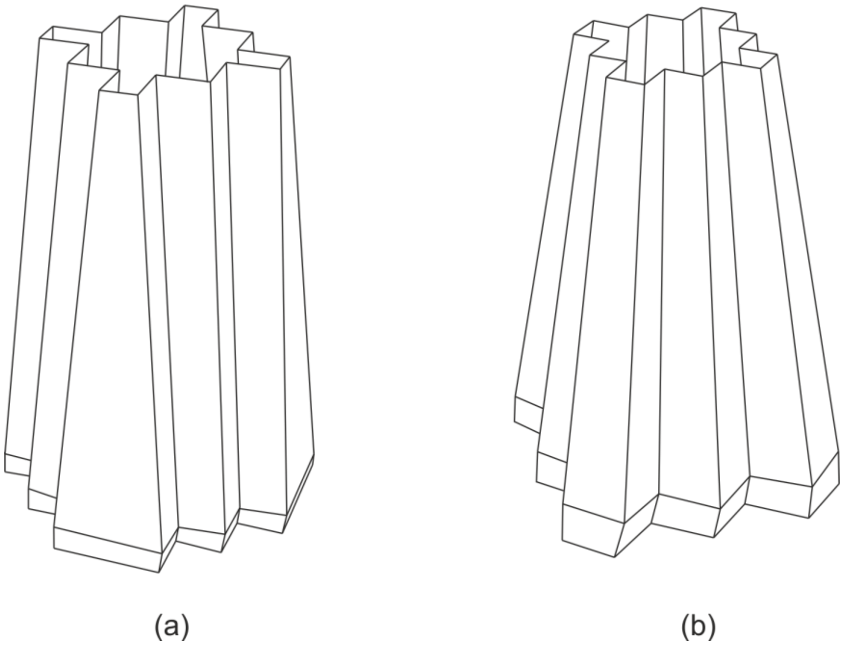

Figure. a1. Forms of tapered origami tubes.

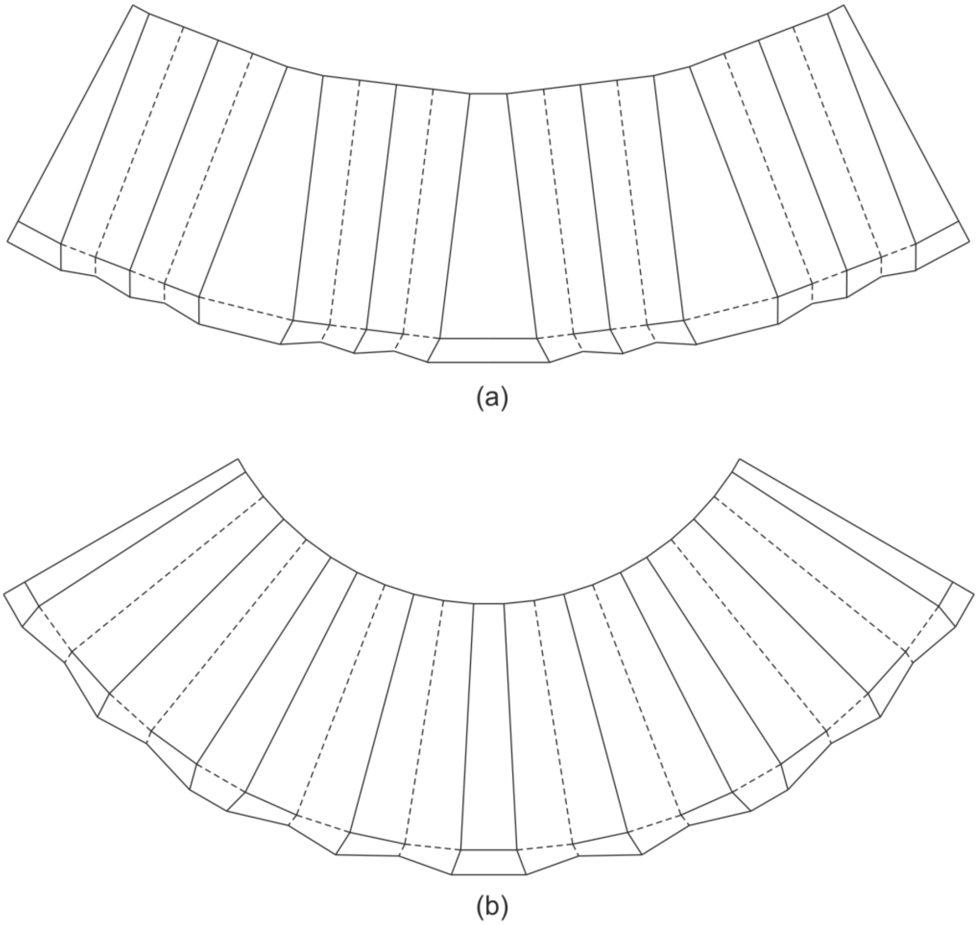

(a)

(b)

Figure. a2. Folding patterns of tapered origami concave tubes.

Different Concave Shapes

Different concave shapes can be used for the cross-sections of origami concave tubes. Some candidates are listed in Figure. a3.

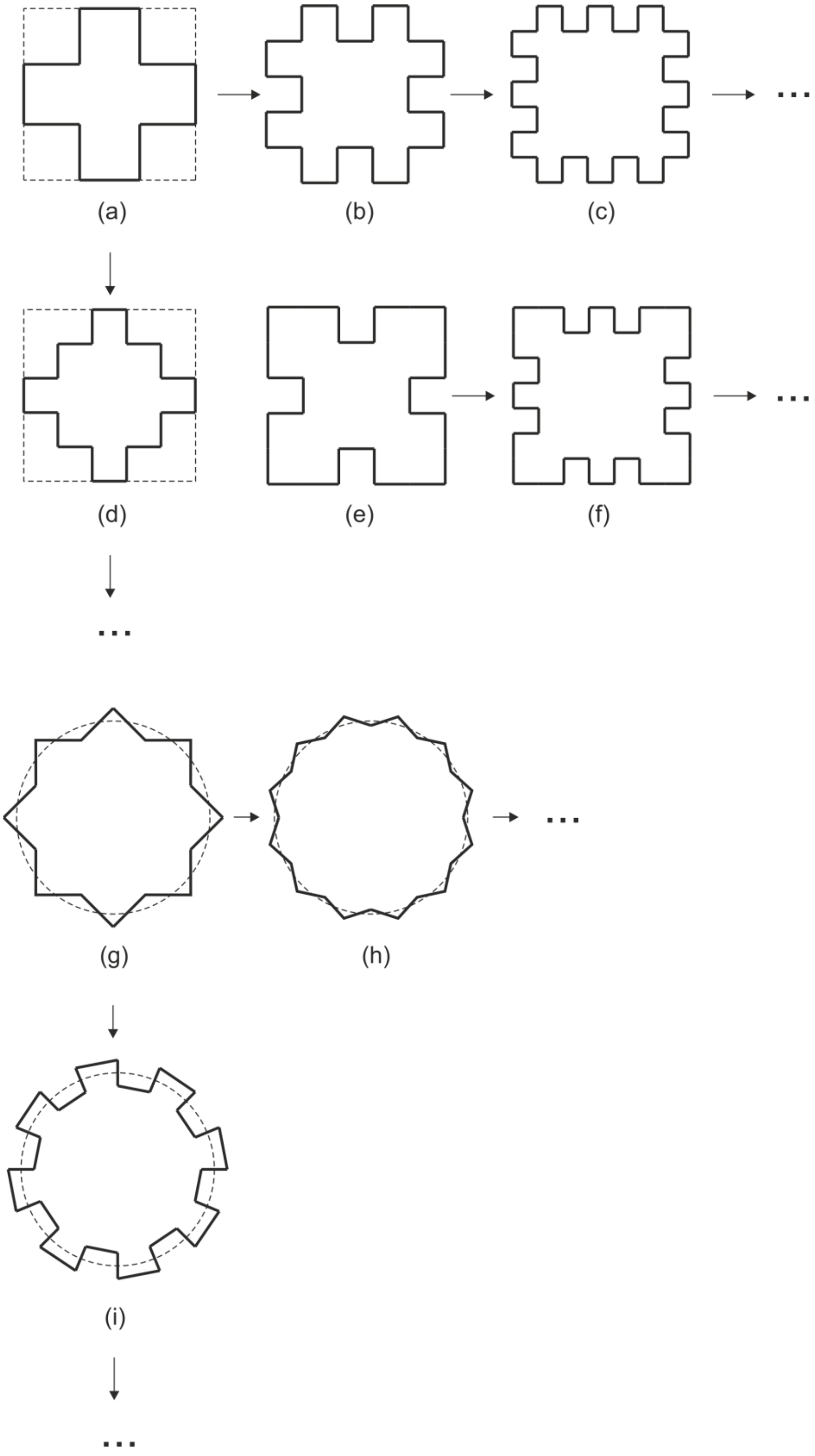

Figure. a3. Concave shapes.

Different Designs of Origami Initiator

Folding patterns of three different origami initiators are presented in Figure. a4. Other ways of creating initiator can be explored, such adding dents or holes at one end.

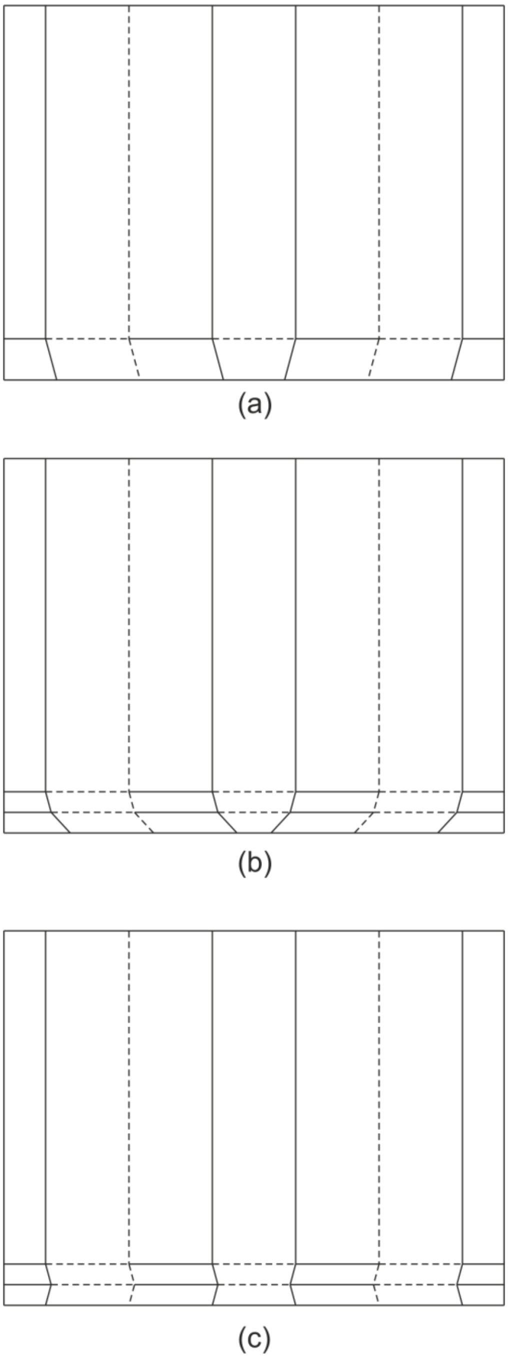

Figure. a4. Folding patterns of different origami initiators.